

Copyright
by
Mingji Wang
2004

The Dissertation Committee for Mingji Wang Certifies that this is the approved version of the following dissertation:

**NANOINDENTATION OF THIN ORGANIC FILMS AND
SELF-ASSEMBLED MONOLAYERS**

Committee:

Kenneth M. Liechti, Supervisor

K. Ravi-Chandar

Gregory J. Rodin

Rui Huang

Peter J. Rossky

Charles B. Mullins

**NANOINDENTATION OF THIN ORGANIC FILMS AND
SELF-ASSEMBLED MONOLAYERS**

by

Mingji Wang, B.S; M.S.

Dissertation

Presented to the Faculty of the Graduate School of

The University of Texas at Austin

in Partial Fulfillment

of the Requirements

for the Degree of

Doctor of Philosophy

The University of Texas at Austin

December 2004

Dedication

To my parents, Xihua Wang and Yunhua Shi.

To my wife, Guirong Gu.

To my son, Matthew (Jianyu) Wang, for bringing light and happiness to my life.

Acknowledgements

The author would like to express his sincere gratitude to his advisor, Professor Kenneth M. Liechti, for his guidance and support through the study and research. The author benefited from his knowledge and experience. His encouragement and humor made my life at UT Austin a lot of fun.

The author is indebted to several research groups due to the interdisciplinary and multi-institutional nature of this research. Special thanks go to Professor John M. White, Professor Peter J. Rossky and their fellow researchers at UT Austin. It was a great experience and honor for the author to work with these two experienced professors. Without their collaboration, the author could not have finished this work. The author is also grateful to Dr. Jack E. Houston at Sandia National Laboratory for his generous assistance in setting up and operating the IFM facility at UT Austin. Dr. Houston continues to supply us with sensors for the IFM, free of charge. The author acknowledges helpful discussions with Professor Robb M. Winter at South Dakota School of Mines and Technology, who also taught the author to operate the IFM at UT Austin.

The author wishes to acknowledge the assistance from so many sources that he received during the research and would like to express thanks to: Dr. Hyacinth L. Cabibil for introducing the author to the IFM; Dr. Hugo Celio for providing further training and many helpful discussions; Dr. Matthew T. Stone and Dr. Vibha Srinivasan for setting up the molecular dynamics simulation

model; Qi Wang for conducting XPS analysis; Daniel Wolfe from Professor George M. Whitesides' group at Harvard University for providing the master grid and Dow Corning Corp. for the free PDMS silicone samples.

The author wishes to thank the professors, the staff and his fellow graduate students in the Department of Aerospace Engineering and Engineering Mechanics at UT Austin. The author treasures the knowledge he gained from them, the help he received from them and their friendship.

Finally, the author wishes to acknowledge the financial support of National Science Foundation (Grant number CMS9978678), Center for Materials Chemistry of The University of Texas at Austin, and the support of the R. A. Welch Foundation and the Department of Aerospace Engineering and Engineering Mechanics of The University of Texas at Austin.

Mingji Wang

The University of Texas at Austin

July 2004

NANOINDENTATION OF THIN ORGANIC FILMS AND SELF-ASSEMBLED MONOLAYERS

Publication No. _____

Mingji Wang, Ph. D.

The University of Texas at Austin, 2004

Supervisor: Kenneth M. Liechti

It has been established for some time now that interfaces between polymers and stiff substrates contain an interphase region (10 nm thick) where the properties of the polymer differ from those of the bulk. It has also been observed that interfacial cracks actually grow in these interphase regions. Thus it is important to understand the mechanical behavior of materials in such thin materials.

Self-assembled monolayers (SAMs) provide well-controlled models for such studies. They are also important materials in MEMS devices where they are used for reducing friction and stiction. The SAM considered in this study was octadecyltrichlorosilane (OTS), which has a chain length of 2.6 nm.

The OTS was probed with an interfacial force microscope (IFM). This relatively new device provides unambiguous force-displacement profiles in

tension (adhesion) and compression (indentation). The IFM was also used to probe thicker films of (3-aminopropyl)triethoxysilane (γ -APS) so that a range of thickness could be considered.

Thin γ -APS films and self-assembled OTS monolayers were deposited on Si(100) surfaces and characterized. A new approach for making OTS monolayers with nano-scale uniformity was developed. Some guidelines for the analysis of IFM experiments were drawn from a parametric study of layer and substrate interactions. Its high resolution in both force and displacement allows the IFM to be used to determine both the elastic mechanical and adhesive properties of thin films. Due to the different molecular structure of thin γ -APS films and self-assembled OTS monolayers, different analytical approaches were required. Combined experimental and continuum analyses of IFM nanoindentation of thin films, which accounted for the layer/substrate and adhesive interactions, were developed. A continuum analysis was used for γ -APS films, while a hybrid continuum-molecular analysis was required for OTS monolayers.

Table of Contents

| | |
|------------------------------------------------------------|------|
| List of Tables..... | xii |
| List of Figures | xiii |
| CHAPTER ONE. INTRODUCTION | 1 |
| 1.1 Overview | 1 |
| 1.1.1 <i>Interfacial fracture and interphase</i> | 1 |
| 1.1.2 <i>Self-assembled monolayers</i> | 3 |
| 1.1.3 <i>Nanoindentation and contact mechanics</i> | 5 |
| 1.1.4 <i>Interfacial force microscopy</i> | 8 |
| 1.1.5 <i>Molecular dynamics</i> | 9 |
| 1.2 Motivation | 10 |
| 1.3 Objective and Approach..... | 12 |
| CHAPTER TWO. EXPERIMENTAL TECHNIQUES..... | 13 |
| 2.1 Introduction | 13 |
| 2.2 Interfacial Force Microscopy | 14 |
| 2.2.1 <i>Interfacial force microscope</i> | 14 |
| 2.2.2 <i>Fabrication of IFM probe</i> | 17 |
| 2.2.3 <i>Operation of the IFM</i> | 19 |
| 2.3 Atomic Force Microscopy..... | 21 |
| 2.4 X-Ray Photoelectron Spectroscopy | 23 |
| 2.5 Ellipsometry | 25 |
| 2.6 Contact Angle Measurement..... | 28 |
| CHAPTER THREE. THIN ORGANIC FILMS | 30 |
| 3.1 Introduction | 30 |
| 3.2 γ -APS Films | 31 |
| 3.2.1 <i>γ-APS film deposition</i> | 31 |

| | |
|----------------------------------------------------------------|----|
| 3.2.2 <i>γ</i> -APS film thickness measurements | 32 |
| 3.3 Self-Assembly of ATS Monolayers | 34 |
| 3.4 Fabrication of Self-Assembled OTS Monolayers | 38 |
| 3.4.1 <i>Materials and substrate preparation</i> | 38 |
| 3.4.2 <i>Deposition of OTS films</i> | 40 |
| 3.4.3 <i>Patterning OTS films</i> | 41 |
| 3.5 Diagnostics for OTS Monolayers..... | 43 |
| 3.5.1 <i>Contact angle measurements</i> | 44 |
| 3.5.2 <i>Surface topography by AFM</i> | 45 |
| 3.5.3 <i>Ellipsometry measurements</i> | 46 |
| 3.5.4 <i>Patterned OTS films</i> | 46 |
| 3.5.5 <i>XPS, ISS characterization</i> | 49 |
| 3.5.6 <i>IFM nanoindentation</i> | 52 |
| 3.5.7 <i>Summary and discussion</i> | 53 |
| CHAPTER FOUR. ANALYSIS | 58 |
| 4.1 Introduction | 58 |
| 4.2 Contact Mechanics | 59 |
| 4.2.1 <i>Contact mechanics theories</i> | 60 |
| 4.2.2 <i>Elastic-plastic contact</i> | 64 |
| 4.2.3 <i>Contact of layered materials</i> | 66 |
| 4.3 Finite Element Analysis | 67 |
| 4.4 Molecular Dynamics | 69 |
| 4.5 Hypo-elastic Behavior | 72 |
| CHAPTER FIVE. RESULTS AND DISCUSSION | 74 |
| 5.1 Introduction | 74 |
| 5.2 Parametric Study of Layer and Substrate Interactions | 74 |
| 5.2.1 <i>Parametric study of substrate effects</i> | 75 |
| 5.2.2 <i>Parametric study of Poisson effects</i> | 77 |

| | |
|------------------------------------------------------------------------|-----|
| 5.2.3 Summary..... | 80 |
| 5.3 Analysis of Nanoindentation of γ -APS Films | 81 |
| 5.3.1 Nanoindentation of γ -APS films | 81 |
| 5.3.2 Classical contact mechanics analyses..... | 82 |
| 5.3.3 Finite element analysis..... | 87 |
| 5.3.4 Summary..... | 89 |
| 5.4 Analyses of Nanoindentation of OTS Self-Assembled Monolayers..... | 90 |
| 5.4.1 Nanoindentation of self-assembled OTS monolayers..... | 91 |
| 5.4.2 Sensitivity to layer thicknesses and mechanical properties | 93 |
| 5.4.3 Extraction of OTS modulus | 94 |
| 5.4.4 Molecular dynamics simulation of OTS compression..... | 96 |
| 5.4.5 Non-linear elastic analysis..... | 98 |
| 5.4.6 Summary..... | 101 |
| CHAPTER SIX. CONCLUSIONS | 103 |
| Tables | 109 |
| Figures..... | 118 |
| Bibliography..... | 182 |
| Vita | 194 |

List of Tables

| | |
|---------------------------------------------------------------------------------------------------------------------------|-----|
| 3.1: Samples of γ -APS film on silicon | 111 |
| 3.2: Water contact angle measurements | 111 |
| 3.3: Thickness measurements..... | 111 |
| 4.1: Elastic material properties..... | 112 |
| 4.2: Atomic weight..... | 112 |
| 4.3: Parameter for harmonic bond potentials | 113 |
| 4.4: Parameter for harmonic valence angle potentials | 113 |
| 4.5: Parameter for cosine dihedral angle potentials | 114 |
| 4.6: Inter-molecular interactions were represented by the short-range (van der Waals) Lennard-Jones pair potentials | 115 |
| 5.1: Contact mechanics analysis of the 4 μm thick γ -APS film on silicon | 116 |
| 5.2: Finite element analysis of γ -APS films on silicon | 117 |
| 5.3: Finite element analyses of OTS on silicon..... | 117 |

List of Figures

| | | |
|------|---------------------------------------------------------------------------------------------------------------------------------------------------------------------------------------------------------------------------|-----|
| 1.1 | Schematic of interfacial fracture of an epoxy/glass specimen. Crack grows in the interphase. | 119 |
| 1.2 | Comparison of the mixed-mode fracture envelopes of sapphire/epoxy with and without SAM. The SAMs were composed of 90%DTS-10%BrUTS and 45%DTS-55%BrUTS. [Mello 2004]. | 120 |
| 2.1 | The main components of the IFM device: IFM head resting on a vibration isolated table, the control electronics tower and a computer equipped with LabView data acquisition board and control software. | 121 |
| 2.2 | The head of the IFM. | 122 |
| 2.3 | Schematic of an interfacial force microscope (IFM). | 123 |
| 2.4 | Schematic of feedback control circuit of interfacial force microscope (IFM). | 124 |
| 2.5 | Setup for electrochemical etching of the tungsten tips. | 125 |
| 2.6 | SEM images of electrochemically etched tungsten tips: (a) overall shape, and (b) magnified view of the tip. | 126 |
| 2.7 | Displacement and force calibrations of the IFM. (a) Piezo calibration. The piezo gain is the slope of the linear fit. (b) Force calibration. The force gain of the sensor is extracted from the quadratic curve fit. | 127 |
| 2.8 | Schematic of an atomic force microscope (AFM). | 128 |
| 2.9 | The photoelectric process of X-ray photoelectron spectroscopy: (a) ejection of photoelectron and (b) subsequent emission of Auger electron. | 129 |
| 2.10 | Schematic of ellipsometry. | 130 |
| 2.11 | Contact angle of a liquid drop. Surface forces equilibrate at the corner. | 131 |
| 3.1 | Chemical reactions of γ -APS in H ₂ O. [Cabibil 2001] | 132 |
| 3.2 | Typical ellipsometry data for γ -APS (46 nm) on silicon. | 133 |

| | | |
|------|------------------------------------------------------------------------------------------------------------------------------------------------------------------------------------------------------------------------------------------------------------------------------------------------------------------------------------------------------|-----|
| 3.3 | (a) An AFM scan of a scratch on γ -APS on silicon. It was used to measure the thinner film thickness. (b) An AFM scan of a channel crack in γ -APS on silicon. This was used for measuring the thickness of the thicker γ -APS film. | 134 |
| 3.4 | Self-assembly model of OTS with cross-linking in the presence of water. | 135 |
| 3.5 | A three-dimensional representation of: (a), (b) the atomic structure of silica with hydroxyl groups ((a) side view and (b) plan view), and (c), (d) ATS chain on silica ((c) side view and (d) plan view) (O is red, Si is yellow, H is white and C is blue). [Stevens 1999]. | 136 |
| 3.6 | Self-assembly of OTS under anhydrous conditions. | 137 |
| 3.7 | Low force contact mode AFM images of an OTS-covered hydroxylated oxidized Si(100). The OTS was added under hydrous conditions. (a) Image of a region that is covered with visually observable patches and (b) image of region that is visually clear. | 138 |
| 3.8 | AFM images of OTS-covered hydroxylated oxidized Si(100). The OTS was added under anhydrous conditions. (a) Image of low force contact mode and (b) image of tapping mode. | 139 |
| 3.9 | For an OTS-covered substrate prepared under anhydrous conditions, an image taken at low force after scratching the surface in the central region of the figure with the AFM tip under the highest applied force available (1 μ N). A line scan is plotted beneath the image. | 140 |
| 3.10 | AFM images of micro-contact printing (μ CP) substrate: (a) silicon based master grid, (b) phase image of patterned OTS on silicon (100), and (c) non-contact topography image of the same patterned OTS. | 141 |
| 3.11 | Patterning OTS with convectively assembled polystyrene beads: (a) an optical microscope image of a Si(100) surface covered with convectively assembled 2 μ m diameter polystyrene beads; (b) ,(c) and (d) are the AFM images of different scan size that were gathered after depositing OTS, under anhydrous conditions, and removing the beads. | 142 |
| 3.12 | Comparison of AFM images (3 \times 3 μ m ²) that were taken at different times. The OTS was patterned using convectively assembled polystyrene beads: (a) immediately following post processing, (b) after 8 hours and (c) after 20 hours. | 143 |

| | | |
|------|----------------------------------------------------------------------------------------------------------------------------------------------------------------------------------------------------------------------------------------------------------------------------------------------------|-----|
| 3.13 | Broad XPS scan of OTS covered Si(100) surface. The peaks are all attributed as marked to either photoelectrons or Auger transitions, C(KVV) and O(KLL), on XPS transitions from C, O, and Si atoms with the XPS sampling depth. | 144 |
| 3.14 | XPS scans for: (A) piranha etched Si(100) surface prior to exposure to OTS, (B) surface exposed to OTS under anhydrous conditions, (C) surface from (B) exposed to 5 keV He ions for 300 s, and (D) surface from (C) exposed to 2 keV Ar ions for 120 s. | 145 |
| 3.15 | ISS for: (A) piranha etched Si(100) surface prior to exposure to OTS, (B) surface exposed to OTS under anhydrous conditions, (C) surface from (B) exposed to 5 keV He ions for 300 s and (D) surface from (C) exposed to 2 keV Ar ions for 120 s. | 146 |
| 3.16 | Force profiles that were taken on OTS-covered Si(100) surfaces prepared under: (a) anhydrous and (b) non-anhydrous conditions. Each of the panels superimposes four separate force versus distance curves measured at different points separated by between 10 and 20 μm | 147 |
| 3.17 | Schematic of structures of OTS moieties. (a) Cross-linked structure. Severe tilting is caused by sterically repulsive arrangement of two cross-linked OTS moieties covalently bonded through an Si-O-Si linkage to a silicon surface. (b) Densely packed OTS monolayer without cross-linking. | 148 |
| 4.1 | Schematic of IFM nanoindentation on layered materials. | 149 |
| 4.2 | Contact between two deformable spheres. $R_2 = \infty$ corresponds to the contact between a sphere and a half space. | 150 |
| 4.3 | Typical force profiles of elastic contact between two deformable spheres. | 151 |
| 4.4 | Force profiles produced by three contact mechanics theories. The differences are due to the different types of adhesive interactions that were invoked in the analyses. | 152 |
| 4.5 | Indentation involving plastic deformations showing a kink on the loading path and hysteresis between the loading and unloading paths. | 153 |
| 4.6 | Finite element mesh for contact analysis: (a) overall and (b) magnified view of the mesh close to the contact region. | 154 |

| | | |
|------|-----------------------------------------------------------------------------------------------------------------------------------------------------------------------------------------------------------------------------------------------------------------------------------------------|-----|
| 4.7 | (a) Cohesive zone model with normal adhesive interactions, (b) default ABAQUS force-separation relationship for contact surfaces and (c) user-defined triangular force-separation law..... | 155 |
| 4.8 | Plan view of the unit cell for the molecular dynamics simulation model of OTS on silica. Small solid circles represent oxygen atoms, large solid circles represent silicon atoms on a lower plane and the remaining open circles represent the silicon atoms with OTS molecules on them. | 156 |
| 5.1 | Parametric study of substrate effect: normalized indentation force vs. indentation depth for various film modulus for different probe sizes ($E_s=100$ GPa, $\nu_s = \nu_f = 0.2$, $t=50$ nm)..... | 157 |
| 5.2 | Parametric study of substrate effect: normalized contact radius vs. indentation depth for different probe size ($E_s=100$ GPa, $\nu_s = \nu_f = 0.2$, $t=50$ nm). | 158 |
| 5.3 | Parametric study of substrate effect: normalized indentation force vs. contact radius for various film modulus for different probe size ($E_s=100$ GPa, $\nu_s = \nu_f = 0.2$, $t=50$ nm). | 159 |
| 5.4 | Parametric study of Poisson's ratio effect for $R=2t$ ($t=50$ nm)..... | 160 |
| 5.5 | Parametric study of Poisson's ratio effect for $R=10t$ ($t=50$ nm)..... | 161 |
| 5.6 | Parametric study of Poisson's ratio effect for $R=100t$ ($t=50$ nm)..... | 162 |
| 5.7 | Parametric study of Poisson's ratio effect for different probe size ($\alpha = -0.9$). | 163 |
| 5.8 | ε_{22} strain contour for a tungsten indenter on a single film on a substrate ($E_s=96$ GPa, $\nu_s=0.2$)..... | 164 |
| 5.9 | The rate effect for loading and unloading on an ambient cured 46 nm γ -APS film on silicon..... | 165 |
| 5.10 | Hertz theory fit of a force profile from a 4 μm thick γ -APS film on silicon.... | 166 |

| | | |
|------|------------------------------------------------------------------------------------------------------------------------------------------------------------------------------------------------------------------------------------------------------------------------------------------------------------------------------------------------|-----|
| 5.11 | DMT theory fit of a force profile from a 4 μm thick γ -APS film on silicon: (a) a two-parameter fit Scheme I, (b) a two-parameter fit Scheme II and (c) a three-parameter fit Scheme III. | 167 |
| 5.12 | JKR theory fit of a force profile from a 4 μm thick γ -APS film on silicon: (a) two parameter fit, and (b) three parameter fit. | 168 |
| 5.13 | Maugis theory fit of a force profile from a 4 μm thick γ -APS film on silicon. | 169 |
| 5.14 | Finite element simulation of force profiles from: (a) a 4 μm thick γ -APS film on silicon, (b) an ambient cured, 46 nm thick γ -APS film on silicon and (c) a 100 $^{\circ}\text{C}$ cured, 46 nm thick γ -APS film on silicon. | 170 |
| 5.15 | A typical IFM force profile of bare silicon at the loading speed of 0.26 nm/sec: (a) original profile showing hysteresis of piezo elements at slow loading/unloading speed, (b) force profile after the adjusting the hysteresis, and (c) data is compared with finite element analysis using the known properties of silicon and silica. | 171 |
| 5.16 | A comparison of force profiles of bare silicon and silicon coated with an OTS monolayer. The loading paths in (b) and (c) have been shifted upward for clarification. | 172 |
| 5.17 | Parametric study of the effect of the thickness of the oxide layer on force profiles: (a) $\nu_{OTS}=0.0$ and (b) $\nu_{OTS}=0.44$ | 173 |
| 5.18 | Parametric study of the effect of the thickness of the OTS monolayer on force profiles: (a) $\nu_{OTS}=0.0$ and (b) $\nu_{OTS}=0.44$ | 174 |
| 5.19 | Parametric study of the effect of the OTS modulus on force profiles: (a) $\nu_{OTS}=0.0$ and (b) $\nu_{OTS}=0.44$ | 175 |
| 5.20 | A comparison of measured and predicted IFM force profile on OTS: (a) $\nu_{OTS}=0.0$ and (b) $\nu_{OTS}=0.44$. The insets emphasize the disagreement at low force levels. | 176 |
| 5.21 | Self-assembly of OTS from the molecular dynamics simulation. Blue= CH_2 and CH_3 united atoms, red=oxygen, turquoise=silicon. | 177 |

| | | |
|-------|-------------------------------------------------------------------------------------------------------------------------------------------------------------------------------------------------------|-----|
| 5.22 | The stresses in an infinite OTS monolayer under uniform compression by molecular dynamics simulation. The insets emphasize kinks in the response that are probably due to conformational changes..... | 178 |
| 5.23 | The extracted (a) tangent modulus and (b) Poisson's ratio for a hypo-elastic material based on the response obtained from the molecular dynamics analysis. | 179 |
| 5.24. | Comparison of the stress-strain behavior of OTS from the molecular dynamics simulation and hypo-elastic model: (a) the comparison at low strain levels and (b) complete range..... | 180 |
| 5.25 | Non-linear finite element analysis of the IFM experiment on OTS. The inset emphasizes the improved agreement at low force levels. | 181 |

CHAPTER ONE

INTRODUCTION

1.1 OVERVIEW

1.1.1 Interfacial fracture and interphase

The performance of composites, thin films, adhesives, and blends is directly linked to interfacial phenomena. In particular, understanding the relationship between surface chemistry and interfacial fracture phenomena in heterogeneous polymer systems will allow for improved lifetime modeling of such structures. In addition, it provides opportunities for controlling adhesive properties in a more direct manner. A growing body of experimental evidence has substantiated the existence of an interphase region and the important role the interphase region plays in the overall mechanical properties of polymer matrix fiber composites [Kim and Mai 1998, Kim et al. 2001]. The interphase is the region between the surface of the reinforcement and the polymer matrix where the chemistry is different from that of the bulk matrix [Drzal 1990, Rao and Drzal 1991, Madhuk and Drzal 1991]. The mechanical properties in the interphase are a direct reflection of the interphase chemistry. In addition, the level of adhesion at the reinforcement surface will influence the mechanical properties near the

interface. The stress transfer between the polymer matrix and the load bearing reinforcement takes place across the interphase and hence the interphase is critical for composite performance. Fourier transform infrared (FT-IR) spectroscopy has been used to substantiate the existence of an interphase region where the chemical composition varies from that of the bulk polymer matrix [Culler et al. 1983, Cossian et al. 1996, Lourie et al. 1997]. Micro-mechanical techniques have provided additional evidence of an interphase and have begun to elucidate the impact the interphase and interface adhesion have on the composites' overall mechanical properties [Williams et al. 1990, Meurs et al. 1996, Winter and Houston 1998 a, b]. Continuum mechanics analyses have clearly shown that the interphase plays an important role in the transverse properties of polymer composites, and to a lesser degree, in the unidirectional properties of polymer composites and the macroscopic elastic constants [Skala et al. 1994, Chouchaoui and Benzeggagh 1997].

A study by Swadener et al. [1999] revealed that interfacial fracture at a glass/epoxy interface occurred in an interphase region as far away as 3 nm from the glass surface. As a result, it is very important to determine the mechanical properties in such interphase regions. In the field of tribology, the mechanical behavior of layers having thickness between 1 and 100 nm affects the wear behavior significantly [Azarian and Bauer 1993, Khurshudov and Kato 1996, Li and Bhushan 1999, Bhushan, 1999 a, b]. It is important to understand the chemistry and mechanical properties of interphase regions because it is in this region where the stress is transferred. Studies of interfaces have indicated that the

transition region (the interphase) had different thermo-mechanical properties from those of the bulk material [Drzal 1990, Winter and Houston 1998 a, b, van Landingham et al. 1999.] and hence require micro- and nano-scale elucidation. These studies have demonstrated the need to obtain a much more fundamental understanding of the link between interphase chemistry and mechanical behavior during the application of a load. Nevertheless, the smallness of these regions poses challenges for the measurement of mechanical properties.

1.1.2 Self-assembled monolayers

Self-assembled monolayers (SAMs) refer to the spontaneous formation of an ordered organic film on an appropriate substrate by immersing the substrate in a solution of an active surfactant in an organic solvent [Ulman 1991]. Organic monolayers formed through self-assembly usually have a highly ordered structure [Ulman 1991, 1996, Kojio et al. 1998]. The functionality of the surface can be controlled by choosing different tail groups or chemical derivations of tail groups so as to alter and control the chemical and mechanical properties of surfaces [Ulman 1991]. Multiple layers can also be achieved by functionalizing the end group and then depositing another monolayer on top of the previous one [Ulman 1991, 1996]. SAMs have been the subject of intense study in the past decade because of their potential applications in controlling wetting, adhesion [Srinivasan et al. 1998, Maboudian et al. 2000], friction [Carpick and Salmeron 1997, Maboudian et al. 2002], chemical sensing [Chaki et al., 2002] and high-resolution lithography [Kumar and Whitesides 1993, Xia et al. 1995, 1998, Jeon et al. 1997].

These features allow SAMs to be tailored to particular applications. One potential is to tailor SAMs for studying the fundamental relationship between the interphase chemistry and mechanical properties. They have the potential to form well-defined interphases. A SAM or mixtures of SAMs with different functionalities have been used to create well-defined combinations of strong (specific) and weak (nonspecific) interfacial interactions [Zhuk et al. 1998, Reedy et al. 2002, Kent et al 2002, Mello and Liechti 2004] in interfacial fracture studies. In the latter study, it was found that fracture occurred in or slightly above the SAM, reinforcing the importance of understanding the nanomechanical behavior of such monolayers.

Alkyltrichlorosilane ($\text{CH}_3\text{-(CH}_2\text{)}_{n-1}\text{-SiCl}_3$, ATS) SAMs are of particular technological interest in microelectromechanical systems (MEMS) since most MEMS devices are based on silicon or SiO_2 . Atomic indentation and friction properties of SAMs are critical in MEMS and surface engineering [Maboudian 1998]. Octadecyltrichlorosilane (OTS) monolayer, which is one species of ATS, has been used to reduce the occurrence of release-related and in-use stiction phenomena in micromachined polysilicon devices [Srinivasan et al. 1998, Maboudian et al. 2000, Jun and Zhu 2003]. Its hydrophobic surfaces reduce the work of adhesion by several orders of magnitude compared to hydrophilic SiO_2 surfaces. The low friction of $-\text{CH}_3$ terminated SAMs largely comes from low surface energy due to their hydrophobic tail groups and high load bearing capacity due to their compact structures [Carpick and Salmeron 1997, Maboudian et al. 2002]. However, despite their technological importance, a complete

understanding of the self-assembly process of ATS is not well understood because the highly reactive of chlorosilane head group with water. Understanding the assembly process affects the choice of monolayer deposition method, the molecular structure, the monolayer quality and most importantly whether or not the film is a true monolayer.

In contrast to the ordered structure of self-assembled monolayers, thin amorphous (3-aminopropyl)triethoxysilane (γ -APS) films were also used as samples in this study. They were useful for developing the analysis of interfacial force microscope (IFM) force profiles. γ -APS is often used as a coupling agent to enhance the adhesion of composite materials [Plueddemann 1982, 1991]. It was the subject of a recent study by Cabibil et al. [2001] who used the IFM to determine the Young's modulus of γ -APS on glass and silicon. They found that the modulus of γ -APS on silicon was four times the value on glass. However, both values were unexpectedly high given the amorphous nature of the γ -APS films that were considered.

1.1.3 Nanoindentation and contact mechanics

Nanoindentation has become an accepted experimental technique for measuring the mechanical and adhesive properties of materials, especially when one of the dimensions is small. The indentation devices use either spherical or pyramidal indenters to probe the surfaces. During an experiment, the force and displacement are recorded. The forces and displacements of commercial

indentation instruments are typically in mN and nm ranges, respectively [Doerner and Nix 1986, Pharr et al. 1992, Oliver and Pharr 1992].

There have been great improvements in indentation devices in the last few years. These improvements allow forces in the range of μN to nN and displacements from nm to \AA to be measured with atomic force microscopes (AFM) and nanoindentation testers [Sawa et al. 1999]. Nanoindentation studies of ultra-thin films can be conducted with these higher resolutions. For example, AFM has been used to measure interphase nanoscale properties of polymer composites [van Landingham et al. 1999, Gao and Mäder 2002] and nanomechanical properties of metals [Hues et al. 1994] as well as surface force interactions [Cappella and Dietler 1999, Hodges 2002]. However, the calibration of cantilever stiffness and the geometry of the probe tip needs to be performed carefully. In addition, the AFM cannot measure surface interactions very well due to the mechanical instability that occurs when the force gradient exceeds the stiffness of the cantilever. The surface force apparatus (SFA) has a higher stiffness and has been used extensively to measure adhesive interactions [Israelachvili and Adams 1978, Israelachvili and Pashley 1984, Israelachvili 1992].

Classical contact mechanics solutions are commonly used to analyze nanoindentation experiments [Sneddon 1965, Johnson 1985, Maugis 2000]. The standard methods for extracting the mechanical properties from the measured force-displacement data were developed by Doerner and Nix [1986], Pharr et al. [1992], Oliver and Pharr [1992], and Field and Swain [1993]. These methods use

the unloading curve to derive the Young's modulus and hardness and should only be used for monolithic materials. The measurement of elastic modulus of thin films poses significant challenges due to the potential influence of the substrate. There are some analytical solutions [King 1987, Yu et al. 1990, Kim 1996 and Yoffe 1998] for indentation on layered materials. They are either mathematically complicated or for limited cases. To circumvent this problem, the local composite (i.e., film and substrate) elastic modulus is usually calculated from the initial part of the unloading curve and then extrapolated to zero indentation depth. Some empirical and semi-empirical formulae for extracting the elastic modulus of thin films have been summarized by Menčík et al. [1997]. Substrate effects are often ignored by following a common rule of thumb that the indentation depth should be less than a tenth of the film thickness [Bückle 1971, Fischer-Cripps 2000, Cabibil et al. 2001]. Based on this rule, the elastic modulus of organic films (γ -APS) on silicon and glass was extraordinarily high [Cabibil et al. 2001].

Another problem that arises in nanoindentation experiments, when the indentation load is low, is the effect of adhesive interactions. In practice, JKR theory [Johnson et al. 1971] or DMT theory [Derjaguin et al. 1975] or even the more generalized solution of Maugis [1992] is usually employed to account for the adhesive interactions. However, they have the same limitations as mentioned above in that they can only be applied to monolithic materials. As a result, the interpretation of nanoindentation experiments on thin, multi-layered materials requires the use of numerical methods.

1.1.4 Interfacial force microscopy

The interfacial force microscope (IFM) was developed in the early 90's [Joyce and Houston 1991, Houston and Michalske 1992]. It is a scanning force microscope similar to the atomic force microscope (AFM), but distinguished from it by its electro-statically driven, force feedback sensor. It can be used to perform both nanoindentation experiments and surface imaging. Since its invention, it has been used to measure the mechanical properties of thin organic films [Winter and Houston 1998 a, b, Cabibil et al. 2001, Burns 1999 a, b, Wang et al. 2004 a, b], for the study of surface force interactions [Thomas et al. 1993, 1994, 1995, Keily and Houston 1998], as well as to image surfaces [Warren et al. 1997]. In the present study, IFM was solely used to measure mechanical properties of thin films in nanoindentation experiments.

One of the key features of IFM is that the force sensor has “zero compliance” through the unique design of its sensor and feedback circuit. No deformation of the sensing element results from the act of measuring force. This “rigid” sensor does not store energy during measurement. Consequently, there is no mechanical instability over the entire probe-sample interaction. This is in contrast to some other devices such as the surface force apparatus (SFAs) and AFM in which springs with low stiffness are used as force sensors and the “snap-to-contact” and “snap-off” instabilities are unavoidable when the interaction force gradient is larger than the stiffness of the sensor.

When an IFM is used as a nanoindentation tester, it follows the entire force-separation response and the force and displacement are recorded directly. It

has sufficiently high resolution in both force and displacement measurements that it can be used to probe SAMs at low enough load levels that the force profiles are elastic. When both the indenter and surface are functionalized with SAMs, the adhesive properties for specific functional groups can be studied. Such studies can provide the fundamental governing relations between interphase chemistry and fracture mechanics in polymer-substrate systems.

1.1.5 Molecular dynamics

Molecular dynamics simulations can be used to explore the macroscopic properties of materials from atomistic levels. Molecular dynamics is a computer simulation technique where the time evolution of a set of interacting atoms is followed by integrating the equations of motion. In molecular dynamics simulations, the motions of individual atoms or molecules are computed based on Newton's equation of motion. Integration of these equations yields a trajectory that describes the positions and velocities of the particles with time. The state of the system can be predicted at any time and the average values of continuum quantities, such as stress and strain, can be determined from this trajectory.

Molecular simulations are a useful technique for studying the structural and mechanical behavior of self-assembled monolayers on the atomic or molecular level. Siepmann and McDonald [1993] used the Monte Carlo technique to study the mechanical relaxation of a $\text{CH}_3(\text{CH}_2)_{15}\text{SH}/\text{Au}(111)$ SAM subject to compression with a flat surface. Tupper et al. [1994 a, b] performed molecular dynamics analyses to simulate a SAM of *n*-hexadecanethiol chemisorbed on a

gold (111) surface and compressed uniformly by another Au (111) surface. Henda et al. [1998] used the static energy minimization technique to study the effects of force fields and monolayer structures on the calculated elastic properties. All the studies revealed that the variation in mechanical response was related to stress induced structural rearrangements. These models were quite simplified and the duration of the loading was very short compared to real indentation time scales. Nonetheless, because the force levels matched those of the experiments [Tupper and Brenner 1994, Henda et al. 1998], these simulations usefully explored the macroscopic properties of self-assembled monolayers from atomistic levels. However, the direct correlation between the molecular dynamics simulation and indentation experiments has not been reported in literature.

1.2 MOTIVATION

This project was motivated by previous work in interfacial fracture problems. Swadener and Liechti (1999) defined the energy dissipated in the fracture process zone associated with interface cracks as the intrinsic toughness, which was independent of mode-mix and, added to the plastic dissipation, yielded the measured toughness. This intrinsic toughness, which should have surface chemistry origins, was further identified with several components, such as surface energy, bond breaking and bond pullout and highly localized permanent deformation. This suggested that fracture was occurring in an interphase region (Fig. 1.1). From the continuum mechanics point of view, the intrinsic toughness can be represented by a force-separation law [Needleman 1987, 1990]. Mixtures

of self-assembled monolayers (SAM) have been used to control adhesion between the epoxy matrix and the substrate [Zhuk et al. 1998, Kent et al. 2002, Reedy et al. 2002] in the interfacial fracture studies. The effect of mixtures of two SAMs on the mixed-mode fracture toughness envelopes of sapphire/epoxy interfaces is shown in Figure 1.2 [Mello 2003]. Nevertheless, these “top-down” approaches [Hutchinson and Evans 2000], which couple continuum mechanics descriptions to phenomenology and experimental calibration at the smallest scales, left several questions unanswered: how do the mechanical properties of interphase differ from those of the bulk epoxy and why did the crack not run along the interface, which should have been the weak link? These studies require “bottom-up” approaches that link the properties at microscopic and molecular scale to the macroscopic aspects of deformation and fracture. Due to their highly ordered structure, SAMs may help answer some of these questions. The functionality of SAMs has the potential for better understanding the chemical nature of the intrinsic fracture toughness in interfacial fracture research. Such studies should provide a bridge between our understanding of mechanisms at the nanoscale to the engineering objective of predicting crack growth in and the durability of structural components. As a first step towards this “bottom-up” approach research, the mechanical properties of ultra-thin films of amorphous polymer and self-assembled monolayers will be studied.

1.3 OBJECTIVE AND APPROACH

The purpose of this work was to develop better-controlled interphase regions and study the mechanical behavior of such regions as a first step towards understanding interfacial fracture at smaller scales. An IFM was developed at UT Austin and used to conduct the nanoindentation experiments. By applying ultra low load levels, the IFM probed the films in the elastic range. Combined experimental and continuum analyses of IFM nanoindentation of thin films, which accounted for the layer/substrate and adhesive interactions, were developed. A hybrid continuum-molecular analysis was also developed for analyzing the nanoindentation of self-assembled monolayers.

CHAPTER TWO

EXPERIMENTAL TECHNIQUES

2.1 INTRODUCTION

In this chapter, the experimental techniques that were used in the study are described. These techniques include interfacial force microscopy (IFM), atomic force microscopy (AFM), scanning electron microscopy (SEM), X-ray photoelectron spectroscopy (XPS) equipped with ion scattering spectroscopy (ISS), ellipsometry and contact angle measurements. Both the chemical and mechanical properties of thin films and monolayers can be explored with this combination of surface and thin film characterization techniques.

Scanning probe microscopy constitutes a family of advanced techniques for surface analysis. In this study, the surface roughness and topology of organic thin films and monolayers were evaluated directly from AFM images. The mechanical properties were studied by conducting nanoindentation experiments with the IFM. SEM was mainly used to characterize the tungsten tip that was used as IFM probe. Thicknesses were measured with ellipsometry as well as with AFM scanning line analysis and XPS extrapolation. The contact angle test and XPS were mainly used to evaluate the surface chemistry properties, including surface wettability and chemical composition.

2.2 INTERFACIAL FORCE MICROSCOPY

In this section, the principle of operation of the IFM is explained in detail. This is followed by a description of the fabrication of the tungsten tip that was used as the IFM probe. Then the calibration and operation of the IFM device are outlined.

2.2.1 Interfacial force microscope

Figure 2.1 is a picture of the IFM system at UT Austin. It consists of a measurement head (Fig. 2.2) that is mounted on a vibration isolated table, a control tower that houses the electronic components and an SCXI interface to a computer, which is loaded with a National Instruments data acquisition board and control software programmed in LabView^{NI}. The whole system should be stationed in a quiet room to minimize ground vibration and acoustic noise. Figure 2.3 shows a schematic of the IFM measurement head, which is the central piece of the IFM. It consists of a force sensor that is mounted on a piezo scanner, a sample stage that is controlled by three piezo inchworms so as to position the sample in three directions. When conducting experiments, the sample stage was stationary and the piezo scanner moves the sensor to probe the sample. The piezo scanner is composed of two co-axial piezo tubes. The inside tube is one piece and can therefore only extend or retract along its axial direction. The outer tube is divided into four quadrants so that they can extend and retract (z-direction) as well as bend (x-, y-directions). The inside piezo tube is mainly for adjusting the position in the z-direction. It is the outer tube that controls the scanning movement. The

electronic components in the tower control the sensor, piezo scanner and inchworms. When all the control components have been setup manually, the experiments are then automatically controlled by the computer.

The heart of the IFM is a self-balancing force sensor, which functions with a differential-capacitance sensor (Fig. 2.3) and its electrical control circuits (Fig. 2.4). The sensor consists of a differential capacitor whose common plate has two pads that are initially parallel to the other two gold pads on the glass base of the sensor. The silicon common plate is suspended by a torsion bar. The torsion bar is designed such that it is stiff in bending (prevents vertical translation of the common plate) but very compliant in torsion (common plate rotates like a teeter-totter about the torsion bar). A sharp probe (100 to 300 nm radius) is mounted on one pad of the common plate, whose angular position is controlled by the feedback.

The IFM experiments are performed under displacement control. Any force interactions between the probe and sample will cause the common plate to rotate about the torsion bar, and therefore change the capacitance of the sensor. The feedback circuit then supplies a DC voltage to the sensor so as to move the common plate back to its original position and the feedback signal is directly proportional to the force.

The differential-capacitance force sensor is actually an active circuit that serves two separate functions — detection of the rotation of and the application of forces to the common plate. It accomplishes these functions via two power sources: a 1.0 MHz RF bridge-drive voltage applied in opposite polarities to the

two capacitor pads and a DC voltage V_0 applied to both pads (Fig. 2.4). The change in differential capacitance is measured by the 1.0 MHz AC bridge circuit. The imbalance signal is fed to a demodulator, which generates a DC voltage ΔV and feeds it back to the pad with the tip on it so as to balance the force and null the rotation. It is this feedback loop that makes the force sensor rigid during measurement. The interaction force can then be measured directly from the DC voltage following the formula

$$F = G_f \left(V_0 \times \Delta V - \frac{\Delta V^2}{2} \right), \quad (2.1)$$

where V_0 is the bias DC voltage, ΔV is the feedback voltage, and G_f is the force gain determined by the sensor configuration. Note that the relationship is not linear but has a quadratic term involving ΔV . The maximum repulsive force that can be applied to the probe is adjusted by the bias voltage

$$F_{\max} = G_f \frac{V_0^2}{2}. \quad (2.2)$$

In reality, there is another (small) DC voltage e_c that is applied to the sensor. This voltage physically balances the teeter-totter so that a zero bridge output is achieved when no force is applied. In essence, e_c accounts for any initial misalignment between the capacitor plates. As a result, Equation 2.1 needs to be modified and appears as

$$F = G_f \left[(V_0 + e_c) \Delta V - \frac{\Delta V^2}{2} \right]. \quad (2.3)$$

The value of G_f is normally between 1 and 2 for the current generation of sensors. In our experiment, it is calibrated using Equation (2.3), as will be described later. The value of V_0 is usually set to 10 to 30 volts. Consequently, the

quadratic term is small and can be neglected and can easily be corrected in data post analysis if large forces are applied.

2.2.2 Fabrication of IFM probe

To date gold, tungsten and silica probes have been used in IFMs. The IFM used in the present study uses electrochemically etched sharp tungsten tips as its probes. This section presents the details of the fabrication process and the characterization of the shape and dimensions of the tips.

Figure 2.5 is a picture of the setup for the electrochemical etching of tungsten tips. The electrolyte used in the electrochemical etching is potassium hydroxide (KOH) in deionized (DI) water ($>18\text{ M}\Omega$) solution (KOH:DI water=1:10 by weight). KOH pellets (EM Science) were dissolved in the DI water in a 30 ml volumetric glass beaker. The working electrode was a tungsten (W) wire (0.2 mm diameter, 99.95% purity, Goodfellow). A platinum (Pt) wire (0.2 mm diameter) loop with about <5 mm diameter was used as the counter electrode and immersed in the electrolyte. A DC power supply (B.L. Packer, Inc., Model 3634 power supply) applies voltage to the electrodes. The W wire is wired to the positive side, while the Pt wire loop is wired to the negative side of the power supply. The most uniform etching was achieved when the W wire was immersed in the solution and centered in the Pt loop. The DC power supply was operated in the constant current mode. The typical current was between 0.1-0.2 Amps. While etching, the voltage fluctuated from 4 to 15 Volts. The etching speed can be controlled by varying the electric current. Typical etching times were from 20 to

45 seconds. Small bubbles could be seen inside the loop. Etching was done when the circuit was open as the W wire broke off at a neck that was formed. The power supply was turned off before cutting and removing the upper part of the W wire. The newly etched W tips were rinsed with plenty of DI water.

The etched tips were then examined under optical microscope so that the shape and quality could be checked at low magnification (10-50 \times) as the first step in quality control. Only regular, symmetric and sharp tips were retained for further examination. The tips were then checked under a scanning electron microscope (SEM) for characterization. Figure 2.6a shows an SEM image of the overall shape of a regular W tip. Only parabolic tips with smooth surfaces would be used for future IFM experiments. The SEM was also used to measure the tip radius with the magnified view as shown in Figure 2.6b. Most tips had a parabolic shape at the end. It was found that only the very end of the tip was spherical. This was monitored following each experiment.

The Pt loop diameter, the Pt loop position relative to the surface of electrolyte and etching speed were the parameters that affected the shape, smoothness and sharpness of the tips. In addition, the water rinse needed be done thoroughly since contaminants could be seen under SEM when the tips were not fully rinsed. An overall 50% yield could be achieved by optimizing the etching parameters.

2.2.3 Operation of the IFM

There are several steps towards final operation of the IFM. The wiring and quality of new sensors needed to be checked optically and electrically. Only those with good transient response were kept for further use. The whole system was calibrated in several steps. This is critically important when absolute measurements are required. There are two independent calibrations — the displacement calibration, which is the calibration of the piezo scanner; and the force calibration, which is the calibration of the force gain G_f of the sensor. The operation of the IFM includes manually optimizing the RF frequency, balancing the bridge, adjusting the demodulator phase, and optimizing the transient response. After tuning the IFM controller, the device is ready for operation.

Since the IFM was used solely for nanoindentation in the present study, the piezo scanner was only calibrated in the z-direction. The calibration was performed by manually applying equal voltage increments to all four quadrants of the piezo tube. The displacement was monitored by a high-resolution displacement gage (Model EHE-2056, Federal Products Co.) with a resolution of 10 nm. The applied voltage was measured by a multimeter and the recorded displacement was plotted against the voltage as shown in Figure 2.7a. The slope of linear response was the displacement sensitivity of the piezo scanner.

The purpose of the force calibration is to determine the relationship between PID voltage and the actual force applied to the tip, i.e. G_f in Equation 2.3. A 0.04 in. diameter Pt ball was mounted on a highly sensitive balance (Denver Instruments Model XE-50 with a range of 500 μ N and a resolution of 1

μN). After tuning the IFM controller to ready status, the sensor was moved towards the Pt ball so that it pressed against the pad of the teeter-totter to which feedback was being applied. In order to make stable measurements, the Pt ball was cleaned with a piranha solution (96% H_2SO_4 : 30% H_2O_2 =1:2 by volume) to remove any organic contaminants and dried with canned gas duster. The actual force reading of the balance and the PID voltage were recorded and plotted for each set-point value (Figure 2.7b). The value of G_f was then extracted by a least squares curve fit of the actual force vs. PID voltage ΔV using Equation 2.3.

A tungsten tip with desired shape and radius was then glued to one pad of the teeter-totter to which the feedback was applied using silver epoxy (Dynaloy 325, Part A:Part B=1:1 by volume, Dynaloy, Inc.). The epoxy was cured at 60°C for two hours. A special rig was designed to fix the W tip in position during the curing process. This step was performed on the vibration-isolated table because the common plate is so delicate. Another special rig was designed to hold the sensor with tungsten probe for SEM examination before and after each experiment. Only those experiments that did not cause any damage to the tip are reported.

Finally, an overall calibration of the instrument was conducted by checking the Young's modulus of fused silica and sapphire (Meller Optics, Inc.). The calibration samples have to be treated with piranha solution to remove any surface contaminants prior to calibration. The IFM that was used in this study is capable of measuring normal forces from 1 nN to 400 μN . Other values can be selected by altering the DC voltage V_0 (Eqn. 2.2) thereby changing the nominal

force resolution. The normal displacement resolution is about 0.01 nm. The feedback response time is approximate 500 microseconds.

2.3 ATOMIC FORCE MICROSCOPY

The atomic force microscope (AFM) uses a sensor that is composed (Fig. 2.8) of a sharp tip on the bottom side of the free end of a miniature compliant cantilever to scan over the surface [Binnig et al. 1986]. A laser light is positioned on the topside of the cantilever and reflected to a position-sensitive photodetector (PSPD). The scanning is controlled by piezo electric elements. The PSPD is a four-quadrant photodetector that determines the position of the reflected laser spot, which corresponds to the bending and torsion deformation of the cantilever. Initially, the reflected laser spot is centered on the PSPD. As the cantilever deforms, the position of the laser spot on the PSPD shifts. Signal $(A+C)-(B+D)$ in PSPD reflects the deflection of the cantilever, while $(A+B)-(C+D)$ signal always reflects the torsion of the cantilever, which reveals the friction between the tip and sample. The shift of the laser position in PSPD is directly proportional to the force between the tip and sample. The device operates in the contact, non-contact or tapping mode. In the first mode, the deflection of the cantilever is kept constant so that the movement of the tip follows the topology of the sample. In the non-contact or tapping mode, the tip oscillates above the surface and the amplitude is maintained at a constant value. The AFM can also be used as a nanoindentation instrument when the feedback is

turned off. The force can be calculated from the $(A+C)-(B+D)$ signal along with a good calibration of the cantilever stiffness.

The AFM tips are micro-fabricated from silicon (Si) or silicon nitride (Si_3N_4) with radius typically in the range from 10 to 50 nm. The cantilever has a shape of either triangle (V-shape) or rectangular (100-450 μm long, and 1-4 μm thick). The range of the cantilever spring constants (0.01-50 N/m) allows AFMs to scan many different materials with different operating modes.

Although the AFM is mainly a surface-imaging tool, due to its multiple operating and imaging modes, it has developed into a multifunctional technique suitable for characterizing the topography, adhesion, mechanical and friction behaviors, and other properties on scales ranging from hundreds of micrometers to nanometers [Magnov and Reneker 1997, Noy et al 1997]. By applying ultra low forces or even working in tapping or non-contact mode, the AFM is an ideal instrument for imaging soft polymer surfaces [Magnov and Reneker 1997]. The AFM has even been used to write patterns on polymer films by using higher forces [Nakagawa et al. 1994, Cabibil et al. 2000].

In this study, AFM studies were performed with Park Scientific Instruments Autoprobe M5 and Autoprobe CP instruments. AFMs were used to check the morphology of surfaces, to pattern self-assembled monolayers by performing scratch and to provide height profiles through line analyses.

2.4 X-RAY PHOTOELECTRON SPECTROSCOPY

X-ray photoelectron spectroscopy (XPS) is widely used to investigate the chemical composition of surfaces. Surface analysis by XPS is accomplished by irradiating a surface with mono-energetic soft x-rays and analyzing the energy of the emitted electrons. Mg K α (1253.6 eV), Al K α (1486.6 eV), or monochromatic Al K α (1486.7 eV) x-rays are usually used because these energy levels are high enough to activate most of the chemical elements. These x-ray photons have a penetration depth in a solid on the order of 1-10 μm . They interact with atoms in the surface region, causing photoelectrons emitted in the photoelectric process (Fig. 2.9a) and Auger electrons emitted due to the relaxation of the excited ions remaining after photoemission (Fig. 2.9b). The emitted electrons have measured kinetic energies given by

$$KE = h\nu - BE - \phi_s \quad (2.4)$$

where $h\nu$ is the energy of the X-ray photon, BE is the binding energy of the atomic orbital from which the electron originates, and ϕ_s is the spectrometer work function.

The electrons leaving the sample are detected by an electron spectrometer according to their kinetic energy. The spectrum is obtained as a plot of the number of detected electrons against the binding energy per energy interval. Although the path length of the photons in a solid is of the order of micrometers, only those electrons that originate within tens of angstroms below the solid surface can leave the surface without energy loss. These electrons produce peaks

in the spectra and are the most useful. Thus, XPS is widely used to investigate the chemical composition of surfaces up to a depth of several nanometers.

Because each element has a unique set of binding energies, XPS can be used to identify and determine the concentration of the elements in the surface. Variation in the elemental binding energies (the chemical shifts) arises from difference in the chemical potential and polarizability of compounds. These chemical shifts can be used to identify the chemical state of the materials being analyzed. Quantitative data can be obtained from peak heights or peak areas, and identification of chemical states can often be made from exact measurement of peak positions and separations, as well as from certain spectral features. For a typical XPS investigation where the surface composition is unknown, a broad scan survey spectrum should be obtained first to identify the element present. Once the elemental composition has been determined, narrower detailed scans of selected peaks can be used for a more comprehensive picture of the chemical composition.

Most XPS are equipped with ion guns so as to perform ion sputter-etching or collecting ion scattering spectrum (ISS). The XPS and ion scattering (ISS) data were gathered using a commercial X-ray photoelectron and ion scattering spectrometer (PHI 3057) equipped with a hemispherical electron and ion energy analyzer. For XPS, Mg K α X-rays were used, taking spectra at a pass energy of 58 eV. For ISS, 1 keV He⁺ ions were used and the analyzer pass energy was 375 eV. The analyzer accepted charged particles from the same a 3×3 mm² area for both XPS and ISS. Sputtering was done with either 5 keV He⁺ or 2 keV Ar⁺. A

single time-of-flight secondary ion mass spectrometry (TOFSIMS) experiment was performed (PHI 7200) using 8 keV Cs⁺ ions.

2.5 ELLIPSOMETRY

Ellipsometry is a sensitive and convenient optical technique for determining the thickness of thin films. Its name is derived from the fact that plane polarized light reflected from a surface becomes elliptically polarized. The change in the polarization state of the light reflected from the surface of a sample is related to the thickness and optical properties of the film. Figure 2.10 shows a schematic of ellipsometry. The measured values are expressed as the relative amplitude change Ψ , and the relative phase change Δ as functions of the wavelength of the incident beam. These values are related to the ratio of Fresnel reflection coefficients R_p and R_s for p - and s -polarized light, respectively,

$$\rho = \frac{R_p}{R_s} = \tan(\Psi) e^{i\Delta} \quad (2.5)$$

where the p -plane is the incident plane and s -plane is orthogonal to it. The complex Fresnel reflection coefficients for the p - and s -directions are defined, respectively, as

$$R_p = \frac{E_p^{reflected}}{E_p^{incident}} \quad (2.6)$$

and

$$R_s = \frac{E_s^{reflected}}{E_s^{incident}} . \quad (2.7)$$

Ellipsometry measurements can be very accurate and reproducible because ellipsometry measures the ratio of the two values and includes both amplitude and

phase information. The sensitivity of an ellipsometer is so high that a change in film thickness of a few angstroms can be easily detected. With the appropriate optical model of the sample, it can be used to measure the thickness of layered samples. In this work, ellipsometry measurements were performed with an M44 spectroscopic ellipsometer with WVASE32TM software (J. A. Woollam Co., Inc). Both Ψ and Δ were acquired as functions of the wavelength of the incident beam with values ranging from 600 nm to 1100 nm. An optical model was developed that accounted for the multiple layers and compared with the experimental data. Unknown parameters in the optical model, such as thin film thickness, were then derived from regression algorithms.

In principle, for films with thickness > 5.0 nm, ellipsometry can determine both thickness and the refractive index. However, care must be taken in measuring the thickness of ultra-thin films, such as monolayers because ellipsometry is a model-dependent technique. The measured quantities determined from experimental data depend on the optical properties used in the mathematical model for ultra-thin films. The actual “measured” film thickness from the regression fit is the optical thickness of the film, i.e. the product of the film thickness and refractive index. Any change in the refractive index of the film yields a corresponding change in the estimated thickness. In addition, any surface roughness could affect the thickness measurements. However, small variations of optical constant, such as refractive index, have very little effect on the measured thickness. Ulman (1991) suggested $n = 1.5$ for monolayers of alkyl chains. A

small variation was also proposed for different chain lengths. The value $n = 1.45$ was suggested for molecular chains with less than 9 carbon atoms.

The optical constants of polymer films can be estimated using the additive group contribution method. The underlying idea of this method is that the physical properties of a compound are in some way determined by a sum of the contributions made by the structural and functional groups in the molecule or in the repeating unit of the polymer [van Krevelen 1990]. The group contribution concept has proved to be extremely useful for studying the correlation between the chemical constitution of substances and their physical properties. Light refraction can be calculated based on the molar refraction. Several major definitions of molar refraction have been proposed in the literature [van Krevelen 1990]:

a) Lorentz and Lorenz's definition

$$R_{LL} = \frac{n^2 - 1}{n^2 + 2} \frac{M}{\rho} \quad (2.8)$$

b) Gladstone and Dale's definition

$$R_{GD} = (n - 1) \frac{M}{\rho} \quad (2.9)$$

c) Volgel's definition

$$R_V = nM \quad (2.10)$$

d) Looyenga's definition

$$R_L = (n^{2/3} - 1) \frac{M}{\rho}, \quad (2.11)$$

where n is the index of refraction, M is the molar mass, ρ is the density, and R is the molar refraction. Definitions of b) and c) are purely empirical combinations,

a) has its theoretical basis in the electromagnetic wave theory of light, and d) is a simpler approximation of a). However, calculations show that the simple formula of Vogel gives the same results as the other complex formulas [van Krevelen 1990]. The values of molar refraction of alkyl (-CH₂-) and methyl (-CH₃) are given in Table 2.1.

2.6 CONTACT ANGLE MEASUREMENT

Contact angle is a measure of wettability, which is measure of the degree to which a fluid spreads on a surface. The shape of a liquid drop (Fig. 2.11) on a homogeneous surface is affected by the free energy of the interfaces through Young's equation

$$\gamma_{LV} \cos \theta = \gamma_{SV} - \gamma_{SL}, \quad (2.12)$$

where θ is the contact angle, γ is the surface free energy, and the subscripts LV , SV , and SL refer to liquid-vapor, solid-vapor, and solid-liquid interfaces. As a result, the contact angle is a measure of the chemical composition of a surface and the degree of molecular ordering present [Bain et al 1989, Ulman 1991].

For some two-component heterogeneous surfaces, the composition can be related by Cassie's equation

$$\cos \theta = f_1 \cos \theta_1 + f_2 \cos \theta_2, \quad (2.13)$$

where f_1 and f_2 are the fractional areas occupied by components 1 and 2, respectively. However, in general, $\cos \theta$ is not linearly dependent on the surface composition.

In this study, static contact angles of water on film surfaces were measured using Ramé-Hart NRL 100 goniometer. The results of contact angle measurements should reveal the chemical nature of the surface.

CHAPTER THREE

THIN ORGANIC FILMS

3.1 INTRODUCTION

In this chapter, the fabrication and characterization of thin organic films and self-assembled monolayers are described. The thin films were (3-aminopropyl)triethoxysilane (γ -APS) with thicknesses from 40 nm to 4 μ m. They were spin-coated on silicon substrates. These thin organic films were used as samples for developing a suitable continuum mechanics analysis procedure for IFM nanoindentation experiments, which will be given in Section 5.2. The fabrication and characterization of self-assembled monolayer of octadecyltrichlorosilane (OTS) on Si(100) are described and discussed in detail because self-assembled monolayers with high quality and reproducibility are required for IFM nanoindentation experiments. In this study, we took an entirely new approach using well-hydroxylated Si(100) surfaces and strictly anhydrous deposition conditions in order to minimize defects. Surface topological, chemical and mechanical properties were characterized with an array of techniques.

3.2 γ -APS FILMS

In this section, we describe the deposition and processing of the γ -APS films. Several schemes for measuring the thickness of the films are then presented.

3.2.1 γ -APS film deposition

γ -APS ($C_9H_{23}NO_3Si$ 99%, Aldrich Chemical Co.) is a standard coupling agent for adhesive bonding and fiber/polymer matrix bonding in composite materials [Plueddemann 1982, 1991]. The γ -APS was deposited on a single crystal silicon (100) surface by spin coating for thickness control. The deposition process included cleaning the silicon surface, making a γ -APS solution and film deposition and curing.

Silicon chips with dimensions $10 \times 10 \text{ mm}^2$ were cut from a polished p-type single crystal silicon wafer (100) with a thickness of approximately $645 \mu\text{m}$ (MEMC Electronic Materials, Inc). They were then soaked in acetone and ultrasonicated for 45 minutes to eliminate organic contaminants. Next, they were placed in a piranha solution (96% H_2SO_4 : 30% H_2O_2 =2:1 by volume) at 100°C for 15 minutes for further cleaning. The final cleaning step was a rinse with plenty of deionized water ($>18\text{M}\Omega \text{ cm}^{-1}$), followed by drying in a pure nitrogen stream. A 5%wt mixture of γ -APS in deionized water ($>18\text{M}\Omega \text{ cm}^{-1}$) was prepared in a clean container. Figure 3.1 shows the detailed chemical reactions of γ -APS in H_2O . The γ -APS molecules are quickly hydrolyzed and form trisilanol and the byproduct ethanol (CH_3CH_2OH). The reactive trisilanol species will condense

with each other to form oligomerized networks and water [Cabibil et al. 2001]. The solution was stored for more than 7 days prior to deposition so that the γ -APS monomers then fully polymerized. This step also minimized any covalent bonding between γ -APS and the silicon surface and allowed us to study an amorphous polymer.

The film was spin-coated onto the silicon substrate. Varying the spinning speed and duration produced films of different thickness. Spin-coating at low speeds (<1000 rpm) usually resulted in non-uniform films, particularly when immediately followed by a high temperature (100 °C) cure. In our study, two film thicknesses were chosen (46 nm and 4 μ m). The thinner γ -APS film was made by spin-coating at 2000 rpm for 50 seconds, whereas the thicker film was made by applying drops of γ -APS solution on the silicon surface without spin-coating.

When the coated silicon chip was first cured under ambient conditions followed by curing at 100 °C, the films had a uniform thickness. In our film preparation, all films were first cured under ambient condition for more than 5 hours, and then heated to 100 °C for another 3 to 5 hours. For the thick films, channel cracks formed following the elevated temperature cure. Further heating would delaminate the film from the substrate. Consequently, the curing time at high temperature was shortened to 3 hours so that no delamination would occur.

3.2.2 γ -APS film thickness measurements

An accurate measurement of film thickness is critical in the determination of the mechanical properties of thin films. This is particularly challenging for thin

and ultra-thin films. The thickness of the thin γ -APS films was measured with ellipsometry and AFM. The thickness of the thick γ -APS films was determined by AFM only.

Silicon wafers usually have a thin native oxide layer on the surface formed either due to the natural passivation in air or in the production. Therefore, in our study there were actually two layers of thin films on the silicon: γ -APS and SiO_2 . The thickness of the native SiO_2 was 1.9 ± 0.1 nm determined by ellipsometry. The measured value was the same as the thickness (2.0 nm) determined by XPS [Cabibil et al. 2001] and other reports in the literature [Shirafuji and Tachibana 1994, Garnier et al. 2003]. The consistency of the measurements could be due to the self-passivation of the oxidation process.

Since the thickness was relatively large for the thin γ -APS films (46 nm), both film thickness and optical constants (refractive and dispersion indices) can be determined from the ellipsometry measurements. Figure 3.2 is a typical set of ellipsometry data for a 46 nm thick γ -APS film on silicon. For the AFM measurement, a sharp tungsten tip was used to scratch the film surface. The force was controlled so that the tip would scratch away the γ -APS but leave the silicon intact. The AFM was then used to scan across the resulting groove in the γ -APS. The depth of the groove should match the thickness of the γ -APS film. Figure 3.3a shows an AFM scan of a scratch on γ -APS on silicon. The thickness measured in this way was compared with an ellipsometry measurement. The difference was less than 1 nm. The thickness of thicker γ -APS film was only measured by AFM. We used AFM to measure the depth of channel cracks formed

by high temperature cure. The result is shown in Figure 3.3b. The thickness measured in this way was $4\pm 0.5\ \mu\text{m}$.

The γ -APS films on silicon that were considered in this study are summarized in Table 3.1. Three samples were prepared. They differ in either thickness or cure temperature.

3.3 SELF-ASSEMBLY OF ATS MONOLAYERS

The alkyltrichlorosilanes (ATS, $\text{CH}_3\text{-(CH}_2\text{)}_{n-1}\text{-SiCl}_3$) are a family of chemical monomers that can form stable self-assembled monolayers (SAM) on silica surfaces. The ATS precursor molecule has three parts: the head group (-SiCl_3 , chlorosilane) that provides chemisorption to the substrate, the tail group (-CH_3 , methyl) providing a surface with the desired physical and chemical properties, and the alkyl chain $(\text{CH}_2)_n$ that links the two and makes a significant contribution to the mechanical properties of the SAM. The head group can form covalent Si-O-Si bonds with silica substrates terminated with hydroxyl groups (Si-OH). However, in the presence of water, it is possible for Si-O-Si cross-linking between molecules to occur. In this study, the self-assembling molecule was octadecyltrichlorosilane (OTS, $n=18$).

Predictable structure and repeatable production of self-assembled monolayers are typically desirable in applications of SAMs. However, these desirable features remain elusive for ATS monolayers. There are mainly two schools of thought about the self-assembly process. Sagiv [1980], Maoz and Sagiv [1984] suggested a structural model for ATS on silicon, in which the ATS

molecules form covalent bonds to the silicon as well as cross-links to each other. On the other hand, Stevens [1999] proposed a different structural model where the ATS molecules covalently bond to the silicon without cross-linking.

In order to form a structure according to the first model, the deposition of OTS monolayers involves the successive processes (Fig. 3.4) of: (1) hydrolysis, (2) adsorption and (3) polymerization with the elimination of water. This model has been widely used to explain the stability of the OTS monolayers. According to this model, water must be involved for the hydrolysis to occur. However, the presence of water has led to poor monolayer formation [Kluth et al. 1997, Bunker et al. 2000]. Angst and Simmons [1991] suggested a compromise where the polymerized OTS film had occasional covalent bonds with substrate. Silberzan et al. [1991] suggested that, although uniform Langmuir-like films may form on the substrates, there is no covalent bonding to the substrate. However, the reproducibility of this kind of monolayer is still low. The quality of such monolayers is very sensitive to reaction conditions, such as the water content and deposition temperature as reviewed by Ulman [1996]. Some authors have pointed out that cross-polymerization is difficult over large areas due to steric hindrance [Kessel and Granick 1991, Ulman 1991,1996, Carpick and Salmeron 1997, Stevens 1999]. This is because the Si-O-Si bond is shorter than the van der Waals radii of the interactions between molecular chains and would therefore cause severe slanting of the chains (not shown in Fig. 3.4 (3)). This would further inhibit lateral polymerization. Thus, polymerization will cause the formation of

clusters and result in non-uniform SAM. This early model does not explain the formation of uniform ATS monolayers over large areas [Stevens 1999].

Stevens [1999] studied the structure of self-assembled monolayers of ATS using three-dimensional molecular modeling. He used the mineral tridymite with hydroxyl groups on the outmost Si atoms as a model substrate. The silicon and four surrounding oxygen atoms form SiO_4 tetrahedrons (Fig. 3.5a). The plan view shows that the silicon atoms formed hexagonal pattern (Fig. 3.5b) with SiO_4 tetrahedrons alternating between pointing up and down around a given hexagon. This model resulted in three silicon atoms on a higher plane and three others on a lower plane around the hexagon. The silicon atoms on the higher plane were terminated with hydroxyl (Si-OH) groups. This arrangement resulted in 1 OH/20-25 \AA^2 , which was in agreement with the experimental values of 1 OH/20 \AA^2 [Zhuralev 1987]. It was concluded that, if every OH group reacted with ATS, a densely packed monolayer could form provided there was no cross-linking. Instead of cross-linking, each ATS molecule formed covalent Si-O-Si bond with the silicon surface with two OH pendant groups (Fig. 3.5c,d).

With cross-linking by forming Si-O-Si bonds between the silane species, steric repulsions between the hydrocarbon chains of the silanes would preclude the formation of densely packed monolayer. This can be explained with the molecular modeling study. For a typical Si-O bond length of 0.16 nm, the maximum distance between Si atoms would be 0.32 nm. Since the van der Waal's diameter for C is 0.35 nm and for H bonded to C is 0.25 nm, intense steric repulsion between the alkyl chains are expected. Consequently, cross-linking

would force the alkyl chains to tilt significantly and therefore prohibit other ATS molecules to react with adjacent OH groups. Thus, in order to form fully covered and uniform ATS monolayers, cross-linking should be avoided.

Control of the film structure depends critically on the amount of water present. Previous literature indicates that, in the presence of moisture, there is a competition between the reactions of cross-polymerization and covalent anchoring of molecules on hydroxylated surfaces. The former causes the formation of clusters and therefore lowers the reproducibility and quality of OTS monolayers. In addition, OTS monolayers have been deposited on mica where there are no covalent bonds. However, in some cases the thickness of these films were not uniform [Kessel and Granick 1991, Parikh et al 1995]. In other cases, the films could easily be removed from the mica [Nakagawa and Ogawa 1994]. When relatively large amounts of water (hydrous solution and glove box, 1-10% RH) were present during the deposition of OTS on Si(100), clusters (mm in size) of OTS were observed, which could not be removed with a chloroform tissue wipe [Vajapeyajula 2002, Winter, 2002]. This suggests that these clusters were occasionally covalently bonded to the substrate. On the other hand, when deposition was conducted with a hydrous solution in a dry box (oxygen and H₂O < 1 ppm), similar sized clusters, which are physisorbed on top of an OTS film (not necessarily a monolayer), could be easily removed by a chloroform tissue wipe [Vajapeyajula 2002].

These previous results and Stevens' model suggested that one further step needed to be taken in order to avoid the formation of clusters — making use of

anhydrous solution in a dry box. This would inhibit cross-linking and promote anchoring of the OTS molecules directly on the silicon surface. The formation of close-packed monolayers also relies on well-hydroxylated surfaces. Under these conditions, monolayers with full coverage over large areas should result. In the present study by following the process as shown in Figure 3.6, such a process was developed as described in the next section.

3.4 FABRICATION OF SELF-ASSEMBLED OTS MONOLAYERS

In this section, a new approach for the deposition of OTS monolayers on silicon is presented. Due to its high reactivity with moisture, the OTS film deposition was conducted with anhydrous solutions and well-hydroxylated Si(100) surfaces in a dry-box. For comparison, OTS films deposited under hydrous conditions with addition of water were also made. Patterned OTS films on silicon, in which part of the silicon was covered with OTS and the rest was left bare, were fabricated in an attempt to measure the thickness of self-assembled OTS monolayers. These patterns could then be characterized with an atomic force microscope (AFM).

3.4.1 Materials and substrate preparation

The substrates used for the OTS deposition were polished boron p-type single crystal silicon (100) wafers with radii of 100 mm and thickness 605-645 μm (MEMC Electronic Materials, Inc). Anhydrous OTS ($\text{CH}_3\text{-(CH}_2\text{)}_{17}\text{-Si-Cl}_3$ 90+%), dicyclohexyl ($\text{C}_{12}\text{H}_{22}$ 99%) and hexane (C_6H_{14} , 99%) were purchased

from Sigma-Aldrich, Inc. The latter two were used as solvents. Deionized (DI) water ($>18\text{ M}\Omega$), acetone, dilute hydrofluoric (HF) acid (HF:DI H_2O =1:36 by volume), piranha solution (mixture of 2 parts concentrated (96%) H_2SO_4 and 1 part H_2O_2 (30% in H_2O) by volume), carbon tetrachloride, toluene, ethyl alcohol were used either for the substrate preparation or post-deposition cleaning. Sylgard Silicon Elastomer 184 and Curing Agent 184, provided by Dow Corning Corp*, were used to make the stamp for patterning OTS by micro-contact printing (μCP). A master grid on a silicon wafer, which has regions of different line features with pitches of 6 to 50 μm , was used for casting the stamp. It was made using standard photolithographic fabrication.

The preparation of the silicon surface followed the same process for all the OTS film depositions described below. Silicon chips with dimensions $10\times 10\text{ mm}^2$ were cut from a silicon wafer. They were then bathed in acetone and ultrasonicated for 45 minutes to eliminate organic contaminants. Silicon wafers usually have a thin native oxide layer on the surface formed due to either natural passivation in air or in production. This native oxide layer could be contaminated and inconsistent. As a result, the silicon chips were dipped in the dilute hydrofluoric acid in a Teflon container for 40 seconds to remove the original native oxide layer. Next, the silicon chips were rinsed with deionized water and placed in a piranha solution in a Pyrex glass beaker at 90 to 100 $^\circ\text{C}$ for 15 to 30 minutes. The piranha solution oxidizes and hydroxylates the silicon surface. After this step, a new oxide layer was formed whose surface was terminated with

* The authors wish to thank Dow Corning Corp. for the free samples that they provided.

hydroxyl groups (-Si-OH). The final cleaning step was a rinse with plenty of DI water ($>18 \text{ M}\Omega \text{ cm}^{-1}$), followed by drying in a pure nitrogen stream. The prepared silicon chips were then ready for OTS deposition. The thickness of the new oxide layer was 2 nm as determined by ellipsometry. This sacrificial etching and re-oxidation process prepared consistent, well-hydroxylated silicon substrates for OTS deposition.

3.4.2 Deposition of OTS films

For comparison purposes, the OTS films were prepared on hydroxylated substrates using two different methods. They differed in their deposition environments. In the first process, deposition was accomplished under ambient conditions with the addition of controlled amounts of water sufficient to stoichiometrically replace Cl by OH in OTS solution. In the second process, anhydrous, dry-box conditions were used with anhydrous OTS solutions. For both methods, the deposition began with the preparation of a millimolar solution of OTS in bicyclohexyl. The mixture was shaken and stirred for a minute, then allowed to stay undisturbed for about another two minutes. Then the silicon chip was placed in the OTS solution with the polished side facing up. After 24 hours, the chip was transferred to CCl_4 . Several post-processing steps consisting of sonication in different solvents were conducted to remove or reduce the physisorbed OTS clusters that might have not been removed in the CCl_4 solution. These procedures left the chemisorbed OTS intact. The chip was sonicated for 15 minutes in each of the following sequence of solvents: CCl_4 , toluene, ethyl

alcohol and DI water. Finally the coated silicon chip was dried in a pure nitrogen stream.

The distinguishing features of each process were as follows. For the first method, not only was the deposition accomplished in ambient atmosphere, but a stoichiometric amount of water was also added with stirring in order to hydrolyze the OTS. After sonication, drying and storage, as described above, the sample was analyzed. Visual inspection revealed patches that were later identified by AFM as regions with large numbers of clusters. By contrast, for the second method, the deposition of OTS was conducted in a dry box (H_2O and $\text{O}_2 < 1$ ppm) using an anhydrous mM OTS solution. After deposition, the sample was transferred while still in the dry-box to a bottle containing CCl_4 . The bottle was closed before removal from the dry-box. Visual and AFM inspection revealed no evidence of clusters and the samples, stored in closed vials, were stable over at least twelve months.

3.4.3 Patterning OTS films

Patterned samples were made using two methods: micro-contact printing (μCP) and convectively assembled polystyrene beads. For both, OTS was added under anhydrous (dry-box) conditions using anhydrous solutions. The detailed procedures of these two methods are described below.

The μCP method was developed by Whitesides' group at Harvard [Kumar et al. 1993, Xia et al. 1995, 1998, Jeon et al. 1997]. It involves direct contact of an elastomeric stamp against a surface in order to transfer the pattern with the

appropriate precursor “ink”. The fabrication of the stamp includes making a master with the desired topographic features and then molding a silicone elastomer stamp. The topographic features were made using conventional photolithography techniques. In this study, a master having line features of 6 to 50 μm in pitch and 1 to 1.5 μm in height (Fig. 3.10a) was provided by Whitesides’ group*. This master was placed in a Petri dish with the featured side facing up. A mixture of 10:1 by volume of polydimethylsiloxane (PDMS) Sylgard Silicone Elastomer 184 and Curing Agent 184 was made. The mixture was then agitated gently with a stainless steel stirrer and cast onto the master in the petri dish. The petri dish was placed in a vacuum for a few minutes to remove entrapped air and then cured under ambient conditions for 60 minutes and at 65 °C for another 1 hour until the polymer was completely cured. The cured PDMS was then peeled from the master and a piece of the stamp with the desired features and dimensions was cut out.

The “ink” used in μCP was a mixture 10 mM of OTS in hexane. The preparation of the “ink” and micro-contact printing were performed in a dry-box. The elastomeric stamp was soaked in the OTS solution. Then the wet stamp was dried in a stream of high purity argon for 30 seconds. The dried stamp was brought into contact with a properly prepared silicon chip and held in place for another 30 to 60 seconds. This allowed the pattern from the high regions on the stamp to be transferred to the silicon surface. The silicon chip was then placed in carbon tetrachloride and removed from the dry box. The patterned silicon chip

* The authors wish to acknowledge the generous assistance of Daniel Wolfe from Dr. Whitesides’ group at Harvard University.

was post processed following the procedure in Section 3.4.2 to remove any physisorbed OTS clusters.

In the second patterning method, a monolayer of polystyrene beads (2 μm diameter) was assembled on the silicon surface from an aqueous solution with sodium dodecylsulfate added as a surfactant*. After annealing at 90 °C, optical microscopy revealed numerous regions where the beads formed hexagonal close-packed arrays (Fig. 3.11a). These regions were marked for later observation under an AFM. The silicon chip was now ready for OTS deposition. Anhydrous OTS deposition times on these surfaces were limited to 60 second because the solvent, bicyclohexyl, slowly dissolves the polystyrene beads. The regions that were not covered by the beads were coated with OTS, while regions covered with beads were not. Post processing, following the procedure outlined above, removed all the beads and left a patterned OTS film.

3.5 DIAGNOSTICS FOR OTS MONOLAYERS

A high quality OTS self-assembled monolayer should cover a surface with a defect-free single layer, should be devoid of clusters, and should exhibit a contact angle with water that is consistent with a hydrocarbon-terminated solid-gas or solid-liquid interface. Depending on the orientation of the chains, the thickness should be equal to or less than the molecular chain length of OTS (2.6 nm).

* The author wishes to thank Dr. Hugo Celio for making the convectively assembled beads.

Once prepared, the OTS-covered surfaces were examined in the following ways: (1) measuring static contact angles with H₂O; (2) measuring surface topology using AFM in either low force (nominal 3 to 6 nN) or non-contact mode; (3) measuring film thickness ellipsometrically, calibrating with known thickness SiO₂ layers on Si(100) and estimated optical constants for OTS; (4) measuring thickness and chemical composition by XPS*; (5) assessing with ISS the atomic composition accessible to backscattering into vacuum of He⁺; and (6) measuring force profiles by IFM.

3.5.1 Contact angle measurements

The water contact angle for a smooth solid surface terminated with closely packed methyl (-CH₃) and alkyl (-CH₂-) groups is 111°-115° and 102°-103°, respectively [Ulman 1991]. The expected contact angle for OTS monolayers should be between these two values based on Equation 2.13.

The static contact angles with water were measured before and after OTS deposition (Table 3.2). The contact angle for the original surface (25°) and the piranha-treated surface (22°) reflect the expected hydrophilicity of silica. The contact angles (109°) for the OTS-covered substrates are, as expected, strongly hydrophobic. This angle falls in the range from 102° to 115° given above. While other properties depend on the hydrous or anhydrous conditions of film formation, there was no difference in the contact angle. Indicating that the OTS films were stable, there was no detectable change in contact angle with time over twelve

* The author would like to thank Dr. J. M. White and Qi Wang for conducting and analyzing the XPS/ISS experiments.

months, the longest period tested for OTS-covered substrates stored in a closed vial after analysis.

3.5.2 Surface topography by AFM

Visual inspection after depositing under hydrous conditions revealed numerous patches with different shape and size. After each step of sonication as described in Section 3.4.2, both the number and size of the patches decreased significantly. Even after the final step, there were still a few visible patches with diameters of 1 to 2 μm in an otherwise featureless clear surface. Using AFM, images were taken in contact mode at low force levels (nominally 3 nN). The visually observable patchy regions (Fig. 3.7a) are very rough and include clusters with heights of order 200 nm. For visually featureless regions of the same sample, AFM shows a small number of clusters (Fig. 3.7b) with generally 10 times smaller dimensions than those of Figure 3.7a.

For films deposited under anhydrous conditions, no patches were visually observable and contact mode AFM revealed no detectable clusters (Fig. 3.8a). The more sensitive tapping mode AFM data, as shown in Figure 3.8b, also revealed a featureless film with no evidence for clusters of any size. Based on 10 line scans, the RMS roughness was less than 0.05 nm over the ($6 \times 6 \mu\text{m}^2$) scanned area. Clearly, deposition under anhydrous conditions produced a much smoother film than deposition under hydrous conditions.

3.5.3 Ellipsometry measurements

The hydroxyl terminated oxide layer produced by treatment with piranha solution was 2.0 nm thick based on calibrated ellipsometry. This thickness is expected for a passivated Si(100) surface [Shirafuji and Tachibana 1994, Cabibil 2001, Garnier et al. 2003]. A refractive index of 1.45 was calculated for OTS using the group contribution and molar index listed in Table 2.1 based on Vogel's definition (Eqn. 2.10). The atomic weights of carbon and hydrogen were taken to be 12.011 and 1.0079, respectively. The estimated refractive index was within 3% of that of SiO_x, so for the OTS-SiO_x layer, a refractive index identical to that for SiO_x (1.5) was used. For the anhydrous deposition, ellipsometric data (Table 3.3, row 1) for the combined thickness of the oxide layer and the blanket OTS film was 4.5 ± 0.1 nm. Of this, 2.5 nm is ascribed to the OTS monolayer, nearly equal to the OTS chain length of 2.6 nm. While subject to uncertainties associated with the refractive index of OTS, this result does indicate an average OTS thickness that did not exceed one layer.

3.5.4 Patterned OTS films

In addition to patterning OTS via μ CP and convectively assembled beads, patterning of the OTS was also attempted with AFM (AutoProbe M5). AFM imaging was conducted in the contact mode with a stiff cantilever in order to plow a small area at high force with the hope of removing the deposited OTS film. Following this, another non-contact mode image was taken over a larger area that included the scratched region. If the OTS film had been successfully removed, the

difference in height between plowed and intact regions should match the OTS film thickness. However, attempts to remove OTS in this way were unsuccessful, even at the maximum load available ($\sim 1 \mu\text{N}$). As shown in Figure 3.9, the area probed was discernable in non-contact mode but line scans indicated a height difference of no more than 0.6 nm in passing from plowed to unplowed areas. This value is much less than the chain length of OTS (2.6 nm). Note that there was no accumulation of material at the edges of the plowed region, i.e., no ridges that would indicate that OTS moieties were forced by the probe tip to the edges of plowed zone. This image is consistent with a thin covalently bound OTS monolayer that can be flattened, but not moved aside by a heavily loaded AFM tip.

AFM imaging of the μCP patterned substrates was striking in that phase images (Fig. 3.10b) showed considerable contrast while topographical images (Fig. 3.10c) were almost featureless. Since the two images were taken simultaneously using two signal sources, the two images are from identical areas of the surface. The phase image can be quite sensitive to small changes in surface chemical composition that are not necessarily reflected in topography because the phase signal measures the phase lag between the periodic signal that drives the cantilever oscillations and the cantilever oscillations themselves. Interestingly, a water contact angle of 75° to 90° was measured on these patterned surfaces comprised of parallel $5 \mu\text{m}$ wide stripes alternating between OTS-covered and OTS-free regions. These values lie midway between 109° and 22° , the values measured for blanket OTS films and hydroxylated SiO_x , respectively.

AFM images of the OTS that was patterned using convectively assembled 2 μm diameter polystyrene beads exhibited much stronger contrast (Fig. 3.11). After exposure to the bicyclohexyl solution containing OTS and then removing the beads, a $15 \times 15 \mu\text{m}^2$ scan taken promptly exhibits a hexagonal close-packed pattern (Figs. 3.11b) of 0.3 μm diameter dark features separated by 2 μm . These dark regions are taken to be areas where the beads made contact with the substrate and were not accessible to OTS during film formation. Line scans of the circular features (Figs. 3.11c,d) gives a height difference of 1.7 to 2.0 nm. Notice (Fig. 3.11d) the presence of some small voids, which indicates low coverage of OTS.

The thickness of these two patterned OTS films was significantly less than the extended length of OTS and thinner than indicated by ellipsometry. Among the possible interpretations, two appear most likely: (1) a low area density of OTS resulting from the short contact time and short deposition time required to avoid dissolving the beads (3 min exposure to bicyclohexyl is sufficient to dissolve the beads) and (2) the accumulation of water in the hydrophilic regions where OTS is absent. The first could lead to significant tilting of the hydrocarbon chains away from the surface normal as the AFM tip scans the surface. Evidence for the second is shown in Figure 3.12. The AFM image (Fig. 3.12a) that was taken immediately following post processing shows holes of depth 1.7 nm. After standing in lab atmosphere 8 hours, another AFM image (Fig. 3.12b) shows that the holes have turned into bumps with height of 5 nm. An AFM image (Fig. 3.12c) taken 20 hours later shows that, except for the large bumps shown in Figure 3.12b, numerous small bumps have appeared on the OTS-covered portion

of the substrate. These probably originated from small voids as shown in Figure 3.11d. These bumps should be the accumulated water from the environment and showed the hydrophilic nature of the bare silicon and proved the low density of OTS coverage in this case.

3.5.5 XPS, ISS characterization

For a substrate prepared under anhydrous conditions, XPS and ISS measurements from a 3×3 mm² area, before and after sputtering, proved helpful in confirming the composition and the monolayer nature of the OTS films produced under anhydrous conditions. Figure 3.13 is a broad scan of the OTS-covered substrate. The peaks in this spectrum are attributable to carbon, oxygen and silicon. In the amplified region (inset), there is no evidence for Cl (BE= 198.5 ± 1 eV) indicating that the preparation reduces the Cl concentration below detection limits of XPS ($< 2\%$ of a monolayer within 3λ of surface where λ is the mean free path of a Cl photoelectron).

Figures 3.14 and 3.15 confirm that the OTS layer formed under anhydrous conditions is no more than a monolayer thick. In each figure, detailed spectra are given for four different surfaces: (A) piranha etched Si(100) surface prior to exposure to OTS, (B) surface exposed to OTS under anhydrous conditions, (C) surface from (B) exposed to 5 keV He ions for 300 s, and (D) surface from (C) exposed to 2 keV Ar ions for 120 s. Prior to dosing with OTS, a substrate that has been etched shows readily detectable signals (Fig. 3.14-A) for both oxidized and unoxidized Si, as well as for C and O. The corresponding ISS profile (Fig. 3.15-

A) exhibits clear signals for Si and O. After deposition of OTS, the XPS profiles are shown in Figure 3.14-B. Compared to the initial sample, the Si(2p) and O(1s) signals are attenuated and the C (1s) signal is much stronger.

The formation of organic monolayers on the silicon surface leads to the attenuation of the Si(2p) peak intensity in the spectrum as compared to the clean surface. The attenuation can be used to estimate the film thickness. The simple equation relating film thickness h to the Si(2p) peak intensity I is given by

$$I = I_0 e^{-h/d \cos \theta} \quad (3.1)$$

where I_0 is the Si(2p) peak intensity from the unmodified substrate, d is the attenuation length of the Si(2p) photoelectron in the hydrocarbon film, and θ is the photoelectron takeoff angle relative to the surface normal. Comparing the peak areas of the zero-valent Si(2p) signals in Figures 3.14-A and 3.14-B, and using an attenuation length of 3.4 nm [Bain et al. 1989, Major and Zhu 2001] and a takeoff angle of 30°, the film thickness was calculated to be 2.2±0.2 nm.

Using 1 kV He⁺, the ISS profile with no sputtering (Fig. 3.15-B) gives direct evidence for the presence of small amounts of Si and O. After sputtering with 5 kV and 1.2 μA He⁺ for 300 s, the ISS Si and O signals double (Fig. 3.15-C) while changes in the XPS data are, at most, barely discernable (Fig. 3.15-C). The C(1s) intensity is slightly smaller, the O(1s) unchanged, the integrated Si(2p) signal slightly larger, and the oxidized and unoxidized Si(2p) components less well-resolved. After sputtering for 120 s with 2 kV Ar⁺ ions, there are substantial changes in both ISS and XPS. Compared to sputtering with 5 kV He⁺ ions, the ISS signal for Si intensifies 5-fold, the O signal increases 2.5×, and there

is emerging evidence for a peak attributable to C atoms (Fig. 3.15-D). In XPS (Fig. 3.14-D), the C(1s) signal is lower by 40% while the O(1s) peak drops by 20%. The Si(2p) region undergoes major changes; the unoxidized (lower binding energy) intensity increases by 30% and the oxidized and unoxidized components are poorly resolved.

These XPS and ISS results are consistent with the very smooth surface found by AFM and support a single monolayer model for the blanket OTS film formed under anhydrous conditions. We conclude that, without sputtering, the surface is nearly fully covered with a monolayer of OTS but there are isolated areas where Si and O are exposed and give rise to the ISS signals. Sputtering with light atoms like He⁺ removes only a few species, mostly OTS. As a result, more Si and O atoms are present at the surface. Sputtering with heavier Ar⁺ removes more material and exposes more Si and O and increases the Si/O ratio at the surface. The ISS intensity in the E/E_0 region near 0.35 exhibits a profile that would be consistent with He⁺ scattered from C atoms (see below).

Clearly, the overlayer is much too thin to attenuate the underlying unoxidized Si peak and is consistent with a single monolayer of OTS covering the 3×3 mm² area of the surface probed by XPS. After sputtering with Ar⁺, the XPS profiles are consistent with the removal of much of the OTS, lowering the C(1s) signal, and removing some Si and O with preferential removal of O. The Ar⁺ sputtering likely fragments the OTS and drives some carbon into the Si surface. The latter would account for the inability to remove completely the C(1s) XPS

signal. Driving C into the Si lattice could form carbidic carbon with sufficient local order to give the He^+ scattering feature at $E/E_0 = 0.35$ in ISS.

Time-of-flight secondary ion mass spectrometry (TOFSIMS) data* gathered for a blanket OTS film show the presence of C_n -containing fragments up to and including $n = 18$. The fragmentation of the OTS overlayer is extensive and the results (not shown) do little more than support the presence of C_{18} -containing adsorbed species.

3.5.6 IFM nanoindentation

Comparing the nanoindentation (IFM) properties of blanket OTS films prepared in the presence and absence of water vapor (hydrous and anhydrous conditions) proved insightful, particularly in the context of the other measurements described above. Here, only the loading paths of the nanoindentation force profiles are given for the two OTS samples prepared under different conditions. The comparison mainly demonstrates the different mechanical response, which should be related to the material and its structure.

To test for mechanical uniformity, force profiles were measured at four locations separated by 15 to 20 μm on OTS films formed under anhydrous and hydrous conditions. Profiles for the former (Fig. 3.16a) overlap within the resolution of the IFM, confirming the homogeneity of the mechanical properties probed by the IFM tip. In the compressive region between 1 and 2 nm, a linear approximation gives a slope of $1.8 \mu\text{N nm}^{-1}$. Laterally, the tip samples at most

* The author would like to thank Dr. Joo-Woon Lee for conducting the TOFSIMS experiment.

20 nm diameter regions, so there may be heterogeneities on smaller but not larger length scales. The situation is very different for a film formed in the presence of water vapor (Fig. 3.16b). In this case, the tip samples at most 30 nm diameter regions. Even with the larger sampling area, there are very clear lateral heterogeneities on the IFM probing diameter scale. In the compressive region, no two curves overlap and the initial slopes differ by a factor of 2 and lie in the range 1.5 to 3 $\mu\text{N nm}^{-1}$.

3.5.7 Summary and discussion

The quality of the SAM is sensitive to the deposition conditions, such as the amount of water, the temperature, not surprisingly, the substrate, particular its initial surface condition. Controlling and manipulating these independent variables has not been uniformly realized. Intuitively, the properties of the SAM should depend on both covalent bonding to the substrate and the cross-linking among ATS molecules. For example, the commonly used deposition [Saigiv 1980, Maoz and Saigiv 1984, Angst and Simmons 1991, Britcher and Kehoem 1993, Kessel et al. 1991, Kessel and Granick 1991, Ulman 1991, 1996] involves the addition of water to the deposition solution and monolayers produced in this way exhibit somewhat variable properties [Nakagawa and Ogawa 1994, Silberzan et al. 1991, Tripp and Hair 1992, Angst and Simmons 1991, Maboudian 2002]. The chemistry involves hydrolysis of the chlorosilanes in solution to form silanols and HCl. Cross-linking to form oligomers can occur both on the surface and in solution with elimination of water. The latter is undesirable because it leads

to clusters of various sizes and shapes that subsequently attach to the surface. Oligomerization on the surface may also lead to non-uniformities because cross-linking impacts steric constraints in forming uniformly packed, and covalently bonded OTS monolayers on silicon oxide.

Based on the above study, two structures of self-assembled OTS layer are proposed as shown in Figure 3.17 for hydrous and anhydrous processes, respectively. The hydrous process leads to the formation of clusters (Fig. 3.17a). This study underscores conditions that lead to reproducibly uniform, robust, cluster-free self-assembled monolayer films of OTS on Si(100). By oxidizing and hydroxylating the Si(100) surface and then, in an anhydrous environment, exposing this surface to an anhydrous solution of OTS, a topologically smooth, cluster-free and stable surface (Fig. 3.17b) is formed as revealed in AFM images with nanoscale resolution. As schematically indicated in Figure 3.6a, the process proposed involves selective reaction of OTS with surface hydroxyl groups to eliminate HCl and form a single covalent Si-O-Si bond at the surface. Since there was no evidence for Cl in XPS, the remaining Si-Cl bonds are presumed to be removed by reaction with atmospheric H₂O when the sample is removed from the storage vial and exposed to water vapor in the atmosphere (Fig. 3.6b).

Confirming the monolayer character of the films prepared under anhydrous conditions, the XPS and ellipsometry data are both consistent with an average thickness of 2.2 to 2.5 nm compared to the 2.6 nm extended length of OTS. Since both tools average over macroscopic dimensions, this data would indicate that for a uniform layer the hydrocarbon chains are tilted away from the

surface normal by an angle ($\sim 30^\circ$ to 16°). When combined with the ISS data exhibiting weak Si and O signals, this suggests an ensemble average OTS coverage slightly less than a full monolayer with the hydrocarbon chains nearly perpendicular to the substrate over 10 mm^2 areas. Future exploration, by combining XPS and ISS measurements with *in-situ* thermal annealing, would be valuable in assessing the structure and thermal stability of these OTS-derived monolayers [Wang et al. 2002]. The robust character of these self-assembled layers is demonstrated by our inability to remove the material by applying relatively large forces ($1 \text{ }\mu\text{N}$) while plowing with the AFM tip (Fig. 3.9) and by the twelve-month stability of samples stored in closed vials filled with ambient air. We conclude that covalent bonding to the substrate without cross-linking is sufficient to form a mechanically robust film.

In contrast to monolayers prepared under strict anhydrous conditions, when the hydroxylated Si(100) surface was exposed to OTS in the presence of moisture, the surfaces were non-uniform and there were regions inhabited by clusters that were not removed by sonication. The clusters are attributed to oligomers derived from OTS and formed in solution or at the surface by cross-linking dehydration reactions occurring after hydrolysis of OTS. These surfaces have non-uniform nanoscale elastic mechanical properties, which is undesirable. In this context, it is noteworthy that contact angle measurements, while useful, do not probe the nanoscale topology and structure of these self-assembled layers.

Our results, in agreement with the molecular modeling study of Stevens [1999], indicate that avoiding cross-linking is central to the formation of a

mechanically and topologically uniform OTS monolayer. Cross-polymerization issues are central to the differences between hydrous and anhydrous processing. Previous studies indicated that, in the presence of moisture, OTS films of poor quality were formed due to the competition between the reactions of cross-polymerization and covalent anchoring of molecules to hydroxylated surfaces. Cross-polymerized OTS films have been deposited on mica where there are few or no covalent bonds [Kessel and Granick 1991, Nakagawa et al. 1994, Parikh et al. 1995]. In some cases, both cross-polymerization and covalent anchoring occurred and the thickness of the films was not uniform [Kessel and Granick 1991, Parikh et al. 1995]. In other cases, the films could easily be removed using AFM scratching at low force levels [Nakagawa et al. 1994]. When relatively large amounts of water (glove box, 1-10% RH) were present, clusters of OTS were observed that were attached to the substrate but could mostly be removed with a chloroform tissue wipe after sonication [Vajapeyajula 2002, Winter 2002]. In the current study, after sonication, large and small clusters were observed on samples that had been prepared under hydrous conditions.

Turning to the initial condition of the substrate, it is noteworthy that incomplete monolayers have been reported as a result of anhydrous processing [Wasserman et al. 1989, Le Grange et al. 1993]. Since steps were taken to eliminate the hydroxyl groups on the surfaces, the surface density of hydroxyl groups was low. In the present study, the opposite approach was taken and a piranha solution was used to ensure that the density of the hydroxyl groups was very high.

Our results demonstrate directly that, as expected, exquisite control of chemical events has an important impact on the mechanical properties of self-assembled OTS-derived monolayers. Not surprisingly, maximizing initial surface hydroxylation and using anhydrous environments are both important. The mechanical properties of the films formed under anhydrous conditions exhibit reproducible force versus distance profiles in the elastic deformation regime while the profiles for films formed in the presence of some moisture vary significantly from region to region of the same film. We assert that much of the lab-to-lab variation in OTS film properties is the result of inadequately controlling both moisture and surface hydroxylation.

CHAPTER FOUR

ANALYSIS

4.1 INTRODUCTION

Figure 4.1 shows a schematic of IFM experiments with γ -APS films and self-assembled OTS monolayers on silicon. Notice that, for both cases, there were two layers of films on Si(100): the top layer of γ -APS or OTS and the SiO₂ under layer. For bi-layered thin films on a substrate (Fig. 4.1) in the absence of adhesive interactions, the force-separation response depends on the following parameters

$$P = K\sqrt{R}\delta^{3/2} \cdot F\left(\frac{E_i}{E_s}, \frac{E_{f_1}}{E_s}, \frac{E_{f_2}}{E_s}, \nu_i, \nu_{f_1}, \nu_{f_2}, \nu_s, \frac{\delta}{t_{f_1}}, \frac{R}{t_{f_1}}, \frac{t_{f_2}}{t_{f_1}}\right), \quad (4.1)$$

where the subscripts i, f, s represent indenter, films and substrate, respectively; E and ν are Young's modulus and Poisson's ratio; $\frac{1}{K} = \frac{3}{4} \left(\frac{1-\nu_i^2}{E_i} + \frac{1-\nu_{f_1}^2}{E_{f_1}} \right)$ and t and

R are the film thickness and tip radius. Subscripts 1 & 2 refer to the top and under layers, respectively. In general, the dimensionless function F could be complicated because there are so many parameters. It is noted that when the sample is monolithic, $F = 1$ and the force profile becomes the Hertzian one. It is expected that, when the adhesive interactions are considered, the function F will become even more complicated.

In this chapter, the techniques for analyzing nanoindentation experiments are described in detail. The classic contact mechanics theories are reviewed first. The methods of extracting mechanical properties from the indentation experiments using contact mechanics theories are discussed. A finite element model, which accounted for the layer and substrate interactions and adhesive interaction using a cohesive zone modeling approach, is developed. The application of a molecular dynamics simulation of the compression of an OTS monolayer on silica by tungsten plate is described. Finally, a hypo-elastic constitutive model for the representation of the non-linear elastic response of the OTS by molecular dynamics simulation is established.

4.2 CONTACT MECHANICS

In this section, the contact mechanics theories, which account for the contact between two monolithic deformable bodies, are reviewed. These theories include Hertz, JKR, DMT and Maugis theories. The differences between them are due to the different types of adhesives interactions that were invoked in the analyses. Some commonly used formulas that account for plastic deformation are also given. These derivations are based mainly on Hertz theory. Their application to and limitations for analyzing the indentation of layered materials are discussed.

4.2.1 Contact mechanics theories

Figure 4.2 shows a schematic of contact between two deformable spheres. The typical force separation response for elastic contact is shown as Figure 4.3. Noting that there are two paths — loading and unloading, and two regions — compressive and adhesive. If the contact is purely elastic, most of the loading and unloading parts overlap each other in the compressive region. However, there could be hysteresis in the adhesive region that might have some chemical origins.

Contact mechanics theories can be used to analyze the elastic contact. They usually can represent part of the force profile, depending on the theory. Hertz solved the contact problem between two spherical elastic bodies in 1888 by assuming a hemispherical pressure inside the contact area. This classic contact mechanics solution does not include surface forces. Johnson et al. [1971] provided the Johnson Kendall Roberts (JKR) theory, which included surface interactions inside the contact area. As a result, the contact area predicted by JKR theory is larger than the Hertz solution. In 1975, Dejaguin et al. presented a different theory, the Derjaguin Muller Toporov (DMT) theory, which includes the surface interactions outside the contact area while maintaining the Hertzian profile. Maugis [1992] treated the contact between two spherical bodies as a fracture problem and derived more complex and complete formulas by incorporating Sneddon's solution with a Dugdale cohesive zone model. This solution bridges the JKR and the DMT theories.

The Hertz solution for the force P in terms of the contact radius a is

$$P = \frac{Ka^3}{R}; \quad (4.2)$$

where R is the reduced radius $\frac{1}{R} = \frac{1}{R_i} + \frac{1}{R_f}$ and K is a parameter defined by

$$\frac{1}{K} = \frac{3}{4} \left(\frac{1-\nu_i^2}{E_i} + \frac{1-\nu_f^2}{E_f} \right). \quad \text{The subscript } i \text{ indicates the indenter, and } f \text{ the film. In}$$

this paper, the subscript f will always refer to the film whether the sample is being considered to be multilayered or a monolithic body. The indentation depth, δ , is given by

$$\delta = \frac{a^2}{R}. \quad (4.3)$$

Combining (4.2) and (4.3) yields the relationship between force vs. indentation depth

$$P = KR^{1/2}\delta^{3/2} \quad (4.4)$$

No surface forces were considered in this elasticity solution. The Hertz theory can only be applied to the problems where attractive forces are much lower than the applied compressive force.

The JKR theory modifies the Hertzian theory by including the effects of the surface energy ω , so that

$$P = \frac{Ka^3}{R} - \sqrt{6\pi\omega Ka^3} \quad (4.5)$$

and

$$\delta = \frac{a^2}{R} - \sqrt{\frac{8\pi a\omega}{3K}}. \quad (4.6)$$

The maximum adhesion force (pull-off force) can be determined, by taking

$$\frac{dP}{d\delta} = 0 \quad \left(\frac{dP}{da} = 0 \right), \text{ as}$$

$$P_c = \frac{3}{2}\pi\omega R \quad (4.7)$$

The monotonic part of the JKR force profile from maximum adhesion force $-P_c$ to maximum compressive force can be written in one equation by reorganizing equations (4.5) to (4.7) as

$$\delta = \sqrt[3]{\frac{P_c^2}{K^2 R}} \cdot \left[\sqrt[3]{f^2\left(\frac{P}{P_c}\right)} - \frac{4}{3} \sqrt[6]{f\left(\frac{P}{P_c}\right)} \right], \quad (4.8)$$

where

$$f(x) = x + 2(1 + 2\sqrt{1+x}). \quad (4.9)$$

In JKR theory, it is assumed that there is no interaction between the surfaces when they are not in contact, which accounts for short-range surface forces acting only inside the contact area. Even so, the gap profile is no longer Hertzian. The JKR theory is applicable to systems where at least one solid is soft or has a high surface energy.

On the other hand, the DMT theory includes long-range surface forces acting outside the contact area. As a result, it can be applied to hard systems with low surface energy. By assumption, the gap profile is still Hertzian so that there is no stress singularity at the edge of the contact zone. The expressions for the force and the indentation depth become

$$P = \frac{Ka^3}{R} - 2\pi\omega R \quad (4.10)$$

and

$$\delta = \frac{a^2}{R}. \quad (4.11)$$

The force vs. separation relationship is then

$$P = KR^{1/2}\delta^{3/2} - P_c, \quad (4.12)$$

where

$$P_c = 2\pi\omega R \quad (4.13)$$

is the pull-off force.

Maugis used the Dugdale cohesive zone model, where the adhesive interaction is represented by a constant traction-separation law over an annular region around the contact area ($a \leq r \leq c$, Fig. 4.2), to cancel the stress singularity at the edge of the contact zone and derived the following more general equations.

$$\bar{P} = \bar{a}^3 - \lambda \bar{a}^2 \left(\sqrt{m^2 - 1} + m^2 \tan^{-1} \sqrt{m^2 - 1} \right), \quad (4.14)$$

$$\bar{\delta} = \bar{a}^2 - \frac{4}{3} \bar{a} \lambda \sqrt{m^2 - 1}, \quad (4.15)$$

$$\begin{aligned} & \frac{\lambda \bar{a}^2}{2} \left[\sqrt{m^2 - 1} + (m^2 - 2) \tan^{-1} \sqrt{m^2 - 1} \right] \\ & + \frac{4\lambda^2 \bar{a}}{3} \left[\left(\sqrt{m^2 - 1} \tan^{-1} \sqrt{m^2 - 1} \right) - m + 1 \right] = 1 \end{aligned} \quad ; \quad (4.16)$$

where $m = \frac{c}{a}$, c is the cohesive zone size plus the contact radius and $m \geq 1$. The

quantities \bar{a} , \bar{P} , and $\bar{\delta}$ are the contact radius, force, and depth, respectively, normalized as follows:

$$\bar{a} = \frac{a}{(\pi\omega R^2 / K)^{1/3}} \quad \bar{P} = \frac{P}{\pi\omega R} \quad \bar{\delta} = \frac{\delta}{(\pi^2 \omega^2 R / K^2)^{1/3}} \quad (4.17)$$

The parameter λ involves the stiffness of the contacting materials and their surface interactions.

$$\lambda = \frac{2\sigma_0}{(\pi\omega K^2 / R)^{1/3}}. \quad (4.18)$$

The quantity σ_0 is the constant stress acting in the cohesive zone. When $\lambda \rightarrow 0$, the Maugis equations correspond to the DMT theory, whereas $\lambda \rightarrow \mathbb{N}$ yields the JKR result.

Figure 4.4 is a comparison of the force profiles from Hertzian, DMT and JKR theories. The force profiles of Maugis solution should fall in between the JKR and DMT theories. There is no adhesive force region in Hertzian theory. The pull-off force varies from $\frac{3}{2}\pi\omega R$ to $2\pi\omega R$ with JKR and DMT theories as two bounds for the rest value of λ in Maugis theory. Hertzian mechanics can only be applied to interpret the experiments where the compressive forces are high and the adhesive forces are negligible. In general, the Maugis solution should be used. The JKR and DMT theories act as two limits from compliant systems with strong adhesive interactions to hard systems with low adhesion.

All these theories can be used to analyze nanoindentation experiments and extract mechanical and adhesive properties. However, none of them explain the hysteresis shown in Figure 4.3. With Hertzian theory, only the mechanical properties can be extracted. The DMT, JKR and Maugis theories can be used to extract both mechanical and adhesive properties from nanoindentation experiments.

4.2.2 Elastic-plastic contact

Several formulae [Doener and Nix 1986, Oliver and Pharr 1992, Field and Swain 1993] for extracting the mechanical properties have been derived for the cases where the force levels are so high that plastic deformation occurs in the loading path. These formulae are all based on the Hertz theory and assume that there is no reverse plasticity in the unloading path. Oliver and Pharr [1992] derived an expression for extracting the elastic modulus from indentation

experiments based on Sneddon's [1965] elasticity solution. The reduced elastic modulus $E^* = \frac{E}{1-\nu^2}$ is extracted by computing the initial tangent of the elastic unloading path at $P = P_{\max}$ (Fig. 4.5) using

$$E^* = \frac{\sqrt{\pi}}{2\sqrt{A}} \left. \frac{dP}{d\delta} \right|_{P_{\max}} \quad (4.19)$$

where A is the contact area (πa^2 for spherical indenters).

Similarly, Field and Swain [1993] used part of the elastic unloading path rather than the initial unloading tangent at maximum load (Fig. 4.5) to extract the reduced elastic modulus. Their analysis was based on Hertz theory and the formulae are

$$E^* = \frac{3}{4} \frac{P}{a\delta_e}, \quad (4.20)$$

where $\delta_e = \delta_t - \delta_r$ is the elastic indentation depth and a is the contact radius. The values of δ_r and contact radius a are determined using

$$\delta_r = \frac{\delta_s (P_{\max} / P_s)^{3/2} - h_t}{(P_{\max} / P_s)^{3/2} - 1} \quad (4.21)$$

and

$$a = \sqrt{2R\delta_p - \delta_p^2}, \quad (4.22)$$

where $\delta_p = \frac{\delta_t + \delta_r}{2}$.

It should be noted that both the Oliver and Pharr [1992] and Field and Swain [1993] methods are based on the Hertz theory for elastic contact and no adhesive interactions are included. Even though Oliver and Pharr's method looks simple and can be used for indenters with any shape, the determination of the

actual contact area is not a trivial task and requires some other tests and techniques.

4.2.3 Contact of layered materials

It should be noted that the theories described above should only be used for monolithic materials or sufficiently thick films on a substrate. Care must be taken when interpreting the indentation data of thin layered materials using the above theories due to the layer and substrate interaction. A commonly used rule for neglecting the substrate effect is to restrict the indentation depth to be less than 10% of the film thickness [Bückle 1971, Fischer-Cripps 2000, Cabibil et al. 2001]. In some cases where the substrate effect is unavoidable, some empirical formulae for extrapolating the reduced elastic modulus of film are given [for a summary see Menčík et al. 1997]. In these methods, a series of indentation experiments are performed to various depths and the composite (film and substrate) elastic modulus are extracted using Equation 4.19. By fitting the composite modulus to the following equation

$$E^* = E_f^* + (E_s^* - E_f^*)\Psi(x) \quad (4.23)$$

where E^* is the composite modulus, $\Psi(x)$ is a weight function of the relative penetration $x = a/t$ or δ/t . Here t is the thickness of the top layer whose elastic modulus is then extrapolated at $x = 0$.

There are also some elasticity solutions [Gao et al. 1992, Yu et al. 1990, Kim 1996, Yoffe 1998] for indentation on layered materials that account for layer and substrate interaction. They are either for special cases or a combination of

analytical and numerical analysis. None of these derivations considered adhesive interactions. Due to their limitation and complexity, these derivations are not suitable for analyzing general indentation experiments. Consequently, accurate and general analysis of indentation experiments has to be in the form numerical analysis. Such methods can account for the substrate effect, Poisson effect and adhesive interactions, thereby providing flexibility and versatility.

4.3 FINITE ELEMENT ANALYSIS

Numerical methods provide a suitable technique for analyzing nanoindentation experiments when multiple layers are present.

Finite element analysis was performed with the commercial finite element software package ABAQUS*, which is capable of modeling the contact between either two deformable bodies or one rigid body and another deformable body. ABAQUS defines contact between two bodies in terms of a contact pair with two surfaces: the master surface, and the slave surface. The geometry of the IFM experiments on the layered samples (γ -APS on silicon and OTS monolayer on silicon) is shown in Figure 4.1. The thicknesses of γ -APS films were given in Table 3.1 and the OTS monolayer was 2.5 nm thick. The thickness of the silica (SiO_2) layer was 2.0 nm and the silicon substrate was taken to be a half-space in all analyses. Due to the presence of the spherical indenter and the relatively low forces used in the experiments, the problem was treated as being axisymmetric with surface interactions. Linearly elastic and isotropic materials were used for

* The authors would like to thank Hibbitt, Karlsson & Sorensen, Inc. for the use of ABAQUS under academic license.

the spherical tungsten probe, SiO₂ layer and silicon substrate (Table 4.1). The mechanical properties of the top film (γ -APS or OTS monolayer) were varied so as to fit the experiments. Geometrically nonlinear analysis was used throughout the simulations due to the large deformations in contact problems.

Quadrilateral (four-node) first-order (linear) interpolation axisymmetric elements with reduced integration were used for both the indenter and specimen. In some cases, the full integration elements had to be used on the contact surfaces in order to avoid the pseudo deformation modes that were caused by the reduced integration. Figure 4.6a shows the overall mesh for the problem along with a magnified view (Fig. 4.6b) of the mesh close to contact surfaces. The meshes were biased towards the contact surfaces, where the largest deformation is expected. In order to simulate the contact area accurately, very fine meshes were used over the potential contact surfaces. Infinite elements were used for the far-field region (>20 times the maximum contact radius) of the half space so that no boundary conditions needed to be enforced on the unbounded domain. The parametric feature of ABAQUS was employed so as to adjust the mesh for each computation. A suitable level of mesh refinement was established on the basis of the Hertz solution.

The geometry of contact with surface interactions is shown in Figure 4.7a (cohesive zone model). The default contact pressure-clearance relationship used by ABAQUS is referred to as the “hard” contact model (Fig. 4.7b). It only transmits pressure once the surfaces come into contact. This interaction model is not sufficient for analyzing indentation experiments where the adhesive effect is

large. As a result, user-defined interface elements were incorporated with the abovementioned mesh. The purpose of introducing the user-defined elements was to modify the surface interaction model so as to include any kind of adhesive interaction between the two surfaces. The user element code (UEL subroutine) was programmed in Fortran language and added to the ABAQUS input file. Figure 4.7c shows a user-defined triangular adhesion interaction that was used as the force-separation law throughout the study when adhesive interactions were considered. There are three parameters that define it: the maximum adhesive traction σ_0 , the corresponding displacement δ_0 and the cut-off displacement δ_t . The surface energy can be expressed as the area underneath the traction-separation curve, i.e.,

$$\omega = \frac{\sigma_0 \times \delta_t}{2}. \quad (4.24)$$

Adjusting these three parameters as well as the mechanical properties of the top film allowed the optimum fit to measured force profiles to be achieved.

4.4 MOLECULAR DYNAMICS

Molecular dynamics was used to simulate a self-assembled OTS monolayer on a SiO₂ substrate and the compression of the monolayer by a tungsten plate. The simulation was performed with the molecular dynamics simulation package DL_POLY package 2.0*. Integration was based on the simple Verlet leapfrog scheme. It generates trajectories in an ensemble in which the total

* DL_POLY 2.0 package was developed at Daresbury Laboratory, U.K. and is available free, under license, to academic institutions on a worldwide basis [Smith and Forester 1996].

energy $H_{NVE} = U + KE$ (kinetic plus potential energy) is conserved. Simulation was carried out in the NVT ensemble, which has a fixed number of particles and constant total volume and temperature, using a Hoover-Nose thermostat. Room temperature (298.15 K) was maintained during the calculation. To make the simulation simple, the top layer of the SiO₂ substrate and the tungsten plate were modeled as rigid surfaces with one layer of atoms. The hexagonal arrangement of the SiO₂ surface was modeled as described by Stevens [1999] who accounted for surface corrugation (Fig. 3.5a,b). The body-centered cubic structure of tungsten crystals was modeled as a flat atomic surface in the (100) direction. Both the SiO₂ and tungsten were treated as rigid because they were expected to be much stiffer than the OTS monolayer. All elements were represented in atomic detail. The OTS molecular chains were modeled using united atoms (pseudo-atoms), where the CH₃ and CH₂ groups were represented as single effective pseudo-atoms. Slab periodic boundary conditions, which were periodic in the *x*- and *y*-directions, were used to represent the infinite extent in the two in-plane directions. The repeating cell had lateral dimensions of 26×27 Å² containing 30 OTS molecules. Figure 4.8 shows the molecular dynamics simulation cell for OTS on silica. All the OTS molecular chains were initially arranged perpendicular to the SiO₂ surface.

Atomic molecular modeling via empirical potential functions is highly developed [Allen and Tildesley 2002, Frenkel and Smit 2002]. The forces are defined by a set of empirical potential functions with forms having a basis in chemical physics, and these are parameterized to give reasonable energy and force levels. For organic molecules, there are two classes of forces: intra-molecular and

inter-molecular interactions [Smith and Forester 2001]. In this study, harmonic bond, harmonic valence angle and cosine dihedral angle potentials were used for intra-molecular interactions. These potentials describe the explicit force between atoms due to chemical bonds, the bond bending and the interaction arising from torsion forces in molecules, respectively. The total configuration energy of the molecular system was the sum of all the above interaction potentials and could be written as

$$\begin{aligned}
 U(r_1, r_2, \dots, r_N) = & \sum_{i_{bond}=1}^{N_{bond}} U_{bond}(i_{bond}, r_a, r_b) \\
 & + \sum_{i_{angle}=1}^{N_{angle}} U_{angle}(i_{angle}, r_a, r_b, r_c) \\
 & + \sum_{i_{dihed}=1}^{N_{dihed}} U_{dihed}(i_{dihed}, r_a, r_b, r_c, r_d) \\
 & + \sum_{i=1}^{N-1} \sum_{j>i}^N U_{pair}(i, j, |r_i - r_j|)
 \end{aligned} \tag{4.25}$$

The intra-molecular interactions were specified for all bonds, valence angles and dihedrals. The potentials were:

1) Harmonic bond potential

$$U(r_{ij}) = \frac{1}{2} k (r_{ij} - r_0)^2, \tag{4.26}$$

2) Harmonic valence angle potential

$$U(\theta_{jik}) = \frac{k}{2} (\theta_{jik} - \theta_0)^2 \tag{4.27}$$

and

3) Cosine dihedral angle potential

$$U(\phi) = \frac{A_1}{2} (1 + \cos \phi) + \frac{A_2}{2} (1 - \cos 2\phi) + \frac{A_3}{2} (1 - \cos 3\phi). \tag{4.28}$$

All the inter-molecular interactions were modeled with (12-6) Lennard-Jones van der Waals potentials. The force-cutoff distance was set to 10 Å. No

coulomb forces were considered. The inter-molecular interactions were specified by atom types and were represented by the short range (van der Waals) pair-body Lennard-Jones potential as

$$U(r_{ij}) = 4\varepsilon \left[\left(\frac{\sigma}{r_{ij}} \right)^{12} - \left(\frac{\sigma}{r_{ij}} \right)^6 \right]. \quad (4.29)$$

The specific values that were used for the various interactions are listed in Tables 4.2 to 4.6. During the simulation, the trajectory of each atom was followed. Macroscopic quantities were averaged on the statistical basis of the configuration history. In particular, the stress tensor was averaged over the volume through

$$\langle \underline{\sigma} \rangle = \frac{1}{V} \sum_k \underline{f}^k \otimes \underline{r}^k \quad (4.30)$$

with

$$\underline{f} = \left[\frac{\partial U(r)}{\partial r} \right] \begin{pmatrix} \underline{r} \\ r \end{pmatrix}, \quad (4.31)$$

where $r = |\underline{r}|$, and V is the volume of the current configuration.

4.5 HYPO-ELASTIC BEHAVIOR

The results of both linear finite element and molecular dynamics analyses, which will be given in Chapter 5, indicated that the mechanical behavior of OTS monolayer was highly non-linear. Due to its simplicity, hypo-elastic behavior was chosen to represent the non-linear elastic response of OTS that was obtained from molecular dynamics simulations. In a hypo-elastic material, the rate of change of

stress is defined through a tangent modulus matrix multiplying the rate of the change of the elastic strain [ABAQUS]

$$d\sigma = \underline{D} \circ d\varepsilon, \quad (4.32)$$

where $d\sigma$ is the rate of change of the stress, \underline{D} is the tangent elasticity matrix, and $d\varepsilon$ is the rate of change of the elastic strain.

The entries in \underline{D} are calculated from the tangent modulus, E_t , and Poisson's ratio, ν_t , as functions of the strain invariants, which are defined here as

$$\begin{aligned} I_1 &= \text{trace}(\varepsilon), \\ I_2 &= \frac{1}{2}(\varepsilon \circ \varepsilon - I_1^2), \\ I_3 &= \det(\varepsilon). \end{aligned} \quad (4.33)$$

In this study, the ABAQUS user material subroutine UHYPEL was programmed in Fortran language and incorporated in the ABAQUS input file. Both E_t and ν_t were derived from directly molecular dynamics solution as functions of the strain invariants, as will be described in Chapter 5.

CHAPTER FIVE

RESULTS AND DISCUSSION

5.1 INTRODUCTION

The results of the IFM experiments on γ -APS films and OTS monolayers are presented and analyzed in this chapter. The layer and substrate interactions were investigated first using a finite element parametric study. A one-layer film on a substrate was used and no adhesive interactions were considered at this stage. These analyses provided useful guidelines for the subsequent analyses of the IFM experiments. A suitable array of continuum mechanics analyses for the IFM experiment was developed based on the analysis of the γ -APS films. Some of these developments were useful for analyzing the experiments with OTS monolayers.

5.2 PARAMETRIC STUDY OF LAYER AND SUBSTRATE INTERACTIONS

The purpose of the nanoindentation experiments is to determine the elastic properties (E_f, ν_f) of the top film as shown in Figure 4.1. As we consider thin layers of γ -APS and monolayers of OTS, we expect layer and substrate interactions to play an important role. Because of this focus, no adhesive interactions were considered at this stage. In this section, a parametric analysis of these interactions was conducted with ABAQUS.

For a single layer film on a substrate, Equation 4.1 simplifies to

$$P = K\sqrt{R}\delta^{3/2} \cdot F\left(\frac{E_i}{E_s}, \frac{E_f}{E_s}, \nu_i, \nu_f, \nu_s, \frac{\delta}{t}, \frac{R}{t}\right). \quad (5.1)$$

Note that the subscript f replaces f_l and t is used for the film thickness in Equation 4.1. The effects of the different combinations of materials properties and geometry in Equation 5.1, such as modulus, Poisson's ratio and probe size to film thickness, were studied.

5.2.1 Parametric study of substrate effects

The elastic modulus is often extracted from nanoindentation experiments using either Hertzian analysis [Cabibil et al. 2001] or Oliver and Pharr's method [1992]. When these methods are applied to thin films on a substrate, the effect of the substrate needs to be considered [Doerner and Nix 1986, Menčík et al. 1997, Sawa et al. 1999, Fischer-Cripps 2001]. Finite element methods have been used to analyze hardness measurements and extract elastic properties from indentation with pyramidal and spherical indenters [Sawa et al. 1999, Swadener et al. 2002]. In this study, a finite element analysis was used to examine the influence of the substrate on nanoindentation measurements when a spherical indenter is used (Eqn. 5.1). The film thickness was fixed at 50 nm. In order to examine the substrate effect on the measurement of film modulus, the substrate was taken to be a half-space with a fixed Young's modulus $E_s=100$ GPa and both the films and substrate were given Poisson's ratios $\nu=0.2$. The radius of the spherical indenter was chosen to be 2, 10 and 100 times of the film thickness.

Figure 5.1 shows the force profiles for various film moduli and probe radii. The force was normalized by the Hertzian value at a given depth (Eqn. 4.4) using the material properties of the film. The analysis covered a large range of ratios of film and substrate moduli, with special emphasis on soft films on stiff substrates. The results indicate that the force profile became less sensitive to situations where the film and substrate moduli are closer. Since both Doerner and Nix [1986], and Oliver and Pharr's [1992] methods are based on elastic solutions, these results should correspond to the relationship between the measured composite modulus vs. indentation depth. Experimental evidence of similar trends has also been reported [Sawa et al. 1999, Saha and Nix 2002]. The striking result here is that the 10% rule on indentation depth does not hold. The Hertzian load overestimation for soft films on hard substrates or underestimation for hard films on soft substrates is significant even when the indentation depth is less than one-tenth of the film thickness.

This departure from Hertz theory was also sensitive to probe relative size (Figs. 5.1a,b,c). As the probe size increased, the over- and underestimation become more and more severe. Figure 5.2 shows the contact radius vs. the indentation depth for different probe sizes. The contact radius was also normalized by the Hertzian value. It can be seen that the actual contact radius was larger or less than that of the Hertzian value depending on the stiffness of the film relative to the substrate. Figure 5.3 shows the relationship between the same normalized forces and the resulting contact radii. The variation of normalized force was almost linear with contact radius for all cases where the slopes

depended on the modulus ratios. Surprisingly, the variation in normalized force was almost the same for all probe sizes (Figs. 5.3a,b,c). This result is distinguished from Figure 5.1 where the force was plotted against indentation depth and varied with probe size. It can therefore be concluded that it was the differences between the actual contact radius and the Hertzian one that caused the force profiles to depart from Hertzian theory.

5.2.2 Parametric study of Poisson effects

For monolithic bodies or very small contact radii as shown in Section 5.2.1, the modulus and Poisson's ratio of a film can be lumped into the reduced elastic modulus $E^* = \frac{E}{1-\nu^2}$. Otherwise, there will be interactions between the layers that depend on the relative thickness of the layers and their elastic properties. The dimensional analysis given in Equations 4.1 and 5.1 suggests that the use of reduced moduli for each layer is unlikely to be successful. As a result, the Poisson effect on the force profiles was considered.

Although Poisson's ratio is widely believed to have a relatively small effect on the reduced modulus, it can affect the stress state significantly when layered materials are subjected to compression or tension in the thickness direction. As a result, it is expected that, as films become thinner or the indentation depth is larger, the difference in force profiles due to different Poisson's ratios, even with the same reduced modulus, will be large. Dundurs [1969] showed that two dimensionless parameters formed from the combination of the elastic constants of two isotropic, layered materials are sufficient to

describe the elastic mismatch in plane problems. The two Dundurs' parameters are

$$\alpha = \frac{\mu_1(\kappa_2 + 1) - \mu_2(\kappa_1 + 1)}{\mu_1(\kappa_2 + 1) + \mu_2(\kappa_1 + 1)} \quad (5.2)$$

and

$$\beta = \frac{\mu_1(\kappa_2 - 1) - \mu_2(\kappa_1 - 1)}{\mu_1(\kappa_2 + 1) + \mu_2(\kappa_1 + 1)}, \quad (5.3)$$

where μ is the shear modulus, $\kappa = 3 - 4\nu$ for plain strain and $\kappa = \frac{3 - \nu}{1 + \nu}$ for plain stress, and ν is Poisson's ratio. In general, α is a measure of the mismatch of the reduced modulus and β is a measure of the mismatch of the bulk modulus. Both α and β vanish when there is no mismatch. The quantity α varies from -1 to 1 corresponding to a soft material on a rigid substrate and *vice versa*.

The effect of Poisson's ratio on the indentation force profiles for a single layer (50 nm thick) on a substrate was investigated by considering various combinations of the properties of the film and substrate (still a half-space). Figures 5.4, 5.5 and 5.6 show the results from finite element simulations for different ratios of probe radius to film thickness of 5, 10 and 100, respectively. Each of the figures presents the results for three values of α (-0.9 , 0 , and 0.9), which covers the variation from very soft films on stiff substrates to very stiff films on soft substrates. In each case, α was held constant, which means the reduced modulus of the film did not change, while the Poisson's ratio of the film did. The force was normalized by the case when the film and substrate had the same Poisson's ratio. The displacement was normalized by the film thickness.

The study showed that, when the film has a larger Poisson's ratio than that of substrate, $\bar{P} > 1.0$, and *vice versa*. However, the effect on the force profiles was relatively small when the Poisson's ratio of the film was less than that of the substrate ($\bar{P} \lesssim 1.0$). When $\alpha > 0$, which corresponds to the case of a stiff film on a compliant substrate, the effect (Figs. 5.4b,c, 5.5b,c, 5.6b,c) on the force profiles was always small. The variation in force profiles was larger when the Poisson's ratio of the film was larger than that of the substrate. The most severe case is for $\alpha \rightarrow -1$ (Figs. 5.4a, 5.5a, 5.6a), which corresponds to situations when the films are much softer than the substrate. The variation that was caused by different Poisson's ratios can be attributed to the lateral constraint caused by the interface mismatch between the film and the substrate. These results indicated that Poisson's ratio had a significant effect on indentation force profiles of layered materials, especially when the film is much softer than substrate. As a result, the modulus and Poisson's ratio cannot be grouped into the reduced modulus. Accurate determinations of both are equally important in indentation and therefore a separate experiment is required [Lucas et al. 2004].

Figure 5.7 shows the same normalized force but this time plotted against normalized contact radius. It follows the same variation as described in Figure 5.3 except that here the variable is the Poisson's ratio of the film instead of Young's modulus. The slope of linear variation not only depended on Poisson's ratio but also varied slightly with probe size. The analyses indicated that the effect of Poisson's ratio mismatch was relatively small (less than ten percent) up to contact radii that were 50% of the film thickness for the most severe situations.

5.2.3 Summary

The present study indicates that the mismatch of mechanical properties between the film and substrate has a more significant influence on the force profile than was previously thought. This becomes even clearer when we examine the strain contours of the strain, ε_{22} , normal to the interface (Fig. 5.8). It can be seen that there is a highly strained core beneath the contact region, which extends into the substrate. Mismatches in both Young's moduli and Poisson's ratios between the film and the substrate have a significant influence on the force profile of indentation on layered materials. Our study indicates that the Poisson effect was more significant than was previously thought. This can be attributed to the high degree of constraint in the contact region.

It was found that limiting the indentation depth to be less than 10% of the top film thickness, a commonly accepted rule of thumb for eliminating substrate effects, did not do so for a wide range of film to substrate moduli. When the contact radius is less than one-tenth of the film thickness (Figs. 5.3, 5.7), both the over- and underestimation of the Hertzian load was small (less than 10%). Thus, we conclude that the contact radius should be less than one-tenth of the film thickness in order for contact mechanics solutions for monolithic materials to be applied. This rule should work for a large range of film/substrate modulus ratios and the contact radius can be roughly estimated using the Hertzian value. Since all indenters have either spherical or pyramidal shapes with large apex angles, the proposed rule based on contact area should work for any indenter shape.

Although the normalized force follows linear relation with the contact radius, no empirical formula will be suggested for the present study because it is impractical to measure real contact area for nanoindentation. Instead, numerical analyses should be used when the contact radius exceeds one-tenth of the top film thickness.

5.3 ANALYSIS OF NANOINDENTATION OF γ -APS FILMS

In this section, the analyses of the IFM experiments on γ -APS films are presented. The thicker (4 μm) film was first analyzed by classical contact mechanics. This is followed by finite element analysis of thick and thin γ -APS films. Some guidelines and a suitable method of analyzing IFM experiments were established.

5.3.1 Nanoindentation of γ -APS films

Nanoindentation experiments of γ -APS films were performed on three samples (Table 3.1) under ambient temperature and humidity conditions: 1) a 4 μm thick γ -APS film cured at 100 $^{\circ}\text{C}$ for 3 hours, 2) a 46 nm thick γ -APS film cured under ambient conditions and 3) the same 46 nm thick γ -APS film cured at 100 $^{\circ}\text{C}$ for another 5 hours. Indentation experiments were conducted at several locations on each sample with spacing of 10 to 20 μm .

Due to the manner in which the γ -APS films were made and the resulting amorphous nature, some viscoelastic behavior could be expected during indentation. Figure 5.9 shows some typical IFM nanoindentation data from three

experiments on a 46 nm thick γ -APS film on silicon. The data were obtained from experiments that were conducted at three different loading-unloading rates: 1.31 nm/s, 2.61 nm/s and 5.22 nm/s. Figures 5.9a,b,c show the loading and unloading curves for each case. There was adhesion hysteresis (the retracting adhesion force is larger than the approaching one) at all rates. There was also indentation hysteresis at 1.31 nm/s (Fig. 5.9a). However, as the rate more than doubled, the indentation hysteresis disappeared (Fig. 5.9b,c).

Looking at Figures 5.9d,e, it can be seen that the slope of the loading curves (Fig. 5.9d) increased with increasing loading rates, while the unloading curves (Fig. 5.9e) overlapped. The slope variations in the loading paths became very small when the rate was above 2.61 nm/s. This indicates that, at high enough indentation rates, the γ -APS film behaved as an elastic material and time-dependent effects were minimized.

As a result of these preliminary observations, the loading and unloading rates used in all subsequent experiments were greater than or equal to 2.61 nm/s. In addition, only the loading paths were used in subsequent analyses so as to eliminate time-dependent effects due to either the piezo scanner or the sample properties. It was expected that these steps would give rise to the glassy or nearly glassy reduced elastic modulus $E^*(0)$.

5.3.2 Classical contact mechanics analyses

Since both the indentation depth and contact radius were small compared to the film thickness, the 4 μm thick γ -APS film on silicon could be treated as a

homogeneous material. To be more specific, the maximum indentation depth was approximately 8 nm. The tip radius was 240 nm as measured by SEM. Based on Hertzian theory, the maximum contact radius would be 44 nm. The actual contact radius would be less than 60 nm, considering the presence of adhesion interactions. Thus, for the 4 μm thick γ -APS film, the maximum contact radius was about 1.5% of the film thickness and the assumption of homogeneity was justified as explained in Section 5.2. It was therefore analyzed using Hertz, DMT, JKR and Maugis theories. Only the data from pull-off force to maximum compressive force or part of them could be used with these theories.

The nanoindentation data of the thick γ -APS film was first analyzed using Hertzian theory. This usually provides a first approximation even when adhesive interactions are present. To be consistent with the neglect of adhesive interactions in the Hertzian theory, only the compressive part of the force-separation data were used in the analysis (Fig. 5.10). A least-squares fit of the data was made to the expression

$$F = k(\delta - \delta_0)^{3/2}, \quad (5.4)$$

where

$$k = \frac{4}{3} E_f^* \sqrt{R}, \quad (5.5)$$

and δ_0 were the fitting parameters, and E_f^* was determined from k . The reduced modulus of 4 μm thick γ -APS film determined in this way was 1.92 ± 0.03 GPa.

For the DMT analysis, the force displacement data were fitted to

$$P = k(\delta - \delta_0)^{3/2} - P_c, \quad (5.6)$$

where k is given in Equation 5.5 and P_c is the pull-off force (maximum adhesive force). Three different fitting schemes were considered based on different choices of the free parameters among k , δ_0 and P_c . In the first scheme (Scheme I), the value of δ_0 was taken to be the position that corresponded to the pull-off force, the parameters k and P_c were then fit to the data. In the second scheme (Scheme II), the value of P_c was set to the measured pull-off force and the parameters k and δ_0 were fit to the data. A three-parameter fit was used for Scheme III where the values of P_c , k and δ_0 were obtained from the fit. Figure 5.11 shows the DMT fits to a force profile using the three different schemes. The average values of reduced Young's modulus and surface energy extracted from three experiments are listed in Table 5.1.

A modification of Equation 4.8 was used for the JKR theory analyses

$$\delta = k \cdot \left[\sqrt[3]{f^2 \left(\frac{P}{P_c} \right)} - \frac{4}{3} \sqrt[6]{f \left(\frac{P}{P_c} \right)} \right] + \delta_0 \quad (5.7)$$

where

$$k = \sqrt[3]{\frac{P_c^2}{K^2 R}} \quad (5.8)$$

and δ_0 is a free parameter, f is the function given by Equation 4.9 and $\frac{1}{K} = \frac{3}{4} \left(\frac{1-\nu_i^2}{E_i} + \frac{1-\nu_f^2}{E_f} \right)$. Two fitting schemes were adopted. The value of P_c was chosen to be the measured pull-off force and k , δ_0 were fit to the data using the least squares method. A three-parameter fitting scheme was used for the second. In both schemes, some data that were close to the pull-off force could not be used in analysis in order to avoid divergence. The overall fits are shown in Figure 5.12

and the values of the reduced modulus and work of adhesion from the two schemes are listed in Table 5.1.

For comparison purposes, the more complicated Maugis solution was also used to analyze the data. There are three fitting parameters (E_f^* , ω and μ) in Maugis' solution. The Maugis parameter μ (Eqn. 14) is a measure of the interaction between the indenter and the sample with JKR and DMT theories as the limit cases. The pull-off force can be expressed as $P_c = \alpha\pi\omega R$, where $\alpha = \frac{3}{2}$ or 2 in the JKR or DMT theories, respectively. In Maugis' analysis, where the Dugdale cohesive traction is constant (σ_0), the work of adhesion can be expressed as $\omega = \sigma_0\delta_t$, where δ_t is the cut-off displacement. By examining the data from the experiment on the 4 μm thick γ -APS film on silicon and taking $\omega \approx 87 \text{ mJ/m}^2$, $\delta_t \approx 50 \text{ nm}$ and using the material properties listed in Table 4.1 and reduced modulus determined by Hertzian theory, we found $\mu \approx 0.178$. Equation 4.16 was used to solve for m for a given value of \bar{a} . Then Equations 4.14 and 4.15 were used to calculate the force and separation, respectively. The best fit was achieved by adjusting the parameters E_f^* , μ , and ω . It was found that E_f^* had the greatest effect on the overall shape of the curve but has little effect on the value of P_c . On the other hand, ω and μ controlled the shape of the curve for $P < 0$. However, μ had little effect for $0.1 \leq \mu \leq 0.3$. Figure 5.13 shows a Maugis fit to one set of data. The overall fit was good. The average values of E_f^* , ω and μ were 1.6 GPa, 92 mJ/m^2 and 0.2, respectively.

The results of these contact classical mechanics analyses of the 4 μm thick γ -APS film on silicon are summarized in Table 5.1. These analyses indicated that

the extracted values depended upon the theories and the fitting schemes. All the correlation coefficients associated with the curve fits were very high. However, although the Hertz theory gave a very good fit for the compressive part of the force profile, the adhesive interactions were of the same order as the compressive force and therefore could not be neglected. Among all the contact mechanics theories, the more general Maugis theory should better describe the force profile. Comparison of the Maugis' results with DMT and JKR analyses showed that DMT (II) gave the similar results, in which the pull-off force was prescribed as the measured value. The Hertz theory overestimated the reduced elastic modulus due to the neglect of adhesive interactions. On examining the Maugis' parameter λ and checking the adhesion map [Johnson and Greenwood 1997], it was found the interactions in this part of the study were close to the DMT limit. Consequently, the DMT theory should describe this system better than the JKR theory. Although the Maugis theory is more complicated, the extracted reduced Young's modulus and work of adhesion were the same for both DMT (II) and Maugis analyses. However, despite the fact that the DMT theory is easy to use, it was found that the choice of the pull-force ($P_c = 2\pi\omega R$) had a strong effect on the value of the reduced modulus E_s^* that was extracted. Generally, higher values of P_c lead to lower values of E_s^* . The best fit was achieved when the pull-off force matched the measured value (DMT II). These results indicate the importance of matching the adhesive interactions when analyzing IFM experiments.

5.3.3 Finite element analysis

The maximum contact radius was approximately 60 nm as described in Section 5.4.1. This is larger than the thickness of a 46 nm thick γ -APS film. In addition, the system has two layers of thin films (γ -APS and SiO_2) on silicon. Therefore, none of the contact mechanics solutions considered above are applicable. Some elasticity solutions for some simplified situations [Yu et al. 1990, Kim 1996, Yoffe 1998] exist for a single film on a substrate. However, they do not account for multiple layers, spherical indenter and surface interactions. Thus, a finite element analysis incorporating user-defined interface interaction elements was used here. The thicker sample (4 μm γ -APS) was also analyzed for comparison purposes.

A triangular force-separation relationship (Fig. 4.7c) was used for the user-defined interface interaction elements throughout the analyses. There were four parameters in the analysis: the reduced elastic modulus E_f^* of the film and σ_0 , δ_t , and δ_0 . As might be expected, E_f^* mainly affected the slope from the pull-off point (maximum attractive force) to the maximum compressive force of the curve, while σ_0 , δ_t and δ_0 affected the region from very large separations to the pull-off point. E_f^* was adjusted first, followed by σ_0 and δ_t , which mainly affected the pull-off force. Then δ_0 was adjusted in order to manipulate the shape. It was usually necessary to make further adjustments in all parameters in two to three iterations. The full force-separation curves for all three samples were well fitted (Fig. 5.14) by the procedure just described.

As indicated in Section 5.2.2, the Poisson's ratio is also important. Two very different Poisson's ratio values of 0.0 and 0.36 were used. The value of 0.36 should be close to most amorphous polymers. The results of the finite element analyses are summarized in Table 5.2. The sample numbers (Column 1) are identified in Table 3.1. The surface energy was obtained from Equation 4.24. For a Poisson's ratio of 0.36, the reduced elastic moduli of the three samples followed the ranking: 3.16 ± 0.4 GPa for Sample 3 (46nm thick, 100 °C cure), 1.6 GPa for Sample 1 (4 μm thick, 100 °C cure) and 0.8 GPa for Sample 2 (46 nm thick, ambient cure). Since this value of Poisson's ratio should be reasonable for γ -APS and the ratio of probe size to film thickness is relatively small, the Poisson effect makes a 10% difference approximately. Thus, these values of reduced modulus should be very close to the real ones.

Both Sample 1 and 3 had the same surface energy (90 mJ/m^2). Sample 2, cured under ambient conditions, had the highest surface energy (114 mJ/m^2). It is noted that the samples with the same curing conditions had the same surface energy. For the thicker sample (1), finite element analysis and the Maugis solution yielded the same values for the reduced modulus and surface energy of the film, indicating that sample behaved as a homogeneous material.

The results suggest that the variation of elastic modulus and surface energy can be related to the curing of γ -APS. Samples 2 and 3 had the same thickness but different curing conditions. The modulus of Sample 2 was 0.8 GPa vs. 3.16 GPa for Sample 3. The surface energy of Sample 2 was greater than that of Sample 3. These two results suggest that Sample 2 was not fully cured and

therefore had a lower cross-link density. However, Samples 1 and 3 were subjected to the same curing conditions, which gave rise to the same surface energies but different moduli. Based on this, it is suggested that ethanol and water inside the film, which are released as the result of hydrolysis and condensation oligomerization, were the cause of the difference in moduli. It should be easy to remove these byproducts from the very thin 46 nm thick γ -APS film (Sample 3) by heating for several hours. Complete removal is less likely for the thicker film. Any solvents entrapped in the thicker film would lower its modulus. Thus we propose that the reduced elastic modulus of a completely cured γ -APS polymer sample is 3.16 ± 0.4 GPa.

5.3.4 Summary

The analyses of the thicker γ -APS films using contact mechanics theories indicated that extracted properties were sensitive to the choice of theory. Although the Maugis theory should be used for more general cases, the computation is complicated and the least squares fit is difficult to achieve. Different fitting schemes for the DMT and JKR theories resulted in different values of modulus and work of adhesion. The analyses showed that the pull-off force needed to be matched in order to achieve good fits. The reduced modulus of γ -APS polymer in this study was 3.16 ± 0.4 GPa, which falls in the expected range of amorphous polymers. This value is far smaller than that obtained by Cabibil et al. [2001]. In that work, it was found that a 50 nm thick γ -APS film on silicon had a modulus of 32 GPa, while the modulus of γ -APS film on glass dropped to 8

GPa. The softening of γ -APS on glass was attributed to the incorporation of Na^+ ions from the glass into the siloxane network of the film and breaking of crosslink. In both cases, the moduli were exceptionally high considering the amorphous nature of the γ -APS polymer. The data was analyzed using the Hertzian approach, which was not optimal. The indentation contact radius in their study was about the same as the film thickness although the adhesive interactions were small compared to the compressive force. The high moduli probably resulted from the strong influence of the substrate due to excessive indentation depth. In addition, on the basis of our present experience, flattening of tungsten tips can occur when indenting at high compressive force levels. Such flattened tips would also contribute to unexpectedly high moduli.

5.4 ANALYSES OF NANOINDENTATION OF OTS SELF-ASSEMBLED MONOLAYERS

The thicknesses of OTS monolayer and the oxide layer of the silicon are several nanometers, while the radius of the IFM indenter was two orders larger. In addition, in order to obtain enough data, the indentation depth was usually about the half the film thickness. The corresponding contact radius was about 10 times the thickness, based on a Hertzian estimate. As a result, classical contact mechanics theories for monolithic materials cannot be used to interpret the IFM experiments on such thin-layered materials due to the influence of the substrate. The finite element analysis described earlier (Section 4.3) was therefore used to analyze the experiments in this study.

5.4.1 Nanoindentation of self-assembled OTS monolayers

Nanoindentation experiments were performed under ambient temperature and humidity conditions on specimens consisting of bare silicon and silicon coated with an OTS self-assembled monolayer. Since both samples are stiffer than γ -APS, in order to acquire enough data, all experiments were performed at a displacement rate of 0.26 nm/sec for both loading and unloading. Even on bare silicon, where no time dependence is expected, the unloading path was consistently lower in displacement for a given force (Fig. 5.15a). This was due to the creep and hysteresis of the piezoelectric scanner that controls the displacement at such low speeds. The effect of this hysteresis is that unloading appears to occur faster than it actually does. In view of the expected lack of time dependence in the response of bare silicon, the piezo calibration for unloading was adjusted so that there was no path dependence between loading and unloading (Fig. 5.15b). Also shown in Figure 5.15b are the results of a finite element analysis which made use of the known properties of silicon and silica. This indicated that small adjustments in both the displacement and force calibrations were needed. The force calibration was adjusted first by making the slope of the data in the compressive regime match that of the analysis. The reference points for the displacement calibration were the points where the forces were at their minimum and zero values. The displacement calibration was adjusted to bring the measured and predicted values into agreement at these locations. This step made the finite element response stiffer in the compressive regime so that the force calibration had to be slightly reduced. Several iterations in displacement and force calibrations finally brought

the measured and predicted responses into close agreement (Fig. 5.15c). The data from this experiment on bare silicon was used as the final calibration step because the material behavior and all geometric quantities were known. The same calibration was applied to all subsequent experiments. It is noted here that the linear analysis perfectly fitted the IFM measurements on bare silicon as shown in the inset of Figure 5.15c. It will be shown later this is not true for the OTS coated silicon.

Figure 5.16a shows a comparison of the loading and unloading force profiles of silicon surfaces without and with an OTS monolayer coating. The obvious differences between the two demonstrate that the IFM is capable of detecting the presence of such thin (2.5 nm) monolayers. The OTS-covered sample is clearly more compliant than the silicon (the inset of Fig. 5.16a) and hydrophobic nature of the OTS surfaces resulted in lower adhesion (Fig. 5.16b,c). It is interesting to see that there is no hysteresis between loading and unloading for the OTS sample in the compressive region (the inset of Fig. 5.16a). This can be attributed to the high degree of order in the OTS monolayer and to the fact that the indentation was performed on the carbon chains. For both surfaces, there is slight hysteresis in the adhesive region (Fig. 5.16b,c), i.e., the pull-off force is larger in the unloading path than that of loading. Most of this adhesive response consists of long-range interactions that are mainly due to condensation of water and the associated meniscus effect. At this stage, we have not attempted to minimize the humidity in our IFM experiments. The relative humidity was typically 30-40% in the experiments conducted here. There are jumps in the

loading curves of both samples, while no such jump can be observed for the unloading curve in the OTS-covered surface. This sudden onset of adhesive forces is attributed to concerted forces. The jump happened earlier for the OTS-covered surface than bare silicon in the loading. This is attributed to a concerted reorientation of the OTS layer as it becomes attracted to the probe or to the hydrophobic nature of the OTS, which may also have increased the mobility of the adventitious water, thereby lengthening the tail of the adhesive response. In the absence of OTS, the effect is solely attributed to the presence of adventitious water in the atmosphere between the hydrophilic IFM probe and the hydrophilic substrate. As the probe comes close to the surface, a column of water suddenly forms between the probe and the substrate due to capillary forces.

5.4.2 Sensitivity to layer thicknesses and mechanical properties

In considering the particular combinations of materials considered in this study, i.e. an OTS monolayer on silicon with an oxide layer, the next item that was considered was the effect of variations of the thicknesses of the oxide layer and the OTS monolayer on the force profiles. This essentially addresses the issue of uncertainties in the measurements of their thicknesses. Figure 5.17 shows the effects of different thicknesses of the oxide layer. In the analyses, the thickness of native oxide was varied from 0.5 to 3.5 nm. It can be seen that such a variation of native oxide thickness had little influence on the force profile when the Poisson's ratio of the OTS was either 0 or 0.44. Since the oxide layer usually has a stable thickness of 2.0 ± 0.1 nm, variations in its thickness clearly have a minimal effect.

The OTS monolayer thickness had a much larger effect for both Poisson's ratios than did the oxide layer (Fig. 5.18). However, the effect would still be small considering that the reported thickness variation of OTS monolayers in the present study fell in the range of 2.2 to 2.5 nm.

The Young's modulus of the OTS monolayer had the largest influence on force profiles (Fig. 5.19). Modulus values ranging from 0.5 to 72 GPa were considered in this analysis for the Poisson's ratios of 0 (Fig. 5.18a) and 0.44 (Fig. 5.18b). This indicates that nanoindentation experiments are indeed sensitive to the monolayer modulus.

Based on these results, the IFM force profiles are most influenced by the OTS modulus, followed by Poisson's ratio, OTS thicknesses, and SiO₂ thickness. Considering the relatively stable values of the thicknesses of OTS and SiO₂ layers, IFM nanoindentation on OTS monolayers can indeed be used to determine its mechanical properties.

5.4.3 Extraction of OTS modulus

Finite element analyses were used to extract the Young's modulus of the OTS monolayer, assuming that it behaves as an isotropic, linearly elastic material. Adhesive interactions had to be considered in these analyses because their effect is significant at the low force levels that were used in the experiments.

Previous finite element analyses of the γ -APS samples (Section 5.3.3) showed that the elastic properties determine the slope of the response from the maximum adhesive force to the maximum indentation force and the surface

energy ω determines the maximum adhesive force itself. The quantities σ_0 , δ_i and δ_0 of the traction-separation law adjust the shape of the force profile from long-range interactions to the maximum adhesive force region. For OTS covered samples (Fig. 5.20), the adhesive portion of the response was best fitted with $\sigma_0 = 37.5$ MPa, $\delta_i = 7$ nm, $\delta_0 = 5$ nm, corresponding to $\omega = 131.3$ mJ/m². The corresponding values for bare silicon (Fig. 5.15c) were 60 MPa, 7 nm, 3 nm and 210 mJ/m², respectively. Since the tungsten probe used in this study has a hydrophilic surface, these values are consistent with the fact that the OTS samples were more hydrophobic.

The Young's modulus of the OTS monolayer was then adjusted to fit the complete force profile. Two different values (0 and 0.44) of Poisson's ratio were considered. The latter value was determined from the results of the molecular dynamics simulation as will be described later. Figure 5.20 shows comparisons between the analyses and data. The extracted modulus of the OTS monolayer was 15 ± 5 GPa when Poisson's ratio was zero (Fig. 5.20a), and 6 ± 1.5 GPa for a Poisson's ratio of 0.44 (Fig. 5.20b). These values are higher than those (3.16 GPa) of amorphous γ -APS polymer films (Section 5.3.3). This is not surprising because OTS monolayers are close-packed and highly ordered films. The direction of the indentation force was such that it compressed the covalent carbon bonds and caused the chains to shorten as well as tilt. These types of interactions are expected to be stiffer than those associated with the pure van der Waals interactions associated with amorphous polymers. Tupper *et al.* [1994 a, b] conducted a molecular dynamics simulation of the compression of *n*-hexadecane

monolayer by gold plates. The Young's modulus that was extracted from the initial linear portion of the force profile was 22 GPa. The molecular chain length of *n*-hexadecane is shorter than that of OTS. Thus, it is reasonable that a monolayer with a shorter chain would be stiffer. Henda et al. [1998] conclude that the initial tangent moduli of monolayers of CH₃-(CH₂)₁₇-S- had values between 15 to 18 GPa. In both cases, the Young's moduli were extracted based on the assumption that the stress state was uniaxial. However, since periodic boundary conditions had been used to simulate the infinite in-plane extent of the films, the stress state was actually tri-axial. Thus, the Young's moduli should be lower by a factor of $\frac{1-\nu-2\nu^2}{1-\nu}$ (0.3 for a Poisson's ratio of 0.44), or an inferred value of about 5.0 ± 0.5 GPa. Nonetheless, these studies demonstrated that highly ordered organic films are much stiffer than amorphous ones.

A closer inspection (insets in Fig. 5.20) of the response predicted by the linear analyses reveals that the overall fit was poor, particularly at low and high force levels. The linearly elastic analyses could not replicate the whole force profile. This suggested that the mechanical behavior of an OTS monolayer could be quite non-linear and, therefore, a more complicated constitutive model was required. This was also motivated by the results from the molecular dynamics analyses that we now describe.

5.4.4 Molecular dynamics simulation of OTS compression

Molecular dynamics simulations were performed in this study in two stages. First, the self-assembled configuration of OTS on a silica surface was

determined. This configuration was taken as the initial one for the subsequent simulation of compression. The steady-state compression of an OTS monolayer with a tungsten plate was then simulated. In the analysis, the tungsten plane moved down in increments of 0.1 Å. The computation was performed in two stages. The molecular dynamics simulation model was first annealed for 20 ps. This relaxation process allowed the equilibrium state to be achieved. The simulation was then continued for another 100 ps for data collection. The molecular configuration at the end of a step was taken as the initial configuration for the next step and the tungsten plane was moved downwards another 0.1 Å. The process was repeated until the desired displacement (30 Å) of the tungsten plane was reached.

It is worth noting that in the simulation, the effective compression rate is roughly 10^8 times faster than experiment. That is, each 0.1 Å increment in distance is associated with 120 ps of equilibration and data collection. Whether this compression rate can yield reasonably accurate results depends on the system studied. If the important configurations that contribute at each height can be sampled at this time, or those configurations sampled have properties substantially the same as all of those accessed in the experimental ~1 sec time frame, the results should be valid. In the present case, the system is relatively well ordered, so that this is a favorable case. One does not expect large variations in molecular configuration to be sampled in either simulation or experiment. Earlier simulations of compression nanoindentation [Siepmann and McDonald 1993, Tupper et al. 1994 a, b, Henda et al. 1998] necessarily have the same behavior.

One expects glassy materials, which are disordered but do not exhibit substantial structural rearrangement on the experimental time scale to also be favorable cases, if an appropriate initial structure is used.

The simulation of the self-assembled monolayer without external stress indicated that the molecular chains had a slight tilt angle relative to the normal to the silica surface (Fig. 5.21). The average tilt angle was about 17° , which compares well with the 16° tilt angle inferred by the ellipsometry measurements. Under load, the trajectory of the atoms was followed and the stresses were averaged. Figure 5.22 shows the computed relationships between the normal stresses and the nominal strain in compression (z) direction. The simulation revealed a highly non-linear response even at low strain levels. Furthermore, besides the compressive stress in the loading direction, high lateral compressive stresses also existed. The difference between the two lateral stresses was negligibly small. As the deformation increased, these three compressive stresses became equal, indicating incompressible behavior. Some kinks can also be seen in the response. These kinks maybe related to changes in conformation. The non-linear response is quite reminiscent of a rubbery material and motivated the following continuum representation of the OTS constitutive behavior.

5.4.5 Non-linear elastic analysis

The non-linear stress-strain behavior that was obtained from the molecular dynamics simulation was represented by a non-linear elastic material model. At this stage, the OTS monolayer was still considered to be isotropic. This neglected

the expected anisotropy associated with the highly ordered structure. The non-linearity was accounted for by the hypo-elastic material model. Rewriting Equation 4.31, the constitutive equation for hypo-elastic material becomes

$$d\varepsilon_i = \frac{1}{E_t} \left[d\sigma_i - \nu_t (d\sigma_j + d\sigma_k) \right], \quad (5.9)$$

where i, j and k represent the x, y and z -directions and E_t, ν_t are tangent modulus and Poisson's ratio, respectively. Both E_t and ν_t are generally functions of the strain invariants I_1, I_2 and I_3 . Based on the infinite lateral in-plane dimensions represented by the periodic boundary conditions in the molecular dynamics analysis, a uniaxial strain state exists where $d\varepsilon_x = d\varepsilon_y = 0$ (Note: In this section all strains are logarithmic). For a uniaxial strain, the tangent modulus and Poisson's ratio become

$$E_t = \frac{d\sigma_z}{d\varepsilon_z} - \nu_t \left(\frac{d\sigma_x}{d\varepsilon_z} + \frac{d\sigma_y}{d\varepsilon_z} \right) \quad (5.10)$$

and

$$\nu_t = \frac{\frac{d\sigma_x}{d\varepsilon_z}}{\frac{d\sigma_z}{d\varepsilon_z} + \frac{d\sigma_y}{d\varepsilon_z}}, \quad (5.11)$$

and $I_1 = \varepsilon_z, I_2 = I_3 = 0$.

Figure 5.23 shows the tangent modulus and Poisson's ratio derived from the results of the molecular dynamics simulation as a function of ε_z . The initial value of the tangent modulus (Fig. 5.23a) was about 1.5 GPa, which is close to that of typical polymers but for different reasons. In glassy amorphous polymers, the modulus is mainly determined by van der Waals interactions. In the compression of self-assembled monolayers, this low initial value was mainly due

to a rearrangement of the molecules. As the deformation increased, the tangent modulus increased to 30 GPa. This high value was caused by the high lateral constraint associated with the close packing of the OTS. On the other hand, Figure 5.23b shows that the tangent Poisson's ratio did not change with ε_z . The values of the Poisson's ratio were scattered about an average value of 0.44. The following equations for the tangent modulus E_t were obtained from the fit

$$E_t = \begin{cases} 1.5367 + 2.0504\varepsilon_z & |\varepsilon_z| < 0.089 \\ -2.2655 + 41.889\varepsilon_z + 37.625\varepsilon_z^2 & |\varepsilon_z| > 0.089 \end{cases} \quad (\text{GPa}). \quad (5.12)$$

Note that some of the points that were obtained from the molecular dynamics simulation were ignored in the fit shown in Figure 5.23a. These points corresponded to the kinks in the response (Fig. 5.22).

Figure 5.24 shows a comparison between the stress-strain behavior of OTS obtained from the hypo-elastic model and the molecular dynamics simulation. The hypo-elastic model fully reconstructed the stress-strain curve for nominal strains $\varepsilon_z < 0.4$, which was sufficient for simulating the IFM experiments.

This hypo-elastic constitutive model was then incorporated into the finite element analysis of the IFM experiments. The other materials were still considered to be linearly elastic and isotropic. Figure 5.25 shows the comparison of this non-linear elastic analysis with the data from the experiment. This simple non-linear model provided a much closer match with the experiment than the linear analyses (Fig. 5.20). This was true at both low (insets of Figs. 5.20 and 5.25) and high force levels. The agreement between analysis and experiment in Figure 5.25 is remarkable, given that the constitutive law that was used in the

continuum model was based directly on molecular dynamics simulations without any adjustment. This result suggests that the behavior of the OTS is indeed simple enough that differences in the time scales of the molecular dynamics analyses and the actual experiments are not important. It appears that a class of problems has been opened up where spatial and temporal scales can be crossed in a relatively simple manner, and molecular dynamics analyses may be used to motivate continuum representations of self-assembled monolayers in a simple but direct manner. This may simplify the stress analysis of MEMS devices that use self-assembled monolayers as friction and stiction reducers.

5.4.6 Summary

The experiments conducted in this study demonstrated that the IFM has sufficiently high resolution in both force and displacement for conducting nanoindentation experiments on ultra thin films whose thickness is on the order of nanometers. The interpretation of the force profiles from such experiments is complicated by substrate effects and interface mismatch. The IFM force profiles are most influenced by the OTS modulus, followed by Poisson's ratio, OTS thicknesses, and SiO₂ thickness. Considering the relatively stable values of the thicknesses of OTS and SiO₂ layers. The IFM experiments showed that the OTS monolayers were elastic, even when the indentation depth was relatively large ($\delta/t \leq 0.4$). Linear elastic analyses of the IFM experiments suggested that the Young's modulus of OTS monolayers is relatively high. These high values are not surprising given highly ordered structure of the OTS monolayers. However, the

linear elastic analyses were unable to fully match the measured force profiles. Molecular dynamics simulations were used to develop a non-linear constitutive model for OTS, which was highly nonlinear and could be represented as a hypo-elastic material. The IFM force profile was fully reproduced when the hypo-elastic behavior was incorporated in the finite element analyses. This result suggests that representations of the behavior of self-assembled monolayers that are obtained from molecular simulations can be readily incorporated in continuum analyses.

CHAPTER SIX

CONCLUSIONS

Introduction

Thin γ -APS films and self-assembled OTS monolayers were fabricated and characterized. They were used as samples for IFM nanoindentation studies. A new approach for making OTS monolayers with nano-scale uniformity was developed. Some guidelines for the indentation analysis were drawn from a parametric study of layer and substrate interactions. Its high resolution in both force and displacement allows the IFM to determine both the elastic mechanical and adhesive properties of thin films. Due to the different molecular structure of thin γ -APS films and self-assembled OTS monolayers, different analytical approaches were required. A continuum analysis was used for γ -APS films, while a hybrid continuum-molecular analysis was required for OTS monolayers.

New approach for OTS deposition

The quality of SAMs of ATS is sensitive to the deposition conditions, such as the amount of water, the temperature, and the substrate, particularly its initial condition. Controlling and manipulating these independent variables has not been uniformly realized to date.

The present study demonstrated the importance of eliminating the presence of water in making SAMs of OTS with nanoscale uniformity. An entirely new approach was developed for fabricating OTS monolayers on Si(100). Uniform and robust self-assembled monolayers were obtained under anhydrous conditions provided that the Si(100) surface was fully hydroxylated. The homogeneity of the mechanical behavior of OTS was confirmed by interfacial force microscopy while uniform topological properties were evident in atomic force microscope images. The monolayer character of the OTS coverage was confirmed by X-ray photoelectron spectroscopy, ellipsometry and patterning experiments. Analogous surfaces, prepared in the presence of moisture, exhibited non-uniform topological and mechanical properties. Cross-polymerization issues are central to the differences between hydrous and anhydrous processing. Our results, in agreement with the molecular modeling study of Stevens [1999], indicate that avoiding cross-linking is central to the formation of a mechanically and topologically uniform OTS monolayer.

Layer and substrate interactions

The present study indicated that the mismatch of mechanical properties between the film and substrate had a more significant influence on the force profiles of contact than was previously thought. The actual contact area departed from that of homogeneous samples, thereby causing over- and underestimation depending on the relative compliance of the film and substrate. Our study indicated that the Poisson effect was also significant. As a result, the modulus and

Poisson's ratio could not be grouped together as the reduced modulus. This was attributed to the high degree of constraint in the contact region. Consequently, accurate determinations of both modulus and Poisson's ratio of the film are equally important in indentation and therefore a separate experiment is required.

It was found that limiting the indentation depth to be less than 10% of the top film thickness, a commonly accepted rule of thumb for eliminating substrate effects, did not do so for a wide range of film to substrate moduli. In order to eliminate substrate effects, a new rule was proposed that the contact radius should be less than one-tenth of the film thickness. This rule should work for a large range of film/substrate modulus ratios and the contact radius can be roughly estimated using the Hertzian value.

IFM experiments

Nanoindentation experiments using an IFM were performed under ambient temperature and humidity conditions on specimens consisting of bare silicon, γ -APS films and silicon coated with OTS self-assembled monolayers. The IFM has sufficiently high resolution in both force and displacement measurement for detecting the presence of thin and ultra thin films. Due to the manner in which the γ -APS films were made and resulting amorphous nature, some time-dependent behavior could be observed during indentation. However, such a phenomenon could not be detected for self-assembled OTS monolayers. This can be attributed to the high degree of order in the OTS monolayer and to the fact that the indentation was performed on the carbon chains.

γ -APS

The analyses of the thicker γ -APS films using contact mechanics theories indicated that extracted properties were sensitive to the choice of the theory. In addition, different fitting schemes for the DMT and JKR theories resulted in different values of modulus and work of adhesion. The analyses showed that the pull-off force needed to be matched in order to achieve good fits. It was found that ethanol and water inside the γ -APS film, which are released as the result of hydrolysis and condensation oligomerization, were the cause of the difference in moduli. The reduced modulus of γ -APS polymer in this study was 3.16 ± 0.4 GPa, which falls in the expected range of amorphous polymers. This value is far smaller than that obtained by Cabibil et al. [2001]. In that work, it was found that a 50 nm thick γ -APS film on silicon had a modulus of 32 GPa, while the modulus of γ -APS film on glass dropped to 8 GPa. The softening of γ -APS on glass was attributed to the incorporation of Na^+ ions from the glass into the siloxane network of the film and breaking of crosslink. In both cases, the moduli were exceptionally high considering the amorphous nature of the γ -APS polymer. The data was analyzed using the Hertzian approach, which was not optimal. The indentation contact radius in their study was about the same as the film thickness although the adhesive interactions were small compared to the compressive force. The high moduli probably resulted from the strong influence of the substrate due to excessive indentation depth. In addition, on the basis of our present experience,

flattening of tungsten tips can occur when indenting at high compressive force levels. Such flattened tips would also contribute to unexpectedly high moduli.

OTS

Parametric studies indicated that the IFM force profiles were most influenced by the OTS modulus, followed by Poisson's ratio, OTS thicknesses, and SiO₂ thickness. Considering the relatively stable values of the thicknesses of OTS and SiO₂ layers, IFM nanoindentation on OTS monolayers can indeed be used to determine its mechanical properties.

Linear elastic analyses of the IFM experiments suggested that the Young's modulus of OTS monolayers is relatively high. These high values are not surprising given highly ordered structure of the OTS monolayers. However, the linear elastic analyses were unable to fully match the measured force profiles. Molecular dynamics simulations were used to develop a non-linear constitutive model for OTS at the continuum level. A hypo-elastic material model provided a convenient and accurate representation of the molecular dynamics results. The OTS force profile was fully reproduced when the hypo-elastic behavior was incorporated in finite element analyses of the IFM experiments. This result suggests that representations of the behavior of self-assembled monolayers that are obtained from molecular simulations can be readily incorporated in continuum analyses, mainly due the relative simplicity of the OTS molecules.

Future work

The present study essentially focused on the compressive response of OTS and adhesive interactions between it and the tungsten probe. The next step could be to consider using a functionalized tip to probe the sample. This could be achieved by depositing self-assembled monolayers with particular functional end groups on the IFM probe. By choosing the functional groups of both probe and sample, specific interactions can be studied in the adhesive region. Such experiments have already been conducted [Thomas et al. 1993, 1994, 1995, Keily and Houston 1998]. However, the analytical tools developed in this study would allow the force-separation law for different interactions to be extracted. This, in turn, could provide information at the molecular level for the study of interfacial fracture mechanisms, and how they relate to the intrinsic toughness. The results could be correlated with parallel macro- interfacial fracture experiments using the same functionality. However, this study requires some improvement to the current IFM device.

In the present study, the IFM experiments were conducted under ambient conditions. This could complicate interpretations of the experiment, especially in the adhesive region. A better environment can be achieved by placing the IFM head inside a high vacuum chamber. The results could then be correlated with parallel interfacial fracture experiments using SAMs with the same functionality.

Tables

Table 2.1: Group contribution to the molar refraction ($\lambda=589$ nm)

| Groups | R_{LL} | R_{GD} | R_V |
|--------------------|-----------------------|-----------------------|----------------------|
| -CH ₂ - | 5.644 | 8.82 | 17.66 |
| -CH ₃ | 4.649 | 7.831 | 20.64 |

Table 3.1: Samples of γ -APS film on silicon.

| Sample | Spin-coat | Cure | Thickness |
|--------|-----------------|--------------------------------------------|-----------|
| 1 | — | Ambient condition > 5 hrs, 3 hrs@100 °C | 4 μ m |
| 2 | 50 sec@2000 rpm | Ambient condition > 5 hrs | 46 nm |
| 3 | 50 sec@2000 rpm | Ambient condition > 5 hrs, 5 hrs@100 °C | 46 nm |

Table 3.2: Water contact angle measurements.

| Sample | Angle ($^{\circ}$) |
|----------------------|----------------------|
| Original surface | 25 \pm 1 |
| Hydroxylated surface | 22 \pm 1 |
| OTS (wet process) | 109 \pm 1 |
| OTS (anhydrous) | 109 \pm 1 |

Table 3.3: Thickness measurements.

| Technique | SiO ₂ thickness (nm) | Total thickness (nm) | OTS thickness (nm) |
|--------------|---------------------------------|----------------------|--------------------|
| Ellipsometry | 2.0 \pm 0.1 | 4.5 \pm 0.1 | 2.5 \pm 0.1 |
| XPS | 2.0 \pm 0.1* | — | 2.2 \pm 0.1 |

* Cabibil et al. 2001.

Table 4.1: Elastic material properties.

| Material | Elastic modulus E (GPa) | Poisson's ratio ν |
|-------------------------------|------------------------------------|---------------------------------------------|
| Tungsten ^a | 392 | 0.28 |
| SiO ₂ ^b | 73.6 | 0.17 |
| Silicon ^a | 168 | 0.22 |

Table 4.2: Atomic weight

| Atoms | O | H | Si | CH₂ | CH₃ | W |
|--------------|----------|----------|-----------|-----------------------|-----------------------|----------|
| Unit (a.m.u) | 15.9994 | 1.008 | 28.086 | 14.027 | 15.035 | 183.84 |

^a Simmons, G., and Wang, H., "Single Crystal Elastic Constants and Calculated Aggregate Properties: A HANDBOOK", 2nd Ed., The M.I.T. Press.

^b By Meller Optics, Inc.

Table 4.3: Parameter for harmonic bond potentials: $U(r_{ij}) = \frac{1}{2}k(r_{ij} - r_0)^2$

| i-j | <i>k</i> (kcal/mole) | <i>r</i>₀ (Å) |
|----------------------------------|---------------------------------|-------------------------------------|
| Si-O | 772 | 1.64 |
| O-H | 1106 | 0.945 |
| Si-CH ₂ | 520 | 1.9 |
| CH ₂ -CH ₂ | 520 | 1.53 |
| CH ₂ -CH ₃ | 520 | 1.53 |

r_{ij} is the distance between atoms labeled i and j .

Table 4.4: Parameter for harmonic valence angle potentials:

$$U(\theta_{jik}) = \frac{k}{2}(\theta_{jik} - \theta_0)^2$$

| j-i-k | <i>k</i> (kcal/mole) | θ_0 (°) |
|---------------------------------------------------|---------------------------------|--------------------------------------|
| Si-O-H | 110 | 122.9 |
| CH ₂ -Si-O | 160 | 114.9 |
| O-Si-O | 100 | 110.7 |
| Si-CH ₂ -CH ₂ | 126 | 120 |
| CH ₂ -CH ₂ -CH ₂ | 126 | 112.4 |
| CH ₂ -CH ₂ -CH ₃ | 126 | 112.4 |

θ_{jik} is the angle between bond vectors \underline{r}_{ij} and \underline{r}_{ik} .

Table 4.5: Parameter for cosine dihedral angle potentials:

$$U(\phi) = \frac{A_1}{2}(1 + \cos \phi) + \frac{A_2}{2}(1 - \cos 2\phi) + \frac{A_3}{2}(1 - \cos 3\phi)$$

| i-j-k-n | A_1 (kcal/mole) | A_2 (kcal/mole) | A_3 (kcal/mole) |
|--------------------------------------------------------------------|-----------------------------------------|-----------------------------------------|-----------------------------------------|
| CH ₂ -Si-O-H | 0.3 | 0.0 | 1.3 |
| Si-CH ₂ -CH ₂ -CH ₂ | -3.4 | 1.25 | 3.1 |
| O-Si-O-H | 0.0 | 0.0 | 0.0 |
| H-O-Si-O | 0.0 | 0.0 | 0.0 |
| O-Si-CH ₂ -CH ₂ | -2.5 | 1.25 | 3.1 |
| CH ₂ -CH ₂ -Si-O | -2.5 | 1.25 | 3.1 |
| CH ₂ -CH ₂ -CH ₂ -CH ₂ | -3.4 | 1.25 | 3.1 |
| CH ₂ -CH ₂ -CH ₂ -CH ₃ | -3.4 | 1.25 | 3.1 |

ϕ is the dihedral angle defined by $\phi_{ijkn} = \cos^{-1} \{ B(\underline{r}_{ij}, \underline{r}_{jk}, \underline{r}_{kn}) \}$ with

$$B(\underline{r}_{ij}, \underline{r}_{jk}, \underline{r}_{kn}) = \frac{(\underline{r}_{ij} \times \underline{r}_{jk}) \cdot (\underline{r}_{jk} \times \underline{r}_{kn})}{|\underline{r}_{ij} \times \underline{r}_{jk}| |\underline{r}_{jk} \times \underline{r}_{kn}|}$$

Table 4.6: Inter-molecular interactions were represented by the short-range (van der Waals) Lennard-Jones pair potentials:

$$U(r_{ij}) = 4\varepsilon \left[\left(\frac{\sigma}{r_{ij}} \right)^{12} - \left(\frac{\sigma}{r_{ij}} \right)^6 \right].$$

| i-j | ε (kcal/mole) | σ (Å) |
|----------------------------------|-------------------------------------------------|------------------------------------|
| W-Si | 0.0707 | 3.6 |
| W-W | 0.05 | 3.2 |
| W-O | 0.092 | 3.1 |
| W-CH ₂ | 0.0768 | 3.5525 |
| W-CH ₃ | 0.0935 | 3.5525 |
| O-O | 0.17 | 3.0 |
| Si-Si | 0.1 | 4.0 |
| Si-O | 0.1303 | 3.5 |
| CH ₂ -O | 0.1416 | 3.4525 |
| CH ₂ -Si | 0.1086 | 3.9525 |
| CH ₂ -CH ₂ | 0.118 | 3.905 |
| CH ₂ -CH ₃ | 0.1437 | 3.905 |
| CH ₃ -CH ₃ | 0.175 | 3.905 |
| CH ₃ -O | 0.1725 | 3.4525 |
| CH ₃ -Si | 0.1323 | 3.9525 |

Table 5.1: Contact mechanics analysis of the 4 μm thick γ -APS film on silicon.

| Theory | Reduced E_s^* (GPa) | ω (mJ/m²) | λ | Correlation R |
|---------------|---------------------------------------------|---------------------------------------------------|-----------------------------|---------------------------------------|
| Hertz | 1.91±0.02 | — | — | 0.998 |
| DMT (I) | 1.40±0.03 | 118.2±2.52 | — | 0.997 |
| DMT (II) | 1.60±0.01 | 87.73±1.76 | — | 0.999 |
| DMT (III) | 1.72±0.01 | 57.74±2.46 | — | 0.999 |
| JKR (I) | 1.53±0.03 | 116.98±2.35 | — | 0.997 |
| JKR (II) | 1.78±0.01 | 74.58±7.92 | — | 0.999 |
| Maugis | 1.60 | 92 | 0.2 | — |

Table 5.2: Finite element analysis of γ -APS films on silicon.

| Sample | Reduced $E_{\gamma-APS}^*$ (GPa) | | σ_0 (MPa) | δ_t (nm) | δ_0 (nm) | $\omega = \frac{\sigma_0 \times \delta_t}{2}$ (mJ/m ²) |
|--------|----------------------------------|---------------------------|---------------------|--------------------|--------------------|-----------------------------------------------------------------------|
| | $\nu_{\gamma-APS} = 0.0$ | $\nu_{\gamma-APS} = 0.36$ | | | | |
| 1 | 1.6 | 1.6 | 30.0 | 6.0 | 4.5 | 90 |
| 2 | 1.0 | 0.8 | 58.5 | 5.0 | 1.5 | 146 |
| 3 | 3.5±0.5 | 3.16±0.4 | 40.0 | 4.5 | 2.0 | 90 |

Table 5.3: Finite element analyses of OTS on silicon.

| Reduced E_s^* (GPa) | | σ_0 (MPa) | δ_t (nm) | δ_0 (nm) | $\omega = \frac{\sigma_0 \times \delta_t}{2}$ (mJ/m ²) |
|--------------------------|--------------|---------------------|--------------------|--------------------|-----------------------------------------------------------------------|
| $\nu = 0.0$ | $\nu = 0.44$ | | | | |
| 15±5 | 6±1.5 | 35 | 70 | 50 | 122.5 |

Figures

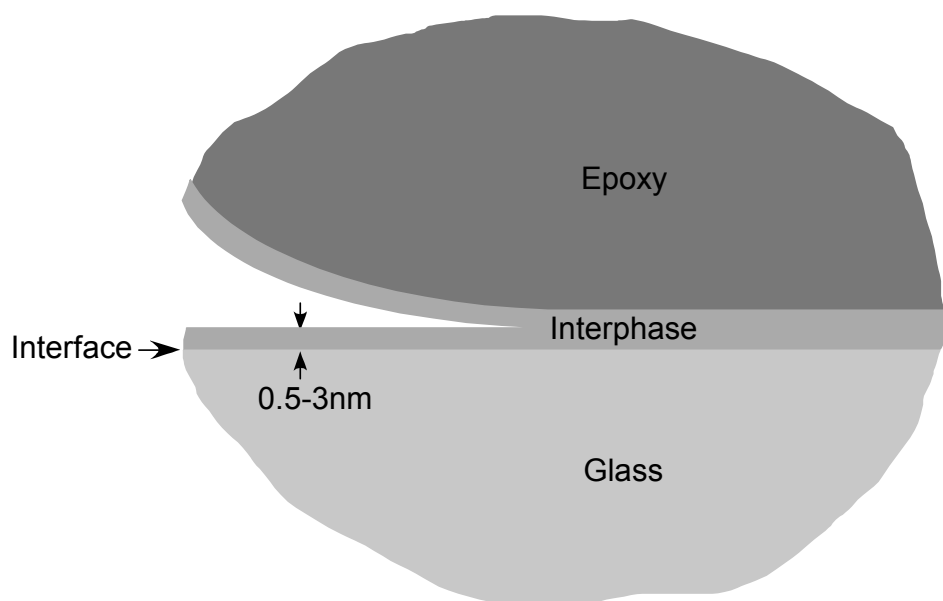


Figure 1.1 Schematic of interfacial fracture of an epoxy/glass specimen. Crack grows in the interphase.

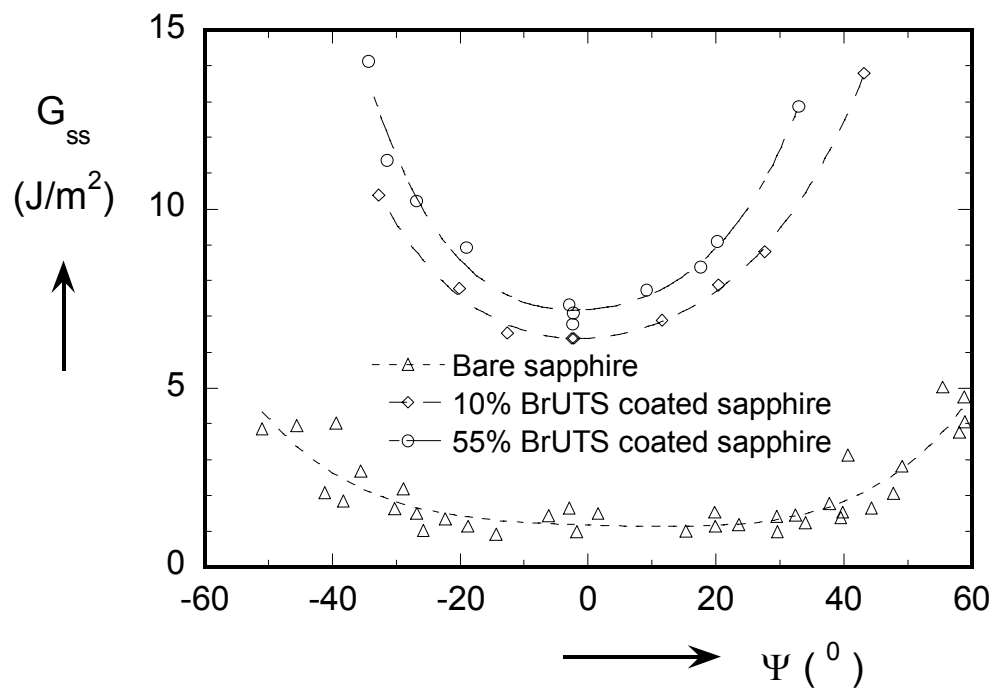


Figure 1.2 Comparison of the mixed-mode fracture envelopes of sapphire/epoxy with and without SAM. The SAMs were composed of 90%DTS-10%BrUTS and 45%DTS-55%BrUTS. [Mello 2004].

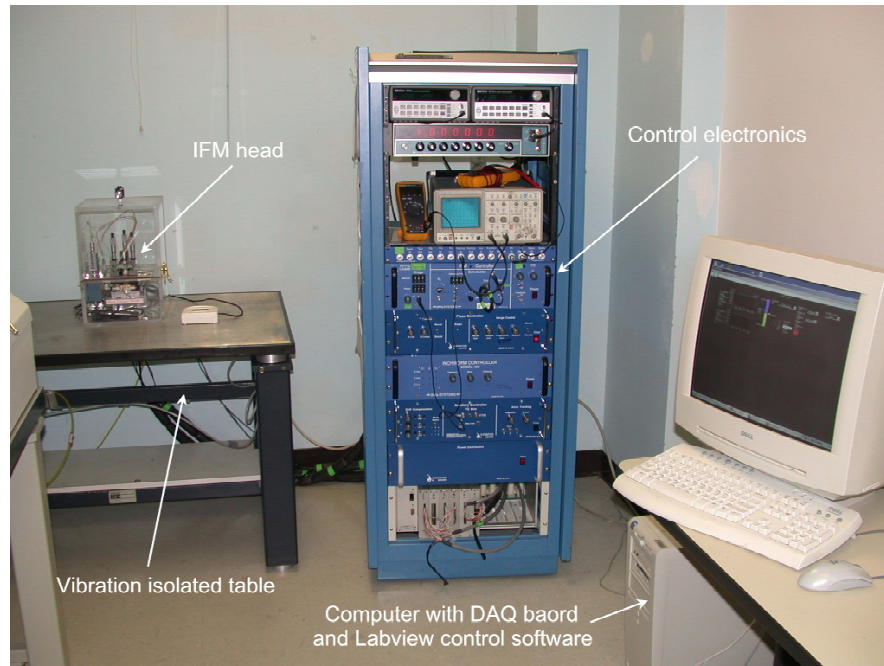


Figure 2.1 The main components of the IFM device: IFM head resting on a vibration isolated table, the control electronics tower and a computer equipped with LabView data acquisition board and control software.

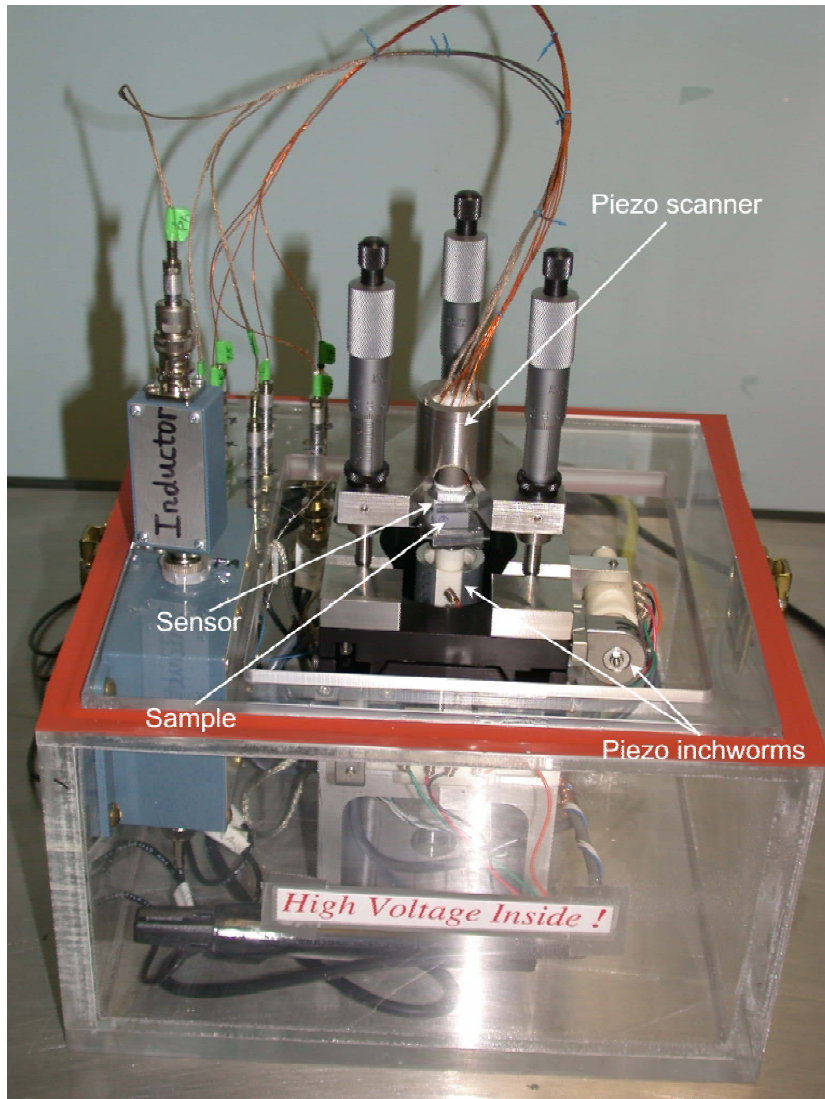


Figure 2.2 The head of the IFM.

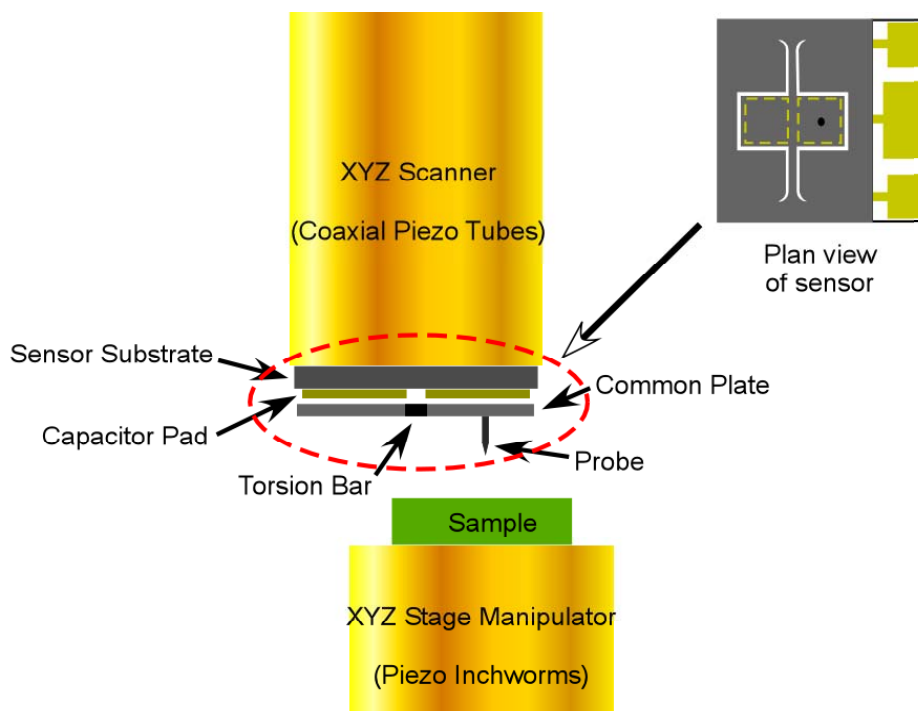


Figure 2.3 Schematic of an interfacial force microscope (IFM).

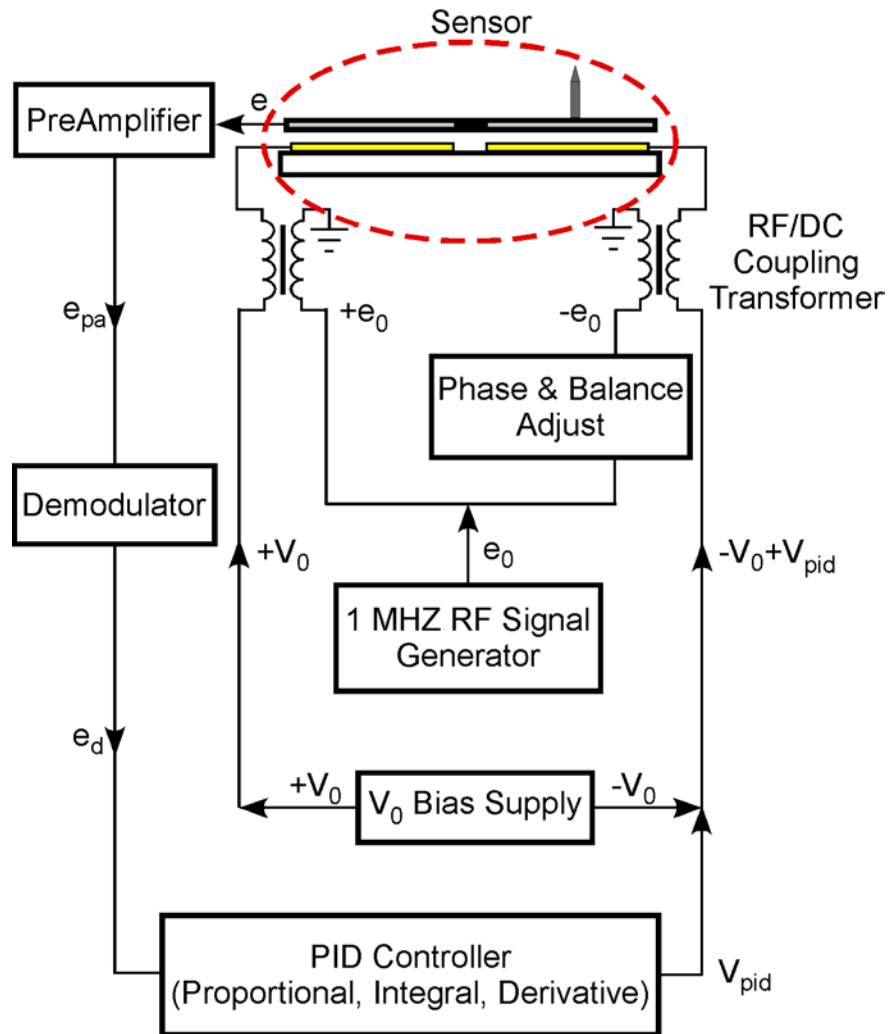


Figure 2.4 Schematic of feedback control circuit of interfacial force microscope (IFM).

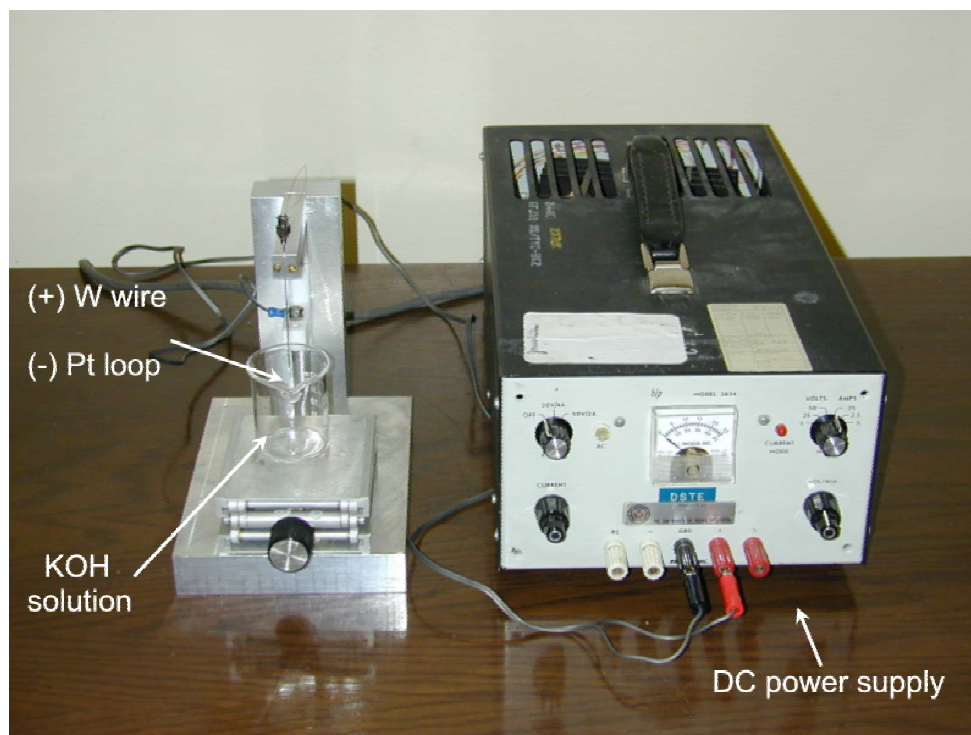


Figure 2.5 Setup for electrochemical etching of the tungsten tips.

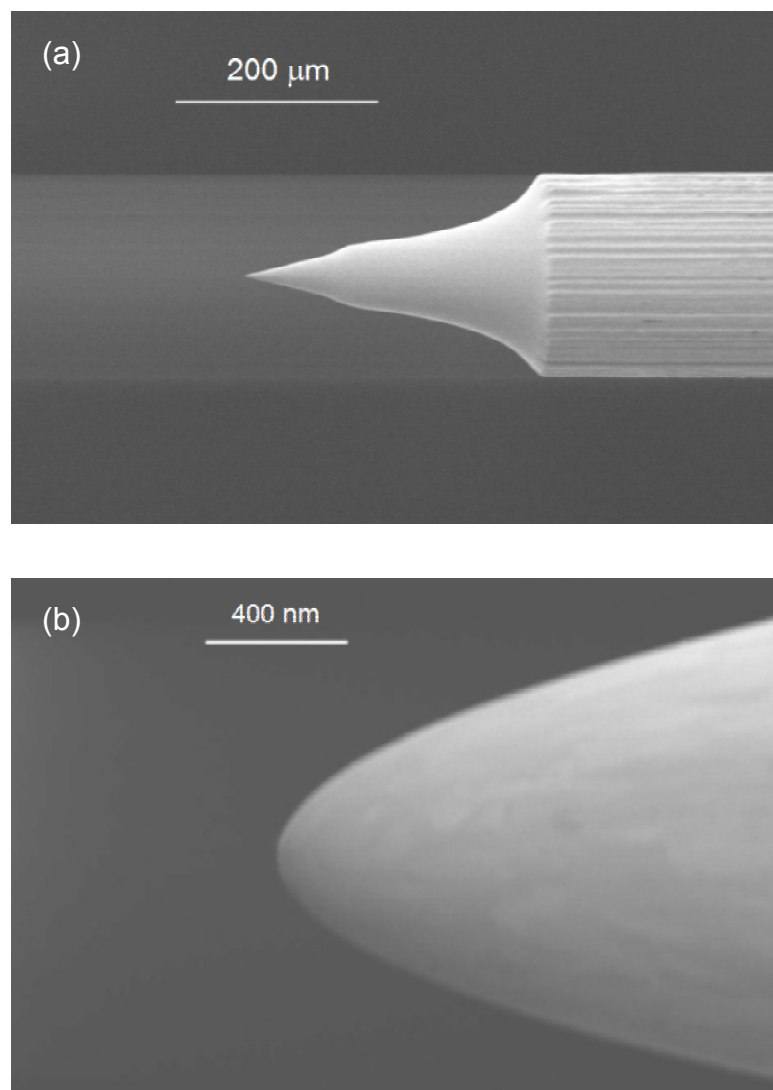


Figure 2.6 SEM images of electrochemically etched tungsten tips: (a) overall shape, and (b) magnified view of the tip.

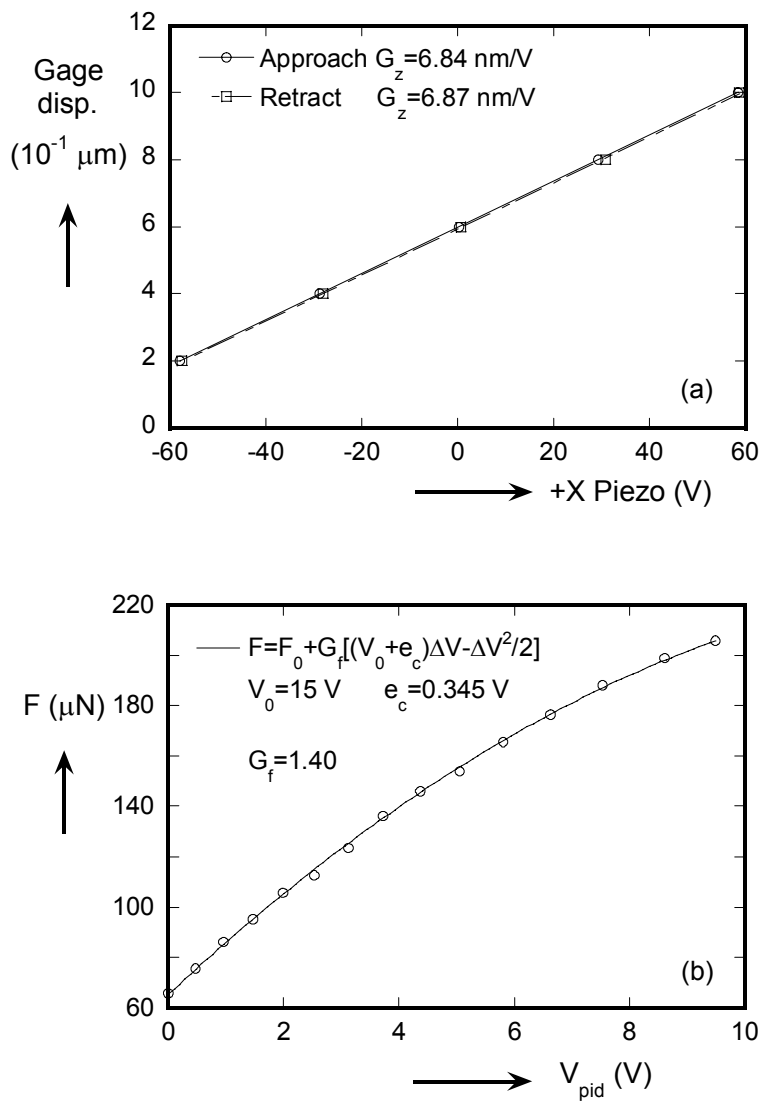


Figure 2.7 Displacement and force calibrations of the IFM. (a) Piezo calibration. The piezo gain is the slope of the linear fit. (b) Force calibration. The force gain of the sensor is extracted from the quadratic curve fit.

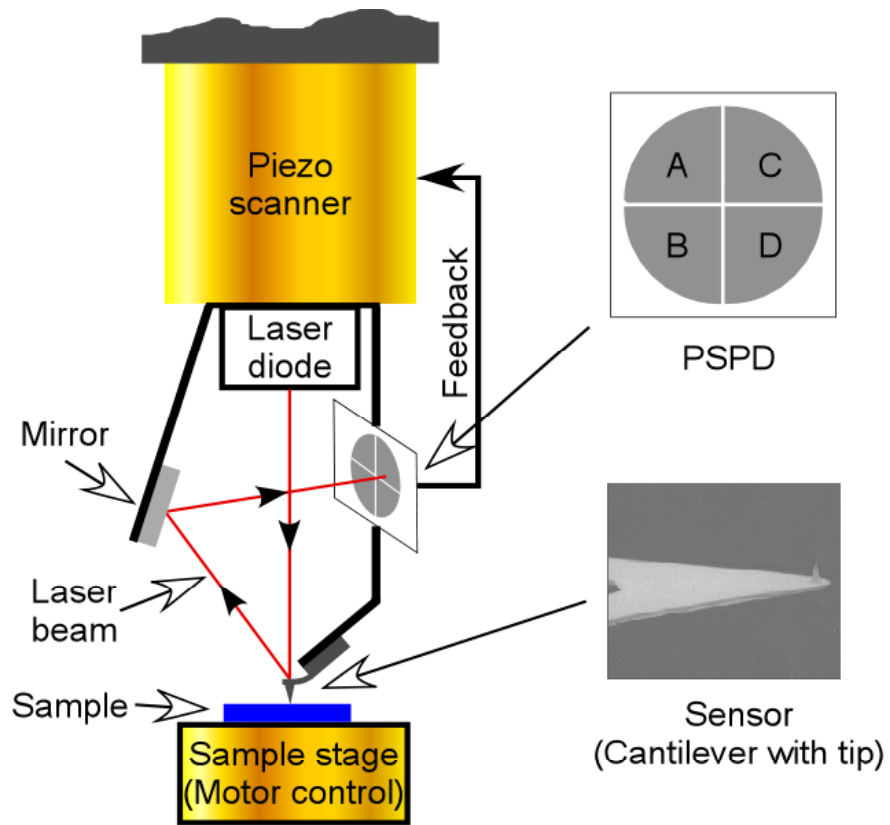


Figure 2.8 Schematic of an atomic force microscope (AFM).

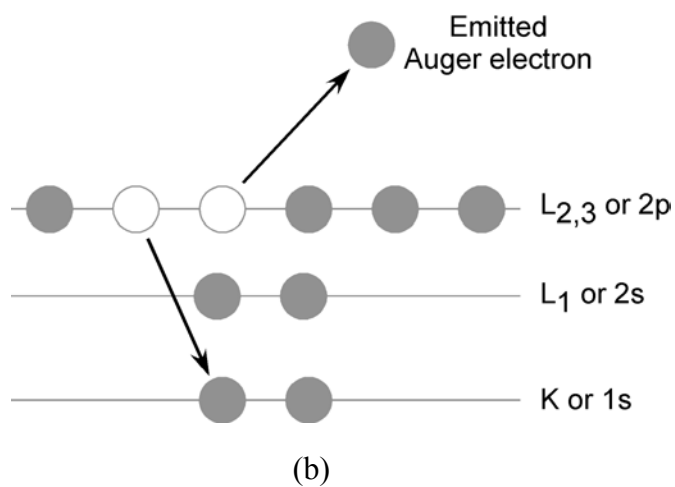
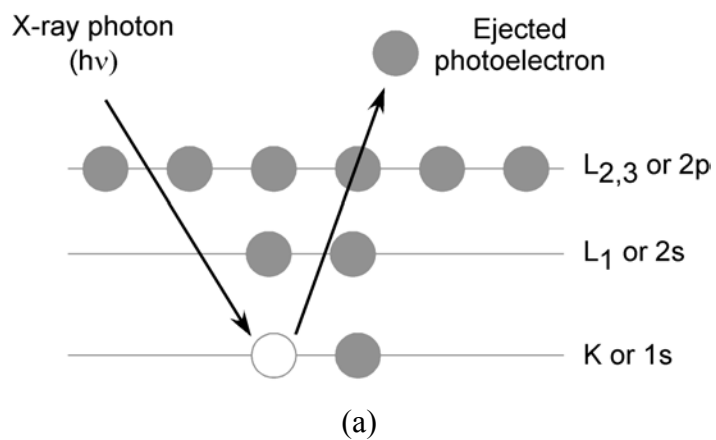


Figure 2.9 The photoelectric process of X-ray photoelectron spectroscopy: (a) ejection of photoelectron and (b) subsequent emission of Auger electron.

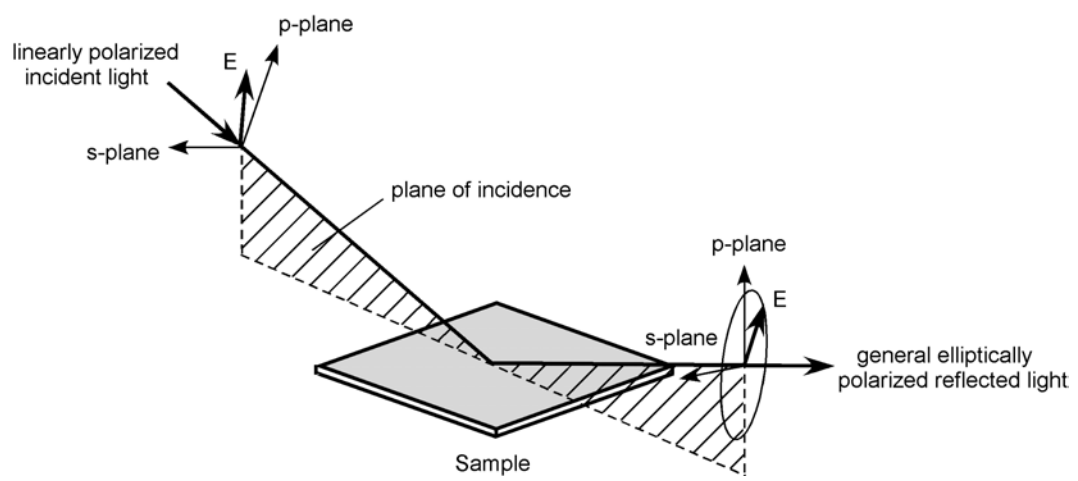


Figure 2.10 Schematic of ellipsometry.

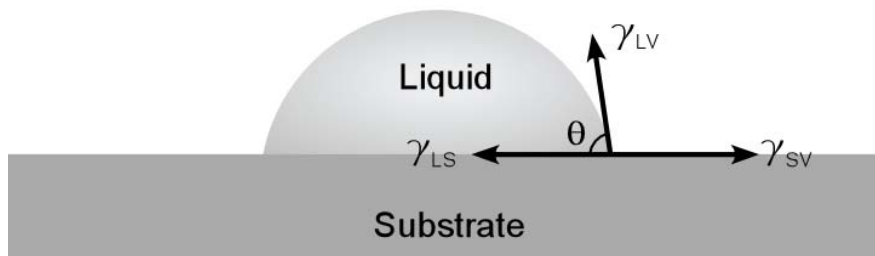
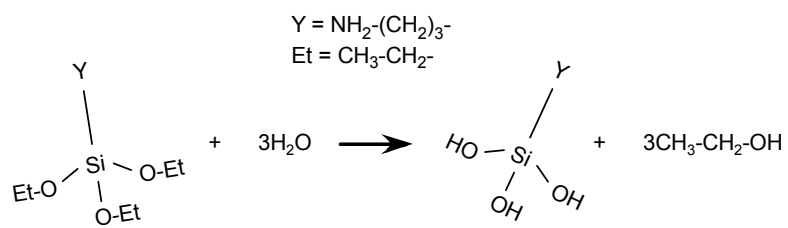
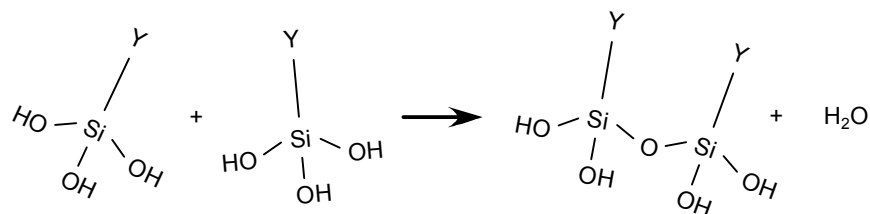


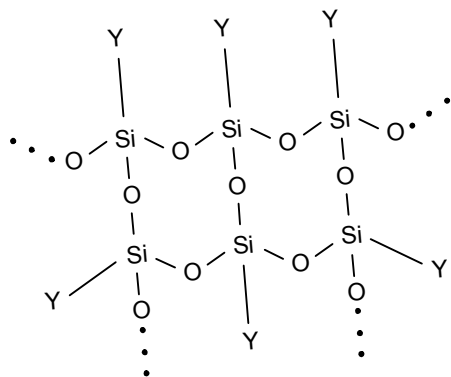
Figure 2.11 Contact angle of a liquid drop. Surface forces equilibrate at the corner.



(1) Hydrolysis



(2) Condensation/oligormization



(3) Idealized APS polymer

Figure 3.1 Chemical reactions of γ -APS in H_2O . [Cabibil 2001]

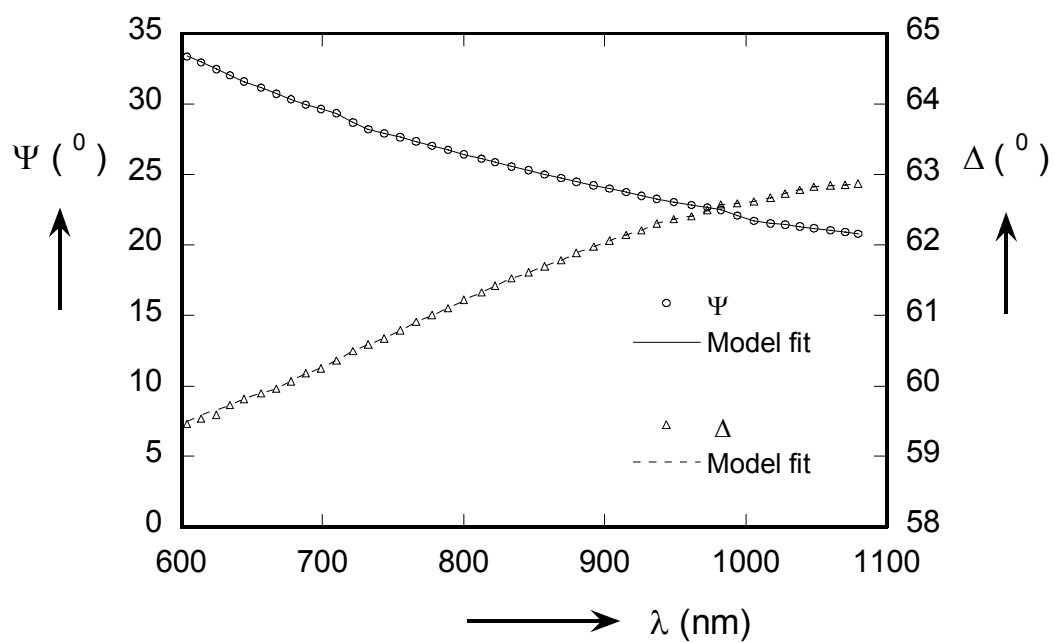


Figure 3.2 Typical ellipsometry data for γ -APS (46 nm) on silicon.

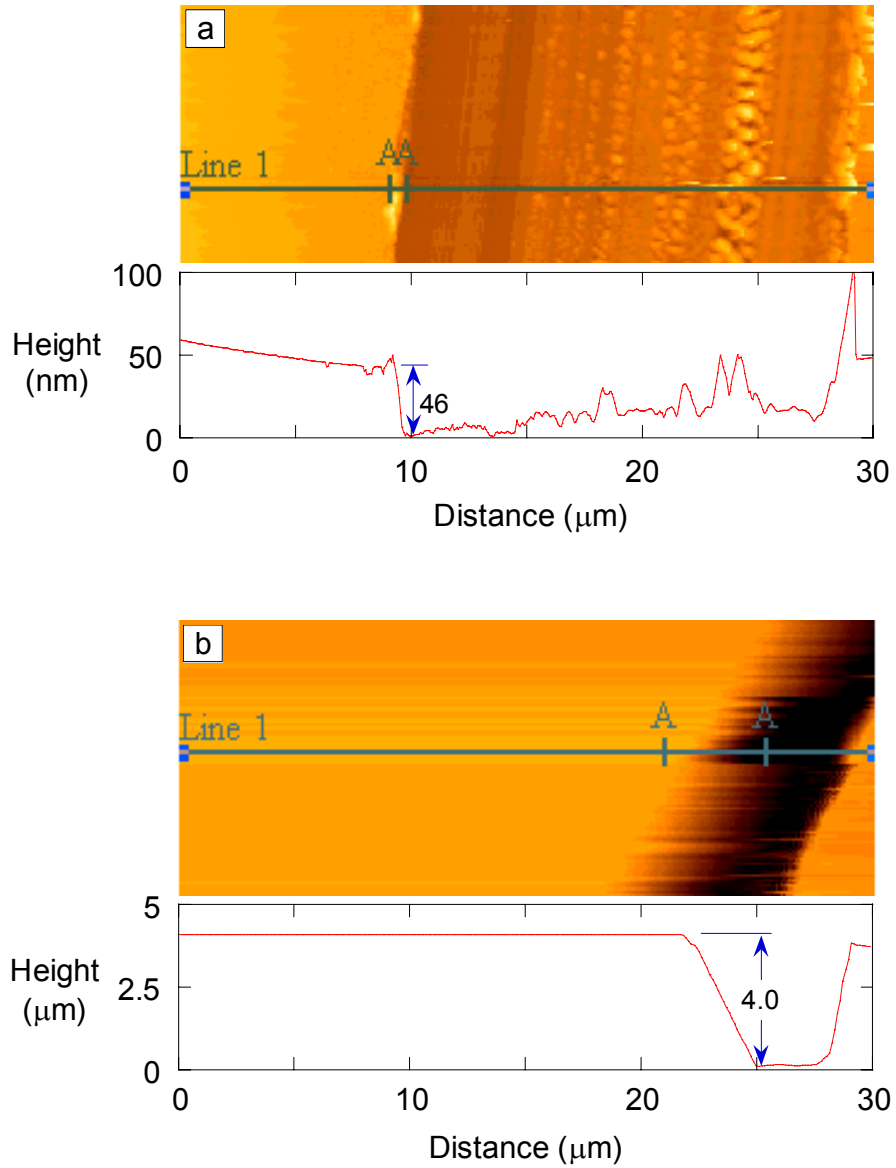
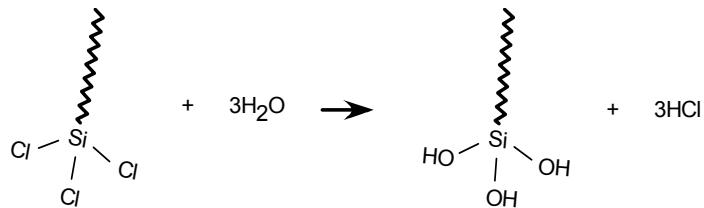
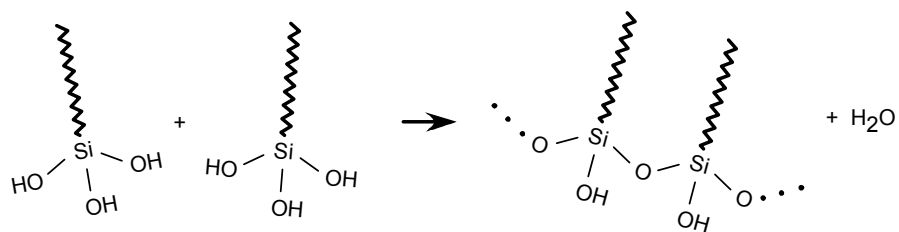


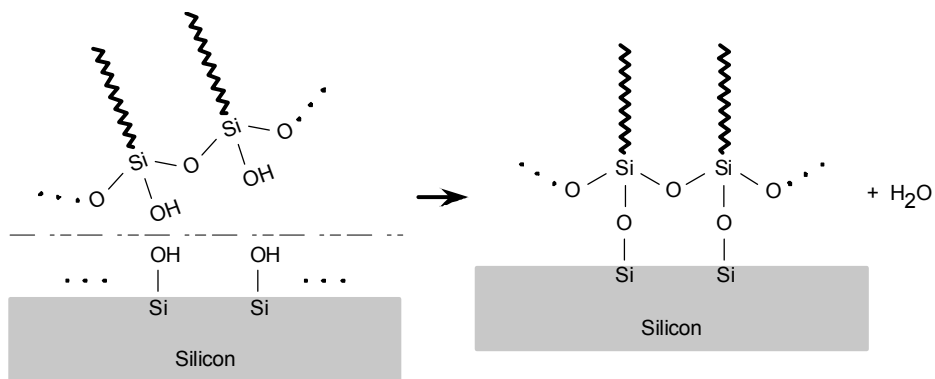
Figure 3.3 (a) An AFM scan of a scratch on γ -APS on silicon. It was used to measure the thinner film thickness. (b) An AFM scan of a channel crack in γ -APS on silicon. This was used for measuring the thickness of the thicker γ -APS film.



(1) Hydrolysis of silane group.



(2) Cross-polymerization.



(3) Chemisorption.

Figure 3.4 Self-assembly model of OTS with cross-linking in the presence of water.

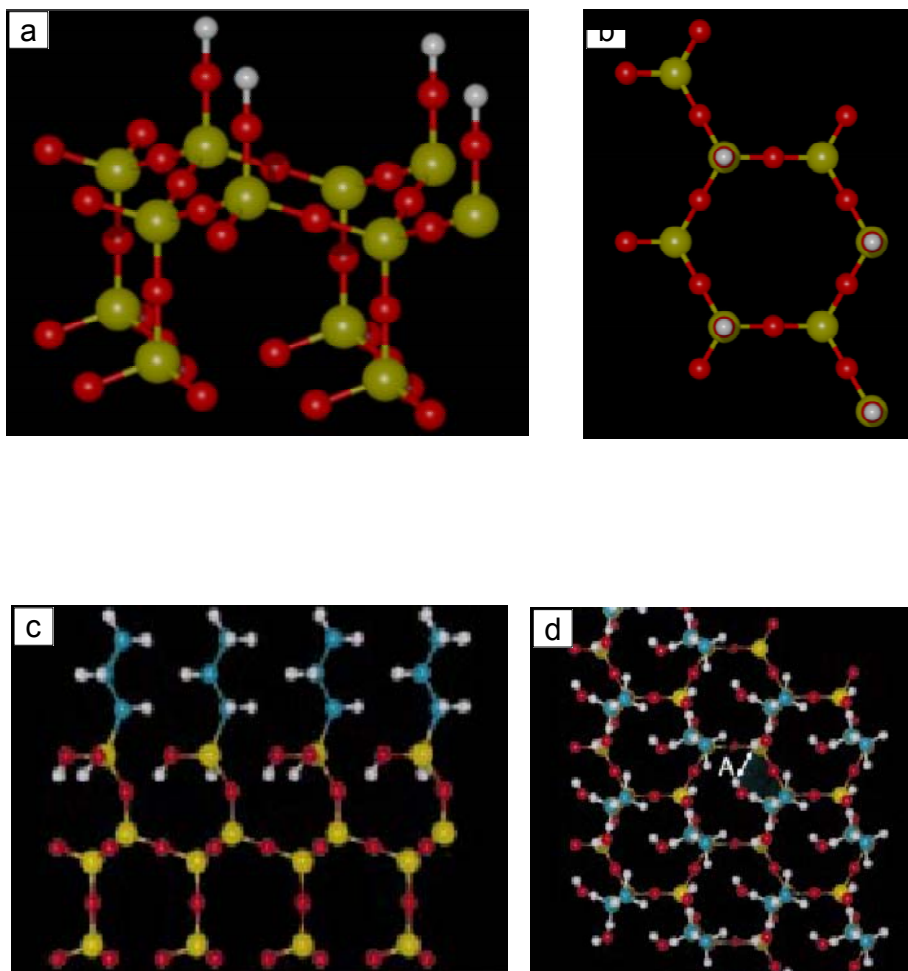
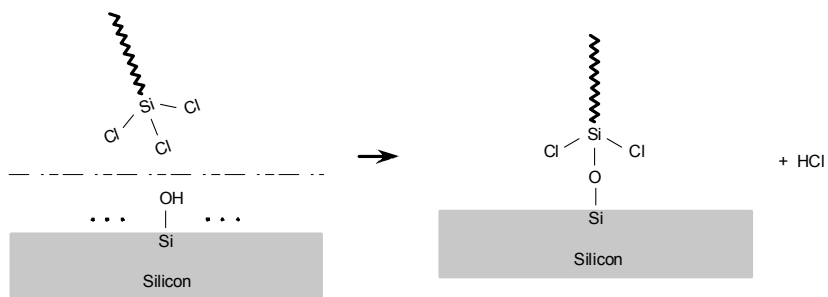
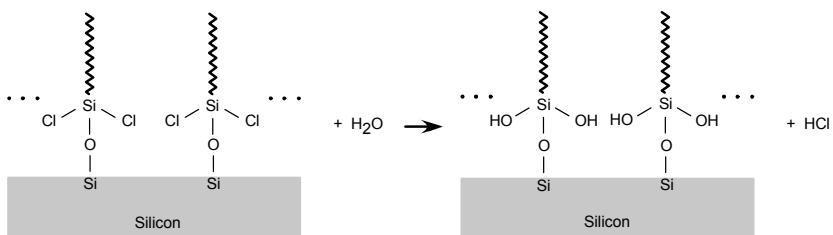


Figure 3.5 A three-dimensional representation of: (a), (b) the atomic structure of silica with hydroxyl groups ((a) side view and (b) plan view), and (c), (d) ATS chain on silica ((c) side view and (d) plan view) (O is red, Si is yellow, H is white and C is blue). [Stevens 1999]



(1) Anchoring the OTS molecules under anhydrous condition.



(2) Subsequent hydrolysis under environment conditions.

Figure 3.6 Self-assembly of OTS under anhydrous conditions.

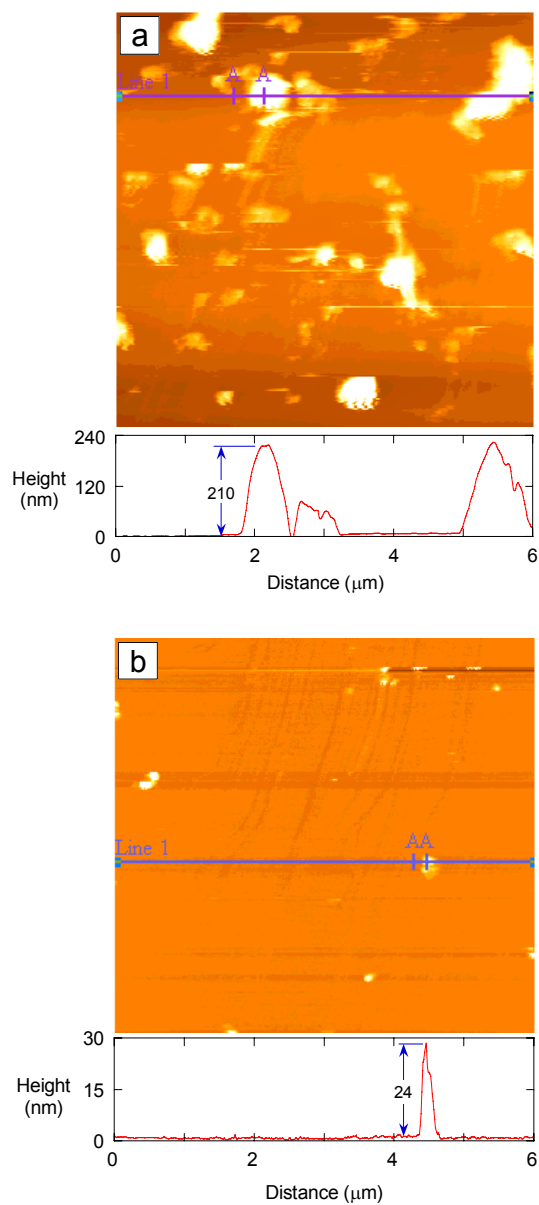


Figure 3.7 Low force contact mode AFM images of an OTS-covered hydroxylated oxidized Si(100). The OTS was added under hydrous conditions. (a) Image of a region that is covered with visually observable patches and (b) image of region that is visually clear.

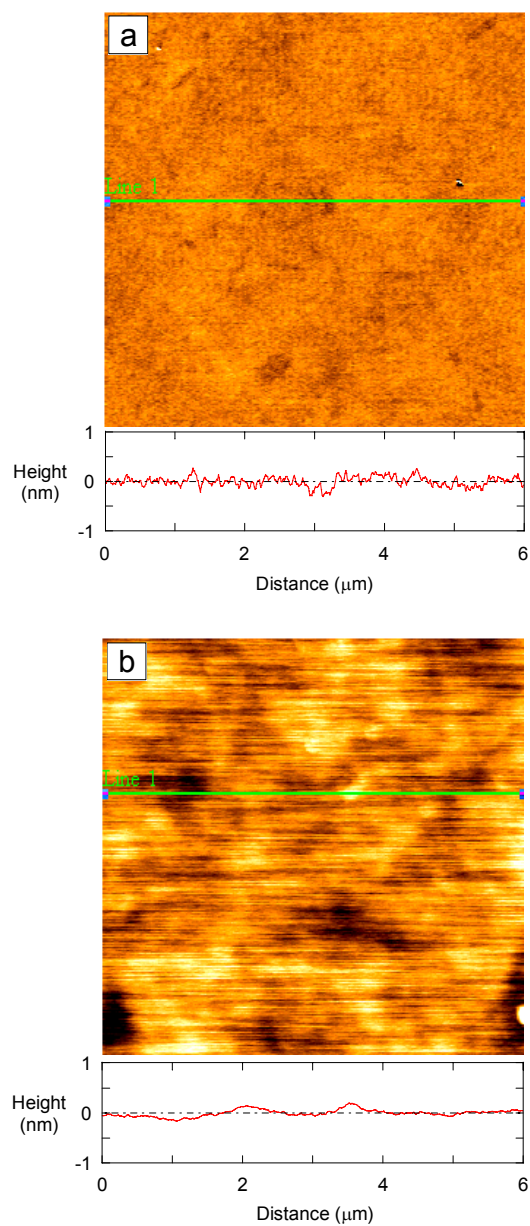


Figure 3.8 AFM images of OTS-covered hydroxylated oxidized Si(100). The OTS was added under anhydrous conditions. (a) Image of low force contact mode and (b) image of tapping mode.

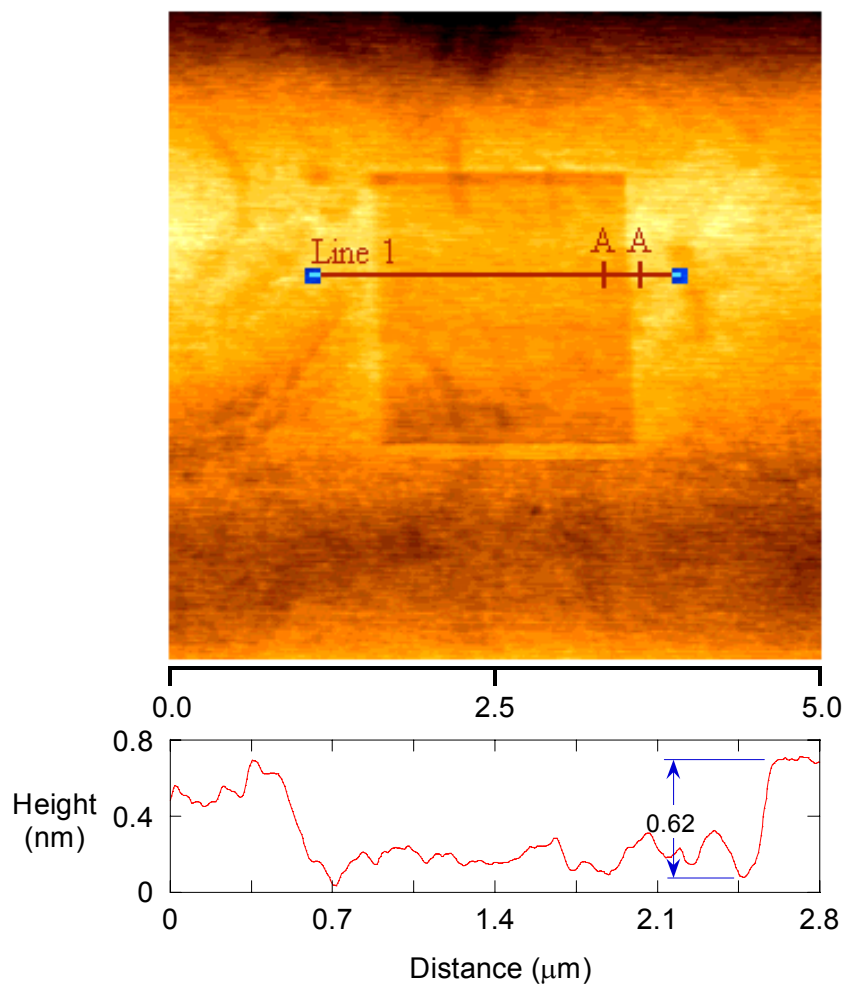


Figure 3.9 For an OTS-covered substrate prepared under anhydrous conditions, an image taken at low force after scratching the surface in the central region of the figure with the AFM tip under the highest applied force available ($1 \mu\text{N}$). A line scan is plotted beneath the image.

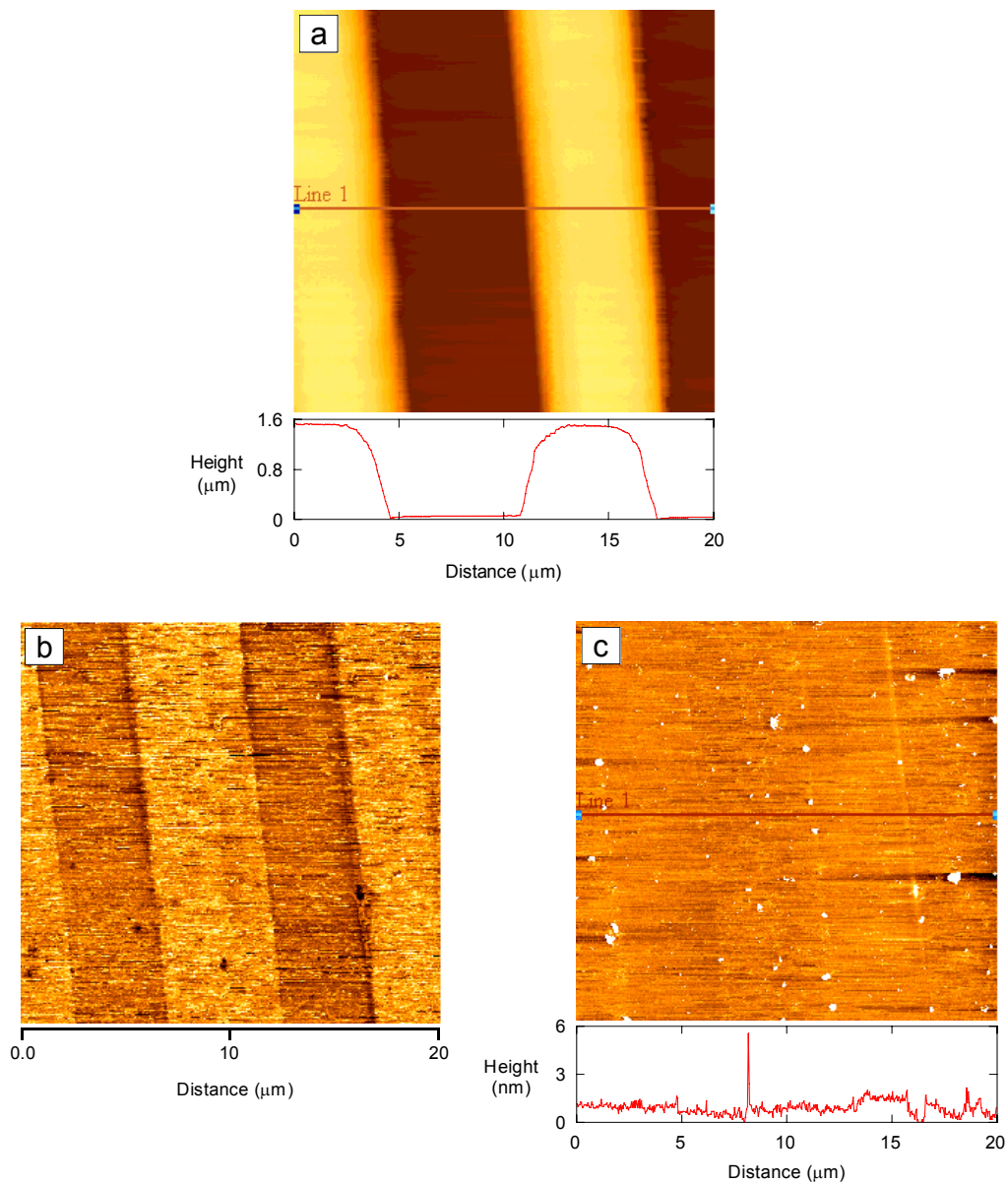


Figure 3.10 AFM images of micro-contact printing (μ CP) substrate: (a) silicon based master grid, (b) phase image of patterned OTS on silicon (100), and (c) non-contact topography image of the same patterned OTS.

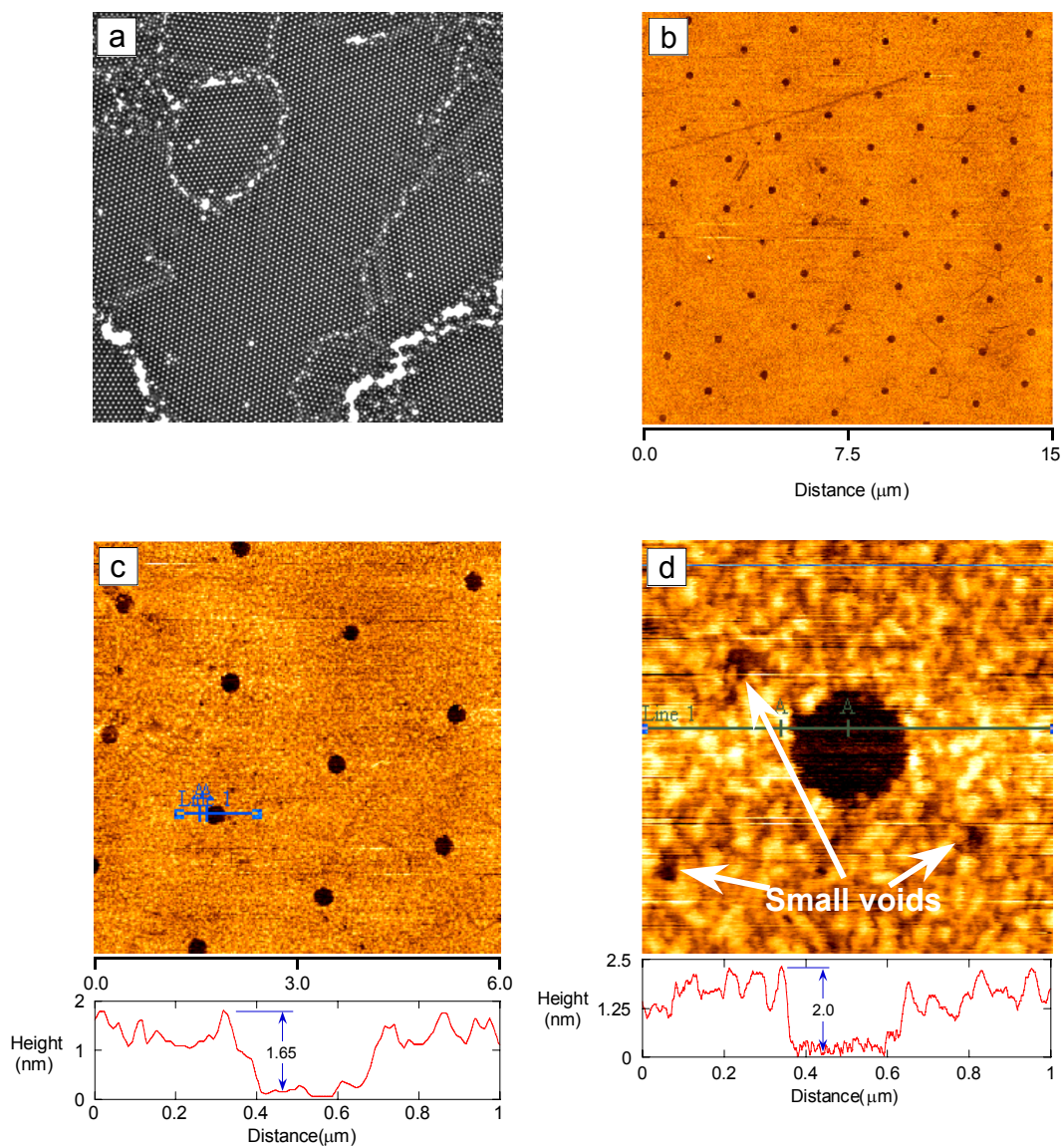


Figure 3.11 Patterning OTS with convectively assembled polystyrene beads: (a) an optical microscope image of a Si(100) surface covered with convectively assembled 2 μm diameter polystyrene beads; (b) , (c) and (d) are the AFM images of different scan size that were gathered after depositing OTS, under anhydrous conditions, and removing the beads.

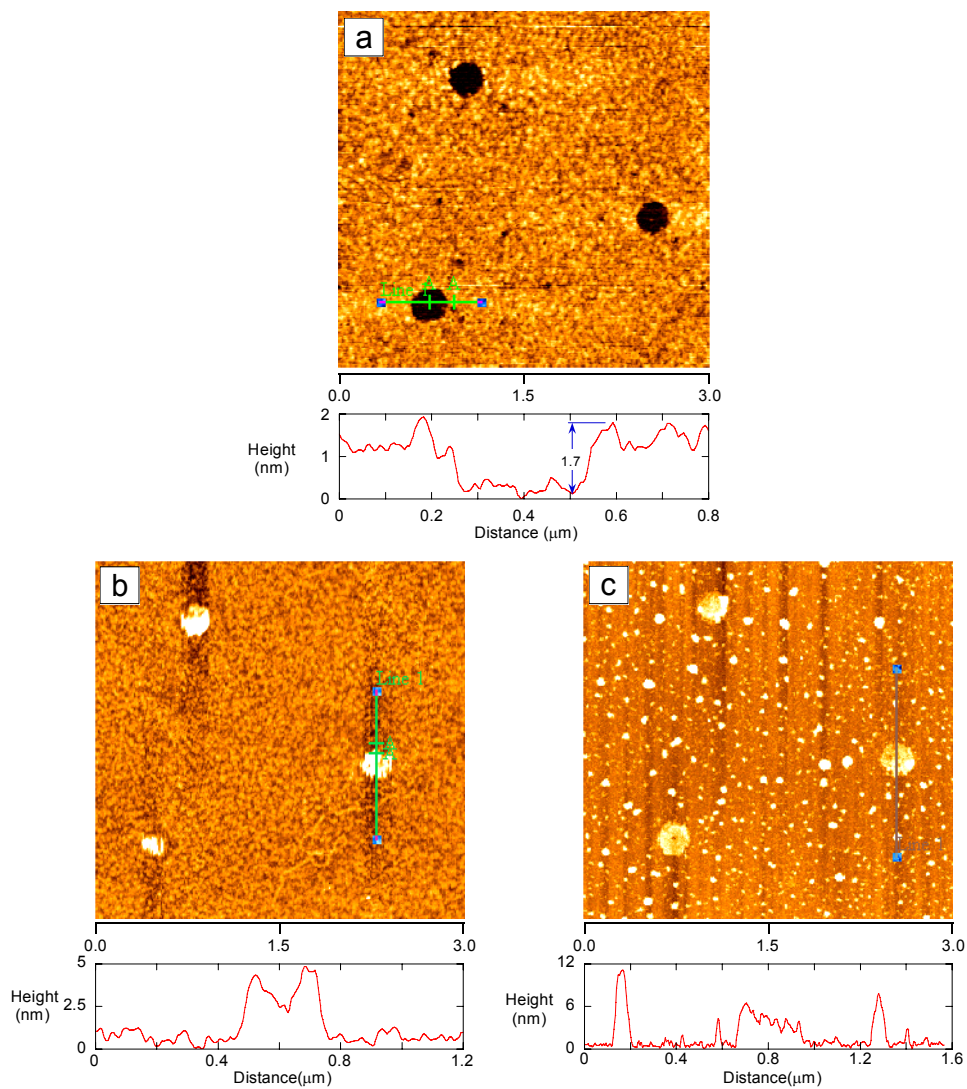


Figure 3.12 Comparison of AFM images ($3 \times 3 \mu\text{m}^2$) that were taken at different times. The OTS was patterned using convectively assembled polystyrene beads: (a) immediately following post processing, (b) after 8 hours and (c) after 20 hours.

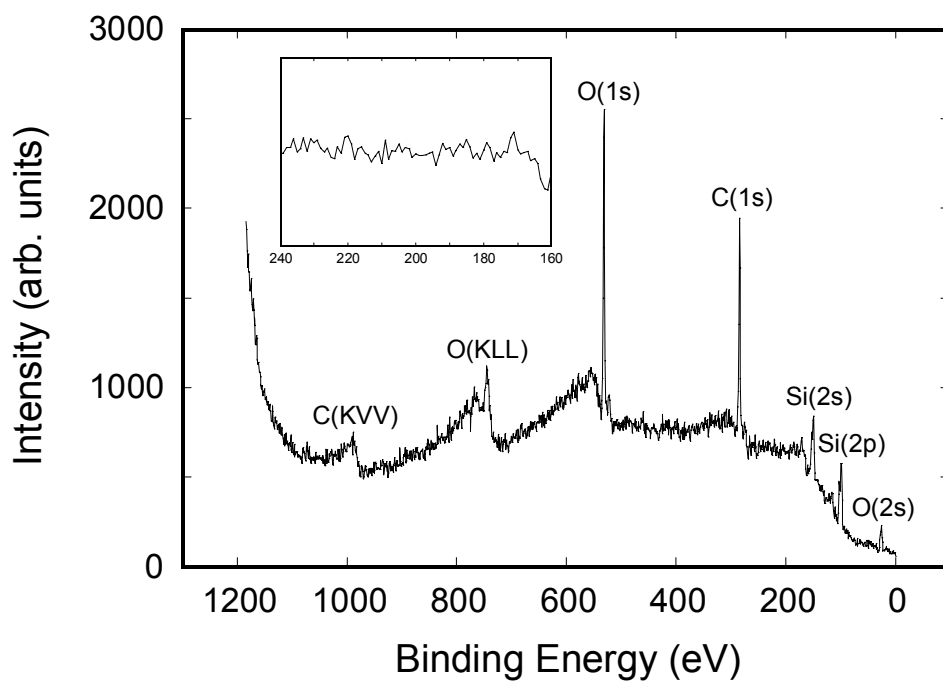


Figure 3.13 Broad XPS scan of OTS covered Si(100) surface. The peaks are all attributed as marked to either photoelectrons or Auger transitions, C(KVV) and O(KLL), on XPS transitions from C, O, and Si atoms with the XPS sampling depth.

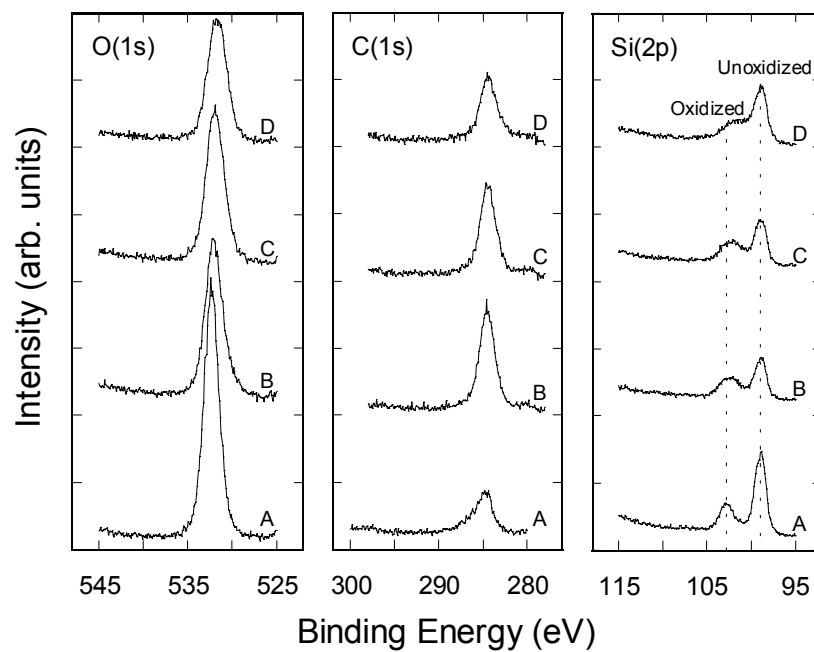


Figure 3.14 XPS scans for: (A) piranha etched Si(100) surface prior to exposure to OTS, (B) surface exposed to OTS under anhydrous conditions, (C) surface from (B) exposed to 5 keV He ions for 300 s, and (D) surface from (C) exposed to 2 keV Ar ions for 120 s.

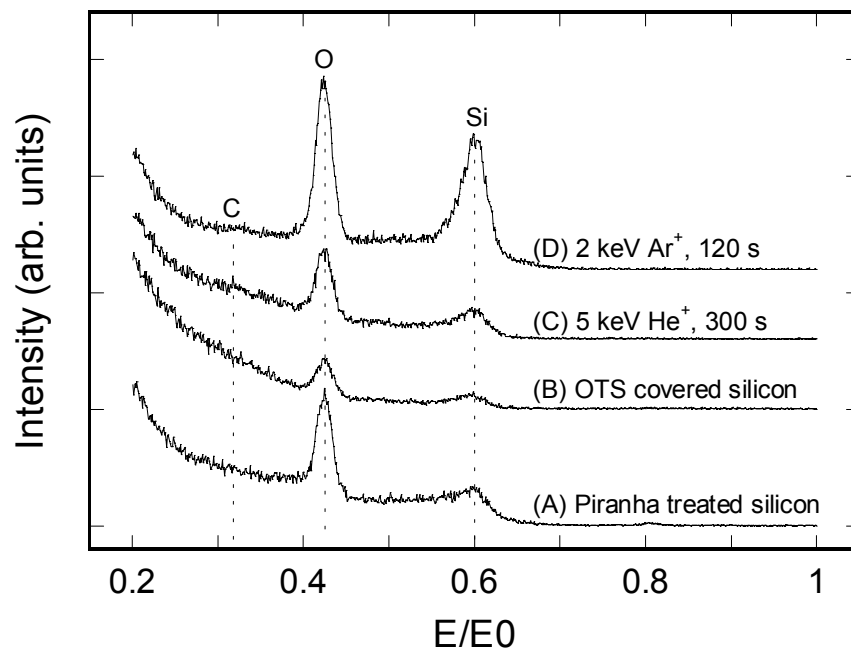


Figure 3.15 ISS for: (A) piranha etched Si(100) surface prior to exposure to OTS, (B) surface exposed to OTS under anhydrous conditions, (C) surface from (B) exposed to 5 keV He ions for 300 s and (D) surface from (C) exposed to 2 keV Ar ions for 120 s.

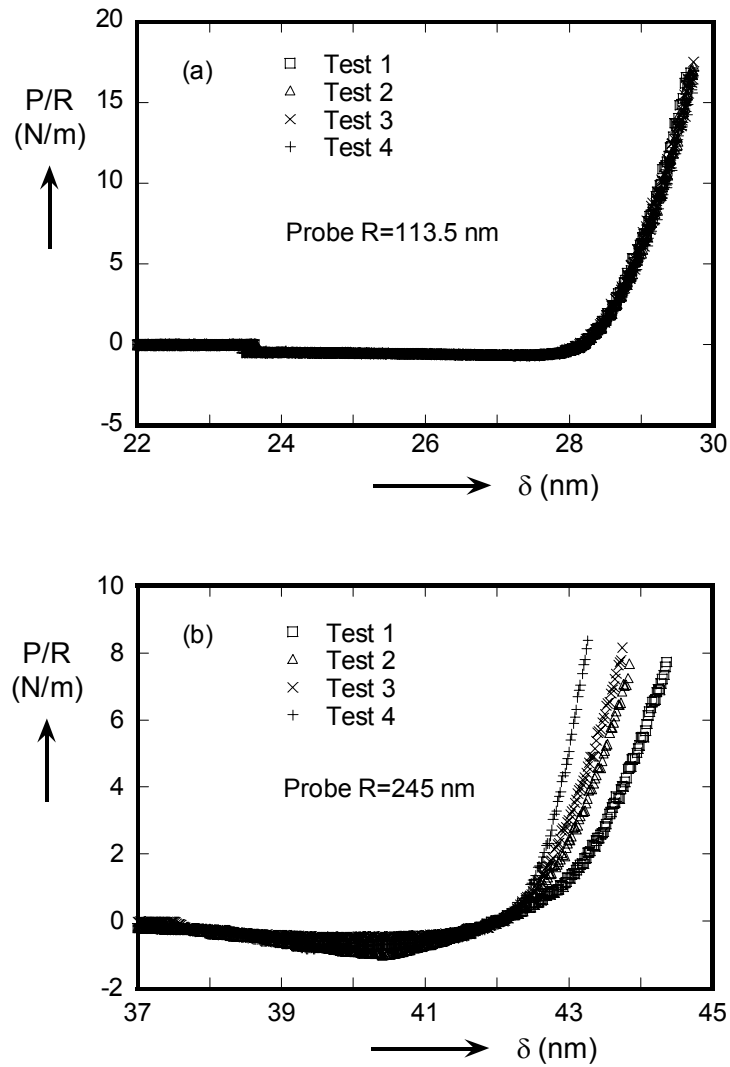


Figure 3.16 Force profiles that were taken on OTS-covered Si(100) surfaces prepared under: (a) anhydrous and (b) non-anhydrous conditions. Each of the panels superimposes four separate force versus distance curves measured at different points separated by between 10 and 20 μm .

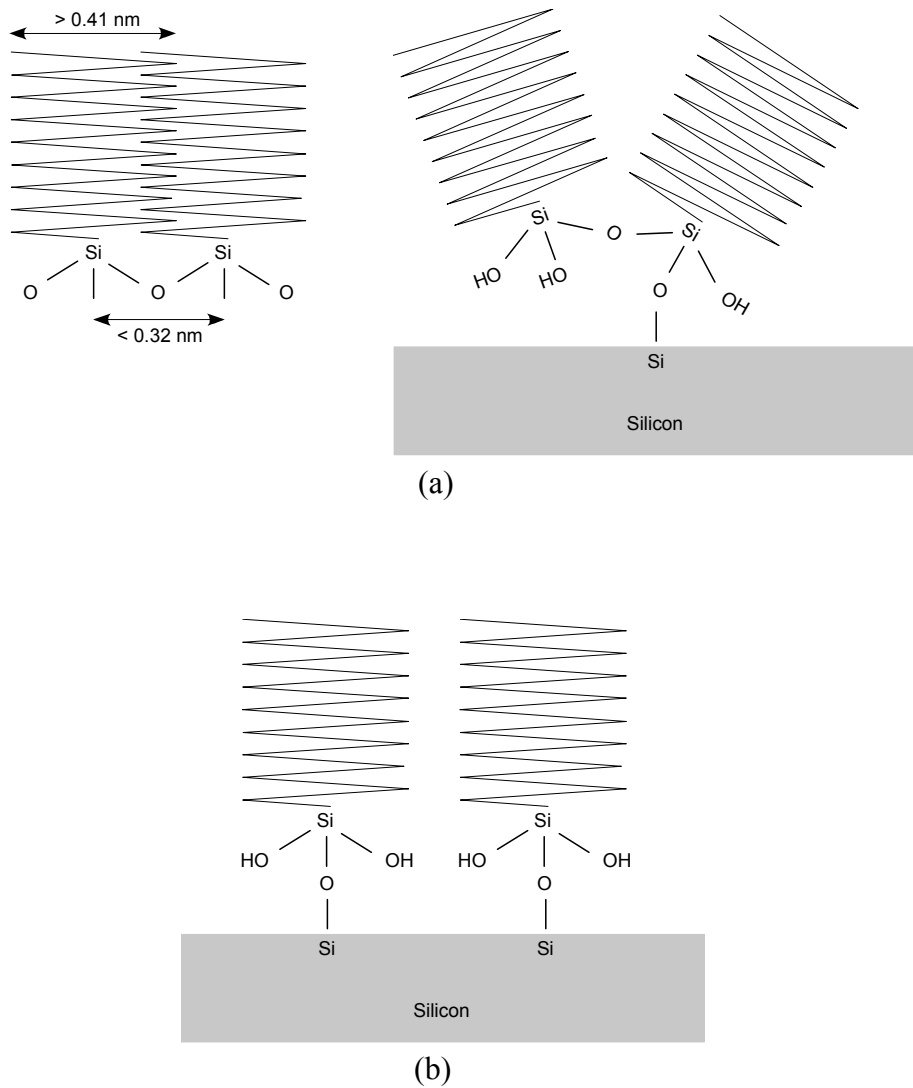


Figure 3.17 Schematic of structures of OTS moieties. (a) Cross-linked structure. Severe tilting is caused by sterically repulsive arrangement of two cross-linked OTS moieties covalently bonded through an Si-O-Si linkage to a silicon surface. (b) Densely packed OTS monolayer without cross-linking.

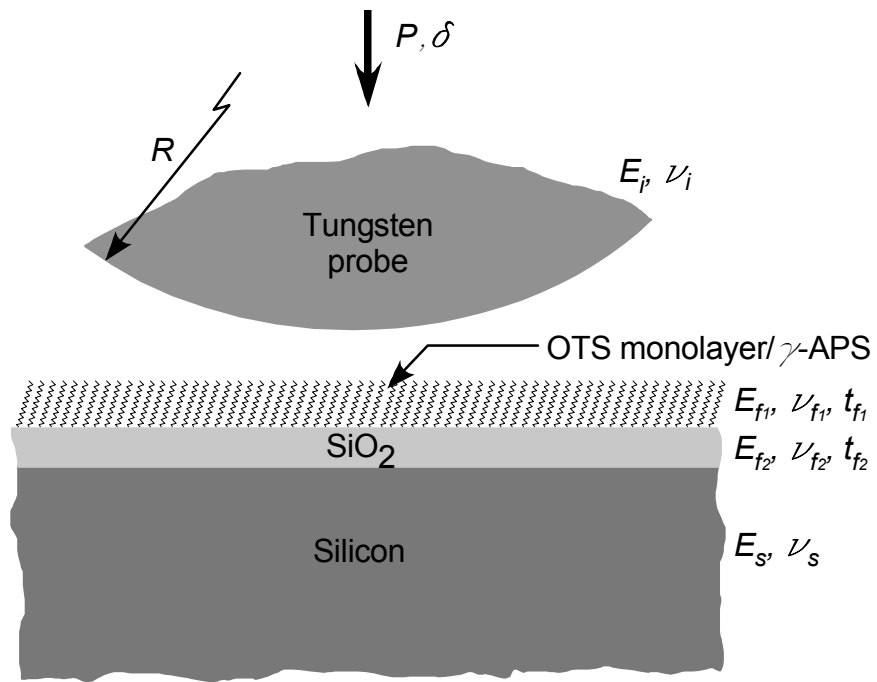


Figure 4.1 Schematic of IFM nanoindentation on layered materials.

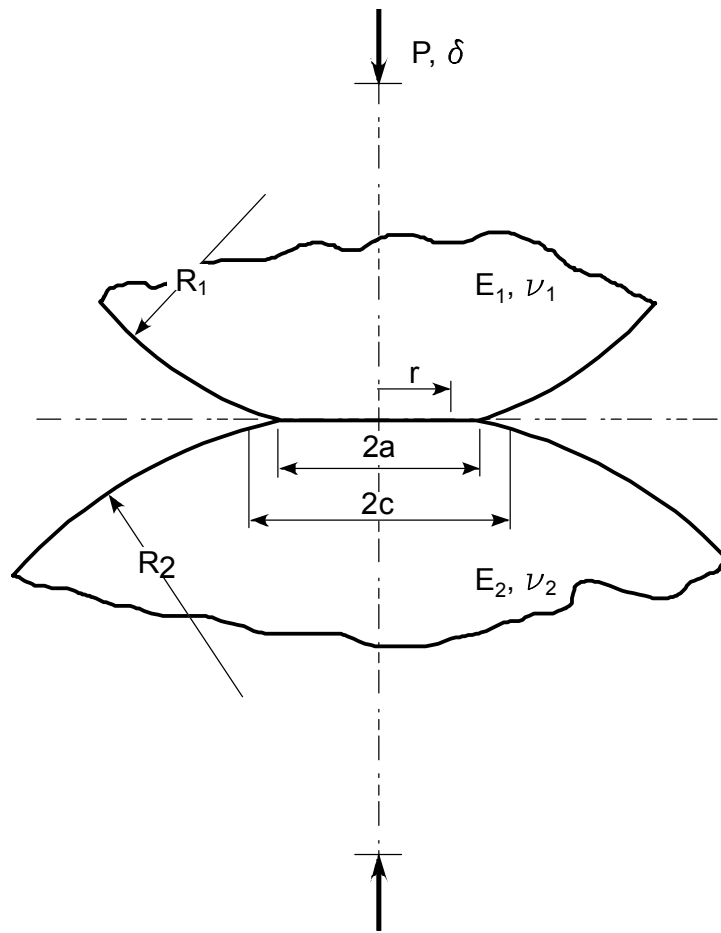


Figure 4.2 Contact between two deformable spheres. $R_2 = \infty$ corresponds to the contact between a sphere and a half space.

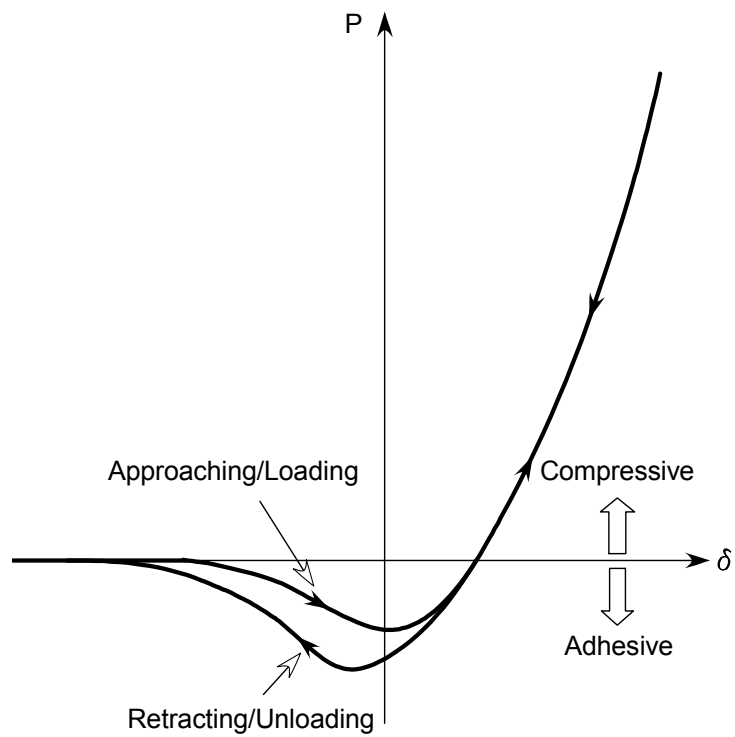


Figure 4.3 Typical force profiles of elastic contact between two deformable spheres.

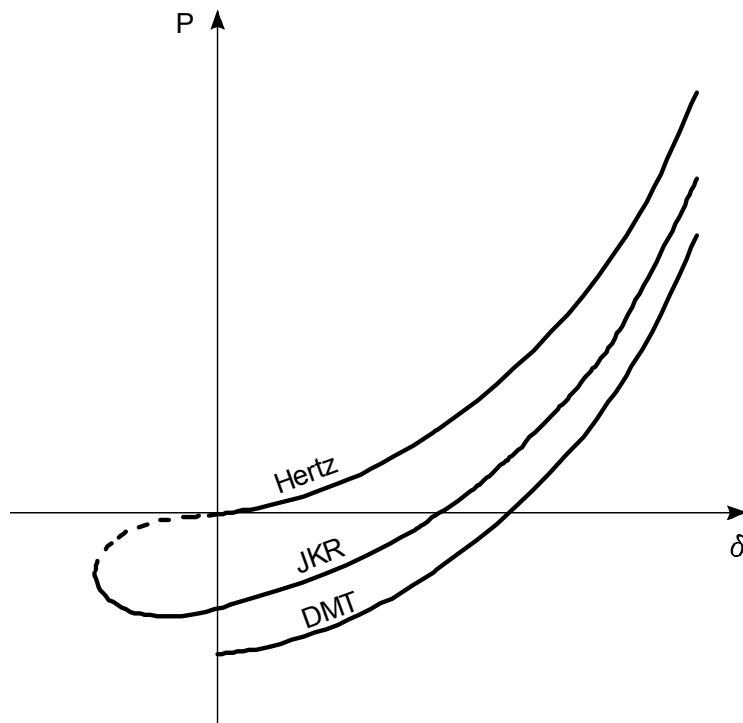


Figure 4.4 Force profiles produced by three contact mechanics theories. The differences are due to the different types of adhesive interactions that were invoked in the analyses.

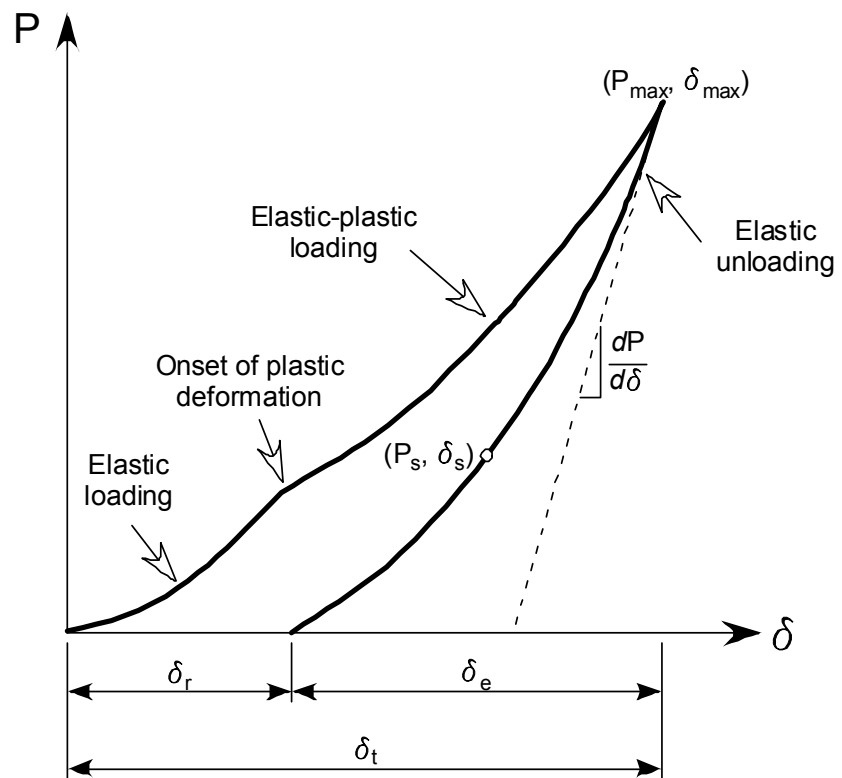


Figure 4.5 Indentation involving plastic deformations showing a kink on the loading path and hysteresis between the loading and unloading paths.

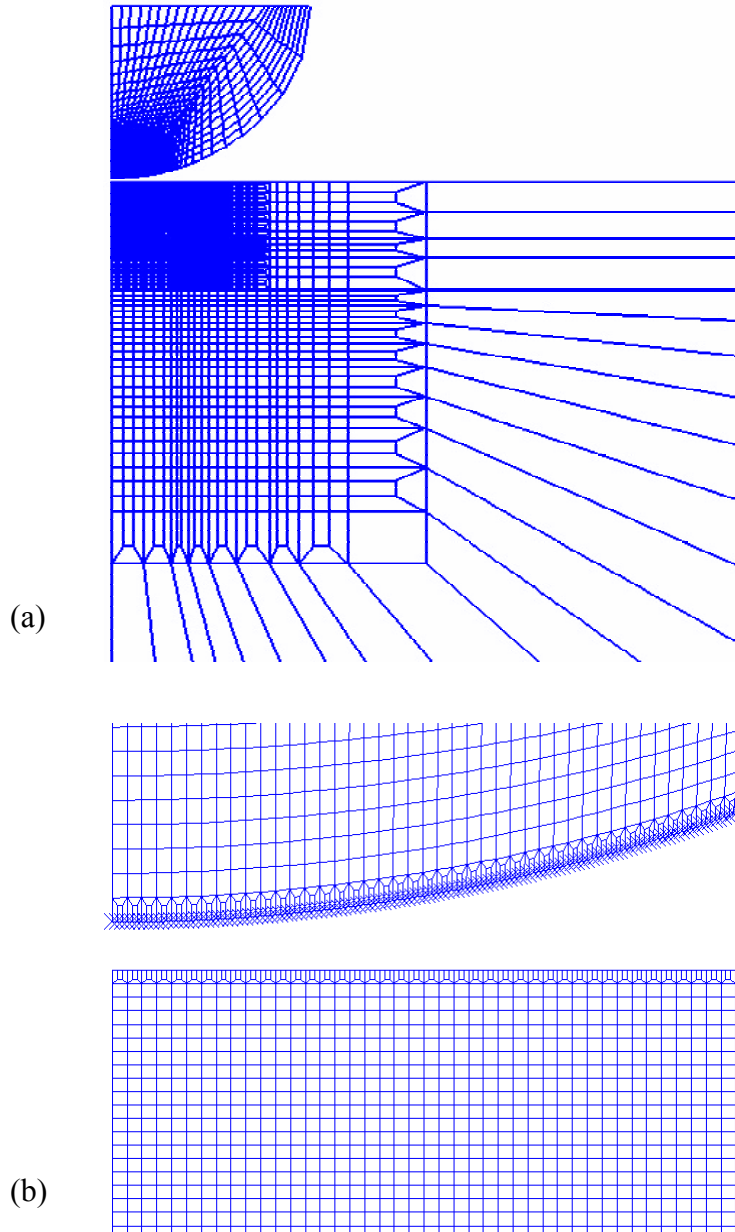


Figure 4.6 Finite element mesh for contact analysis: (a) overall and (b) magnified view of the mesh close to the contact region.

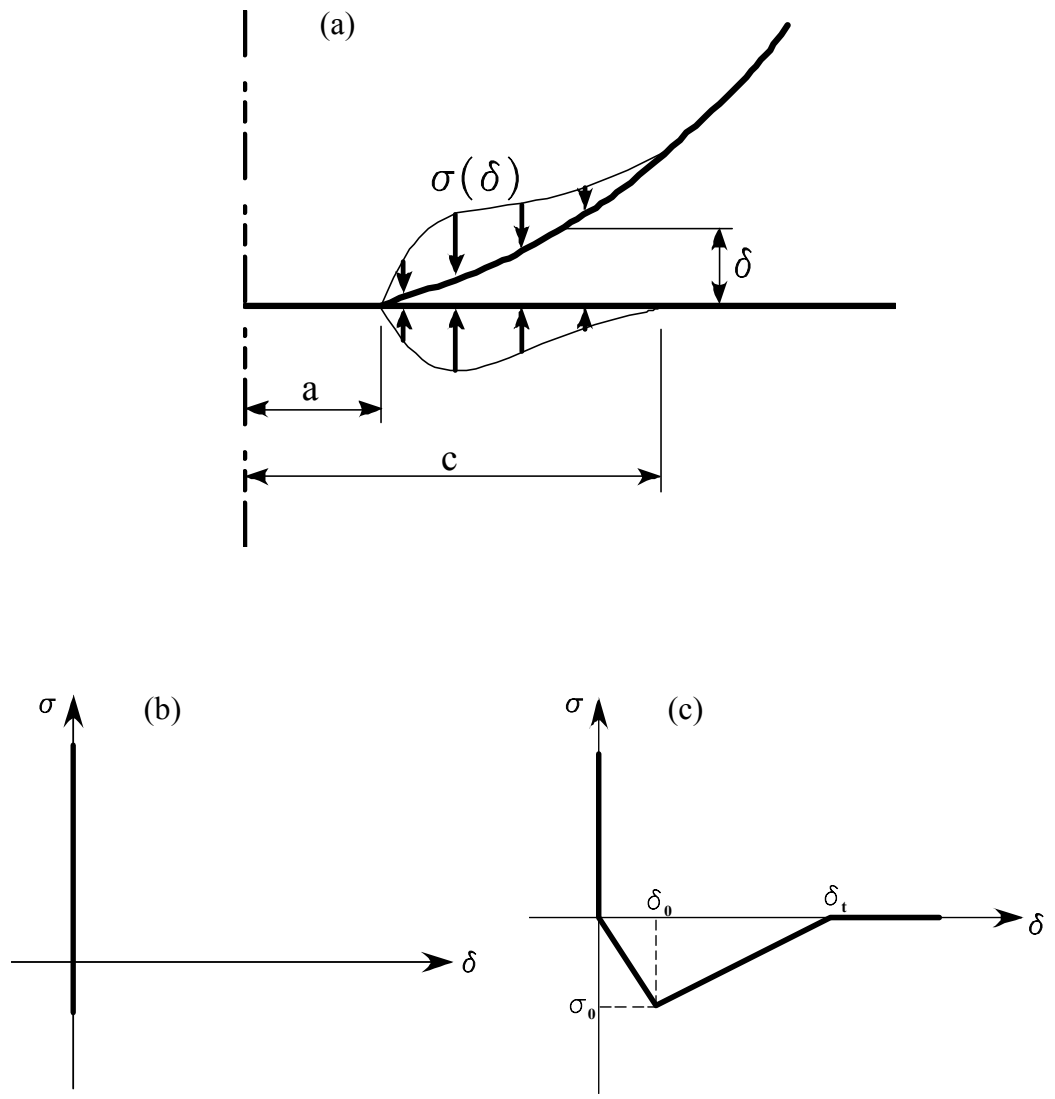


Figure 4.7 (a) Cohesive zone model with normal adhesive interactions, (b) default ABAQUS force-separation relationship for contact surfaces and (c) user-defined triangular force-separation law.

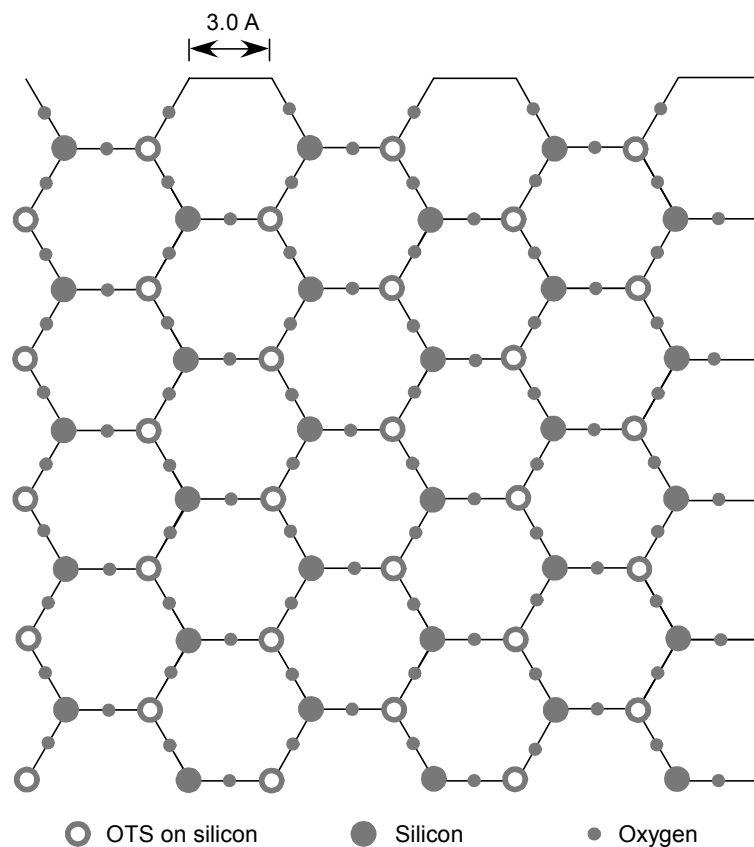


Figure 4.8 Plan view of the unit cell for the molecular dynamics simulation model of OTS on silica. Small solid circles represent oxygen atoms, large solid circles represent silicon atoms on a lower plane and the remaining open circles represent the silicon atoms with OTS molecules on them.

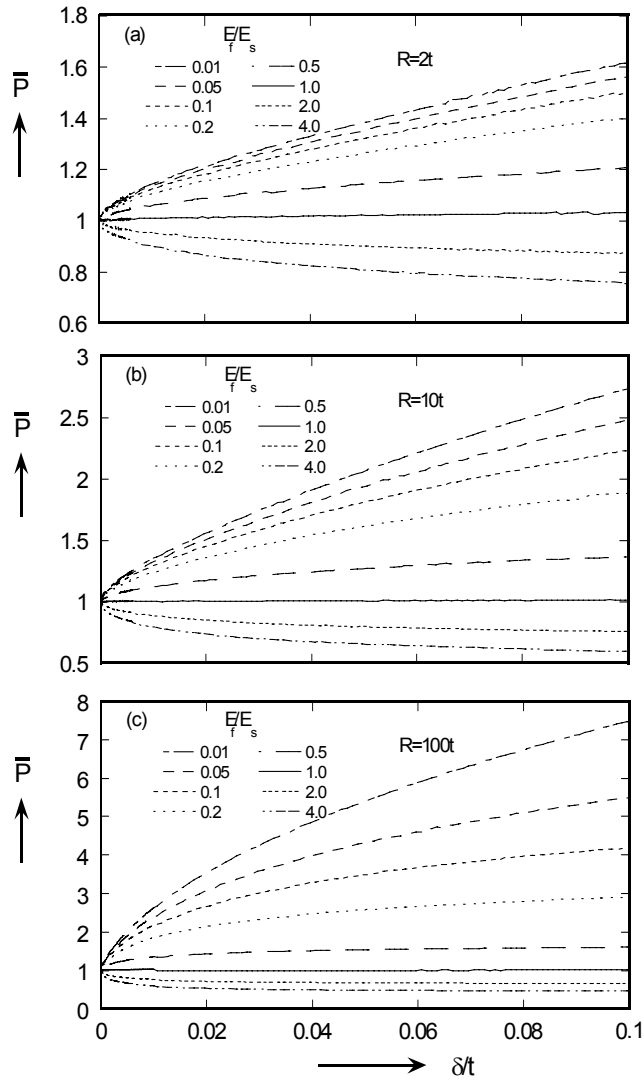


Figure 5.1 Parametric study of substrate effect: normalized indentation force vs. indentation depth for various film modulus for different probe sizes ($E_s=100$ GPa, $\nu_s = \nu_f = 0.2$, $t=50$ nm).

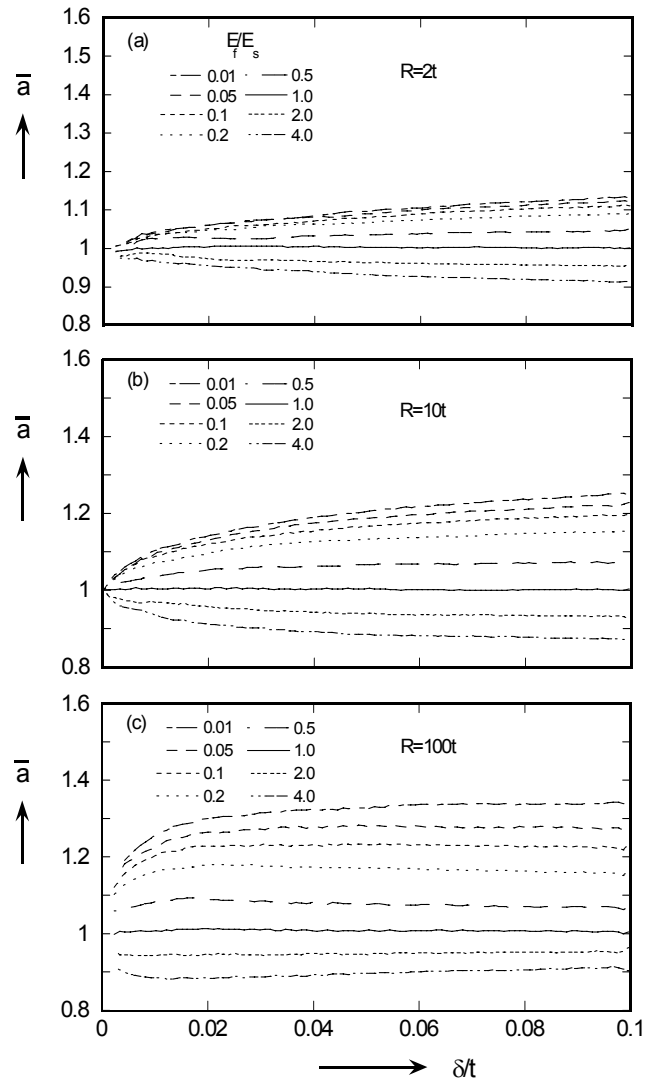


Figure 5.2 Parametric study of substrate effect: normalized contact radius vs. indentation depth for different probe size ($E_s = 100$ GPa, $\nu_s = \nu_f = 0.2$, $t = 50$ nm).

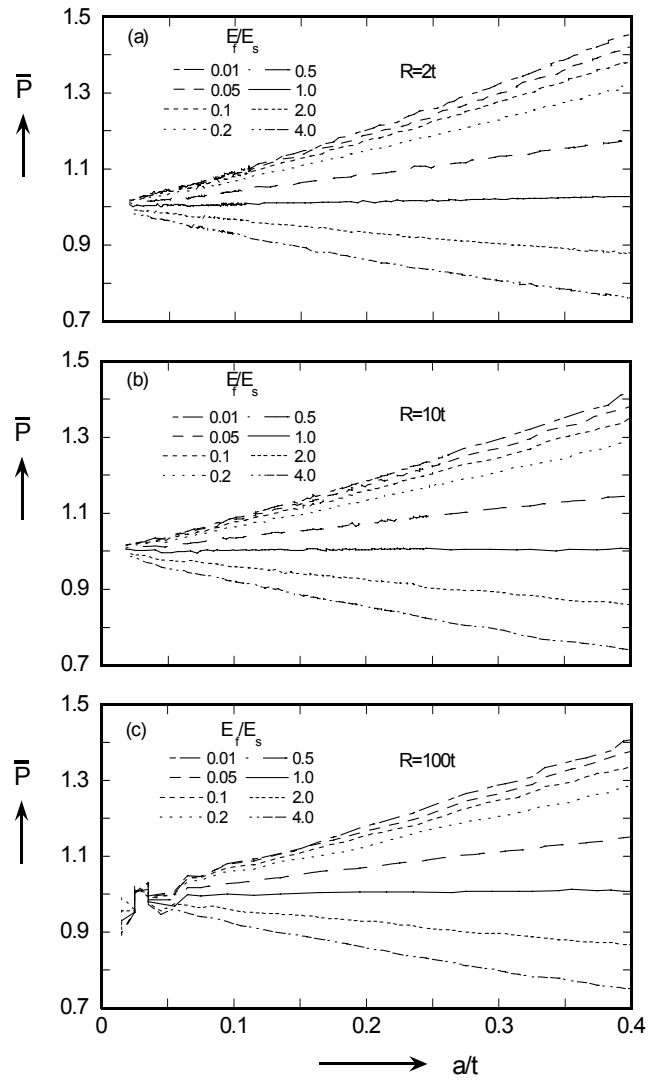


Figure 5.3 Parametric study of substrate effect: normalized indentation force vs. contact radius for various film modulus for different probe size ($E_s=100$ GPa, $\nu_s = \nu_f = 0.2$, $t=50$ nm).

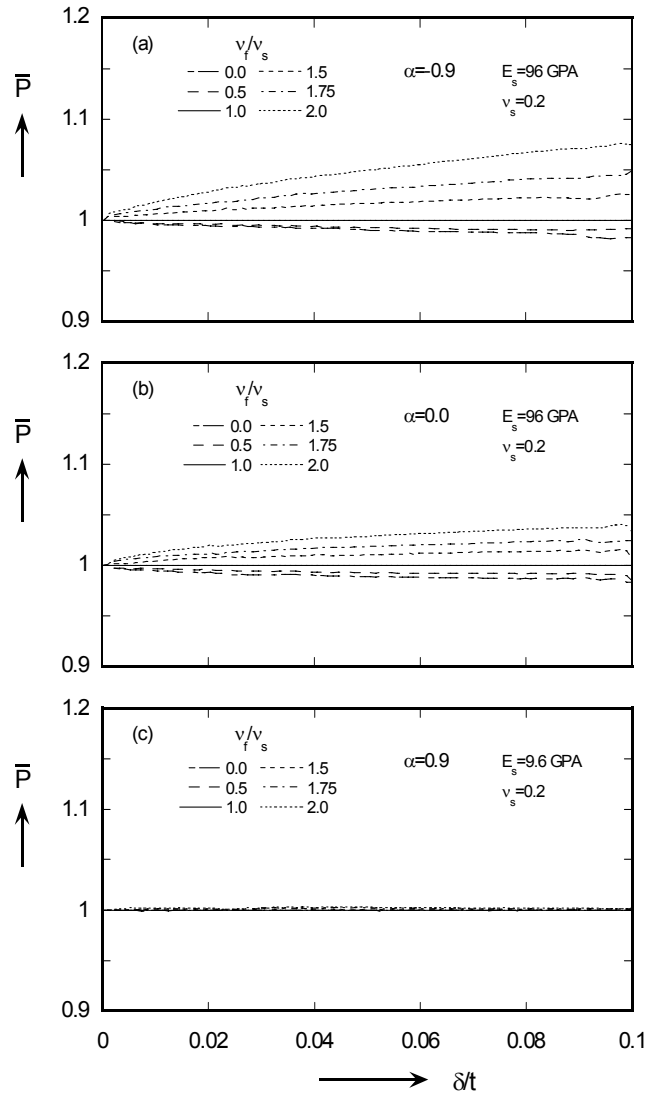


Figure 5.4 Parametric study of Poisson's ratio effect for $R=2t$ ($t=50$ nm).

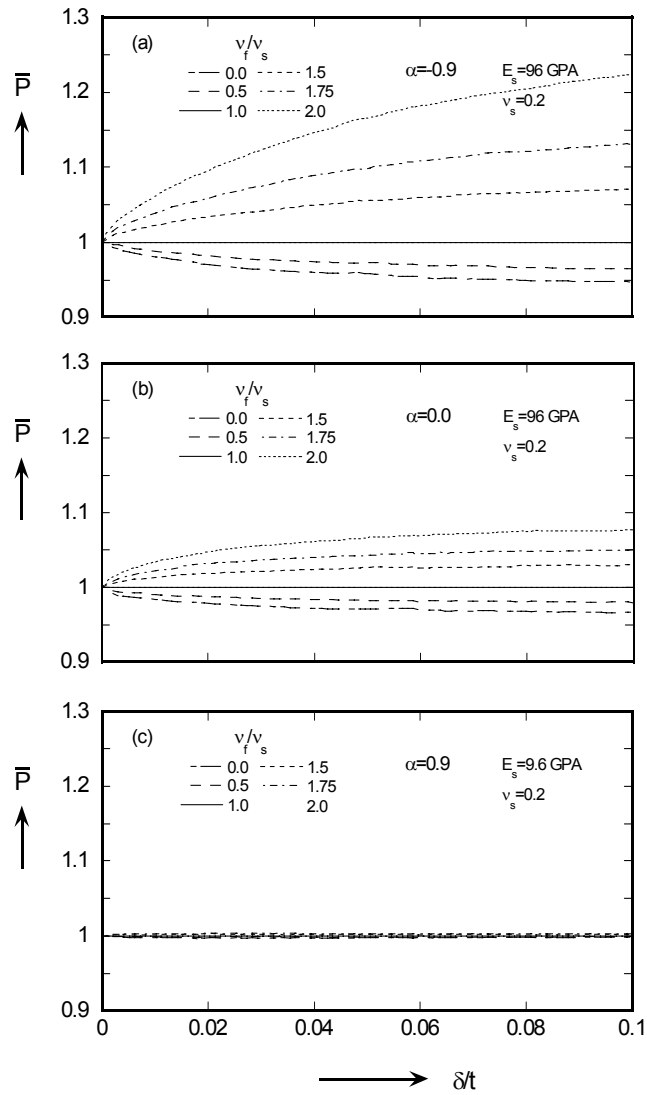


Figure 5.5 Parametric study of Poisson's ratio effect for $R=10t$ ($t=50 \text{ nm}$).

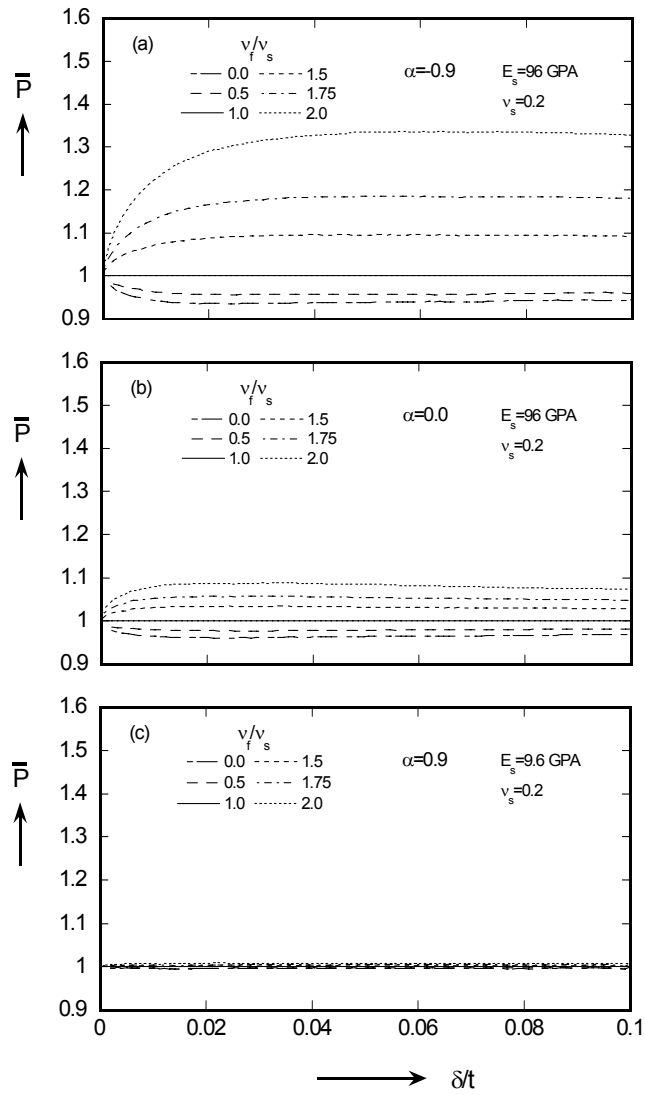


Figure 5.6 Parametric study of Poisson's ratio effect for $R=100t$ ($t=50$ nm).

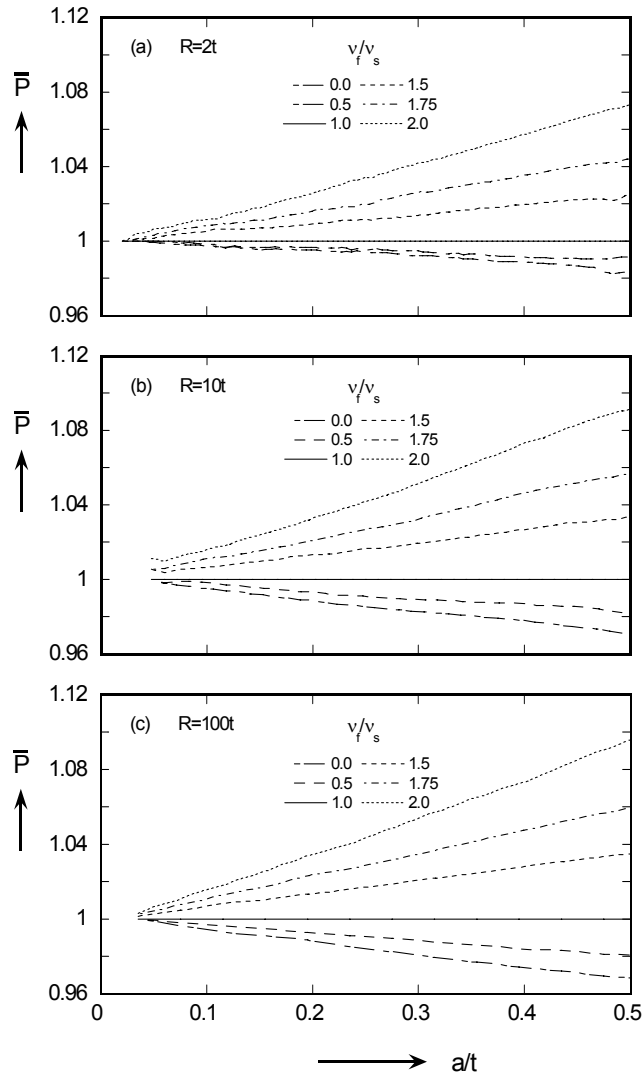


Figure 5.7 Parametric study of Poisson's ratio effect for different probe size ($\alpha = -0.9$).

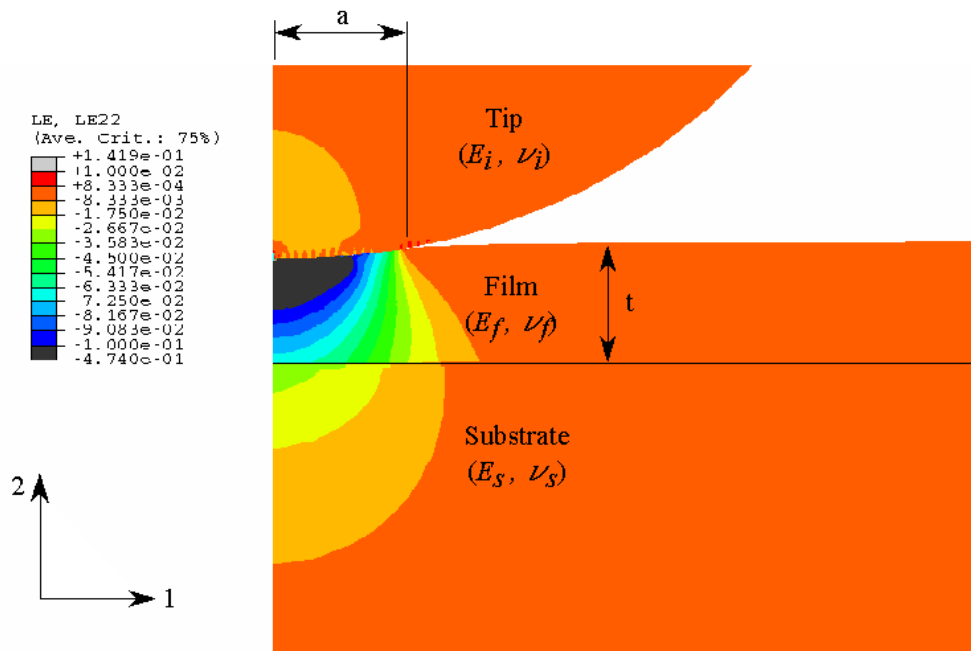


Figure 5.8 ϵ_{22} strain contour for a tungsten indenter on a single film on a substrate ($E_s=96$ GPa, $\nu_s=0.2$).

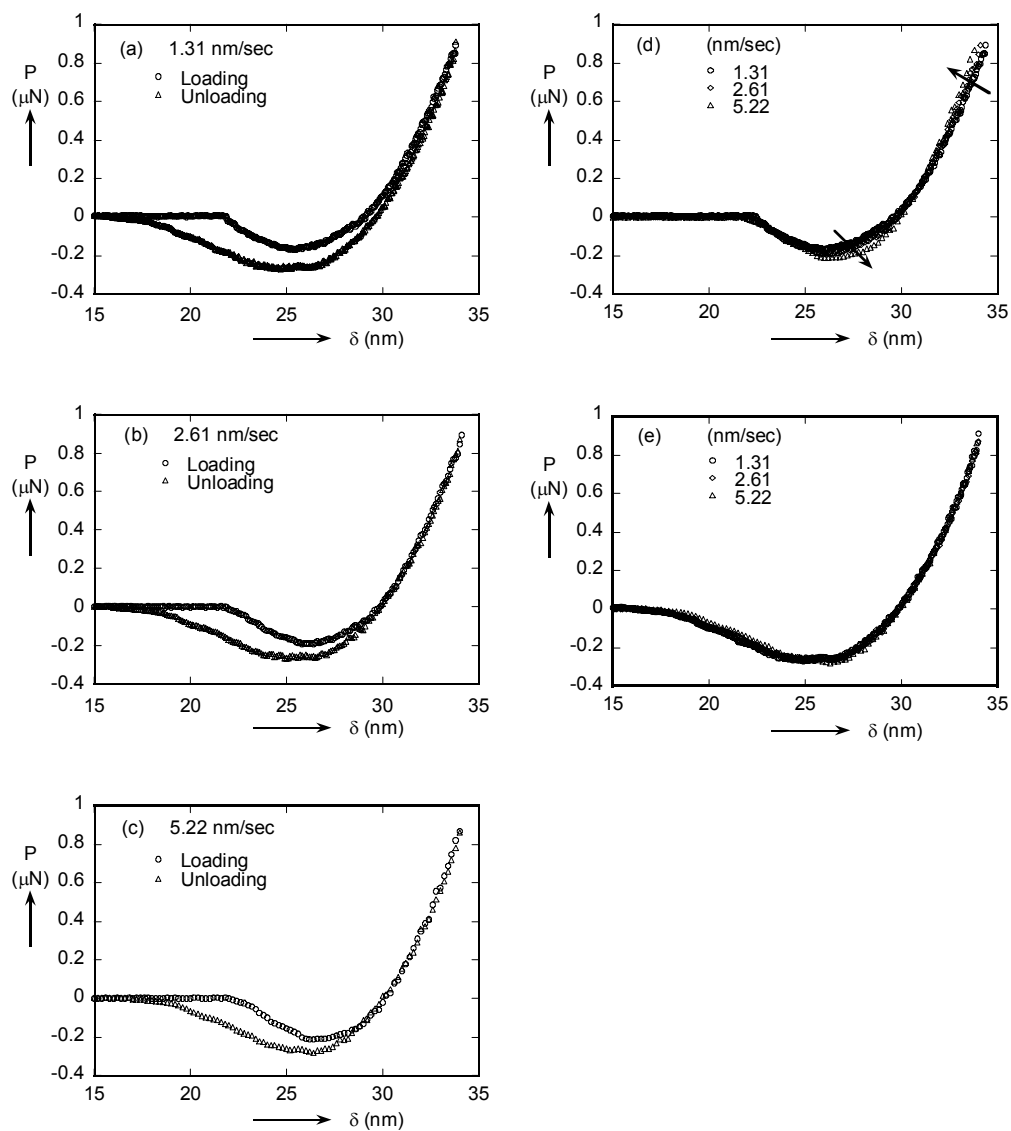


Figure 5.9 The rate effect for loading and unloading on an ambient cured 46 nm γ -APS film on silicon.

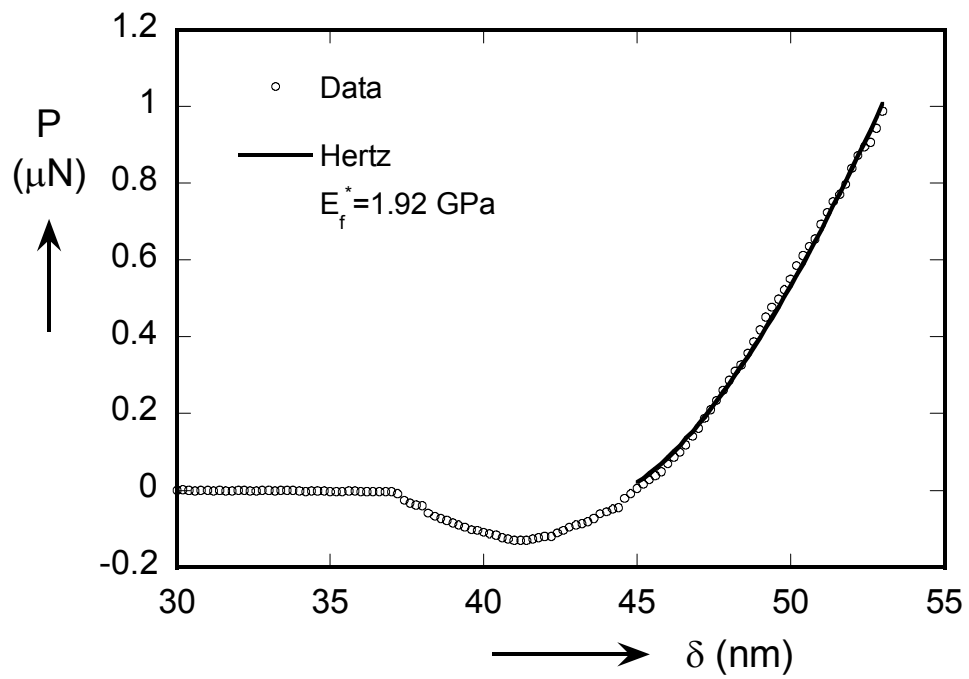


Figure 5.10 Hertz theory fit of a force profile from a 4 μm thick γ -APS film on silicon.

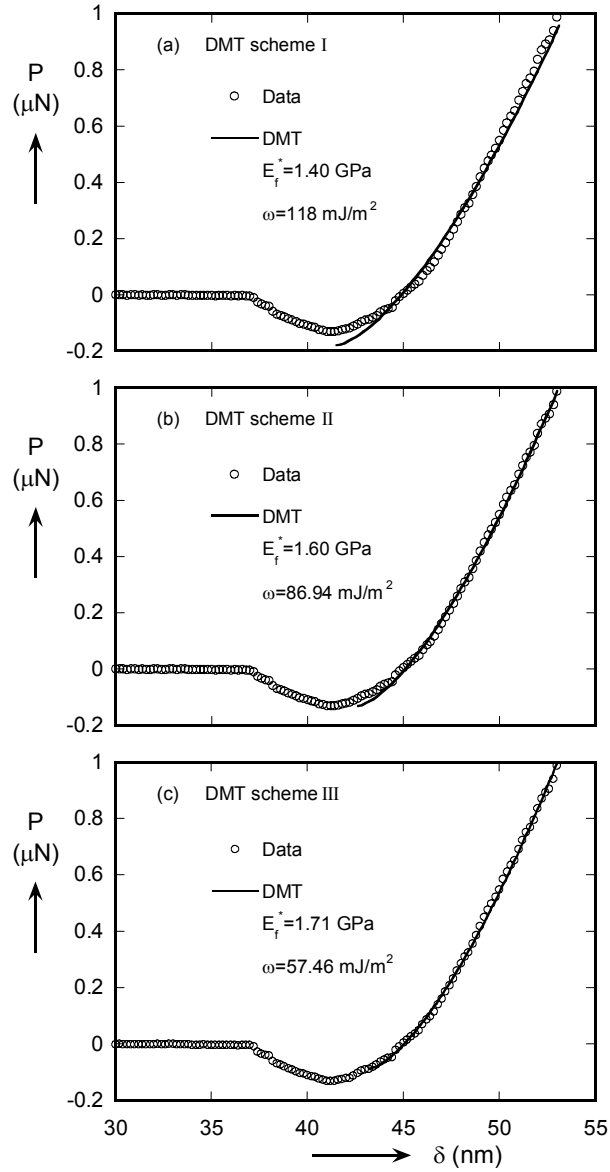


Figure 5.11 DMT theory fit of a force profile from a 4 μm thick γ -APS film on silicon: (a) a two-parameter fit Scheme I, (b) a two-parameter fit Scheme II and (c) a three-parameter fit Scheme III.

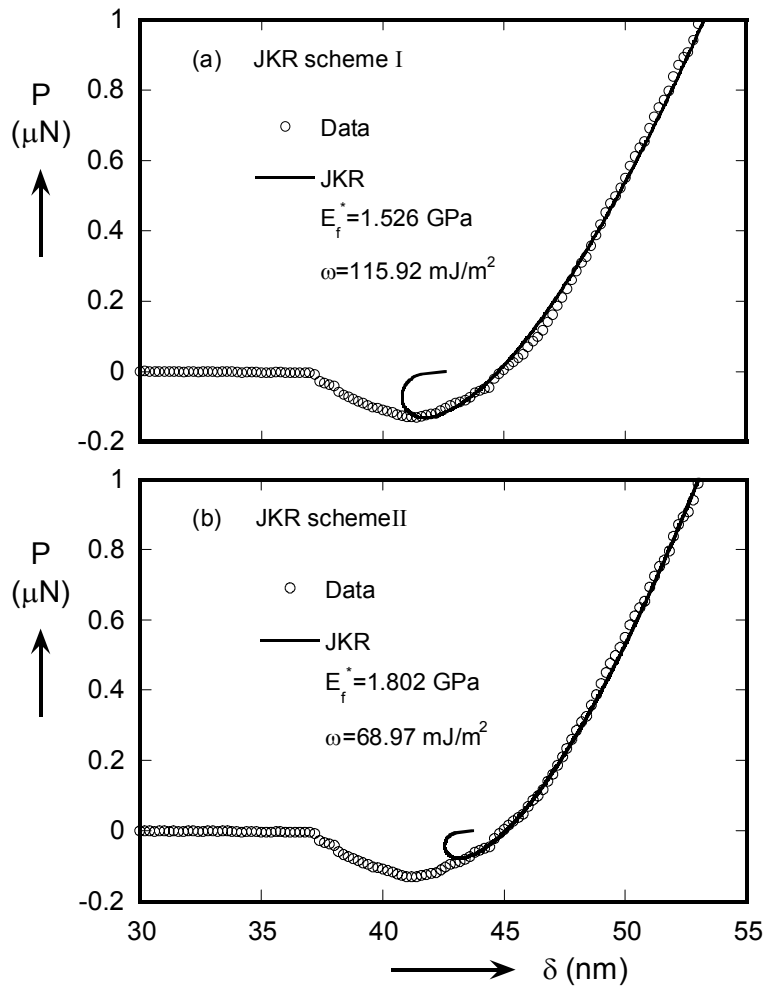


Figure 5.12 JKR theory fit of a force profile from a 4 μm thick γ -APS film on silicon: (a) two parameter fit, and (b) three parameter fit.

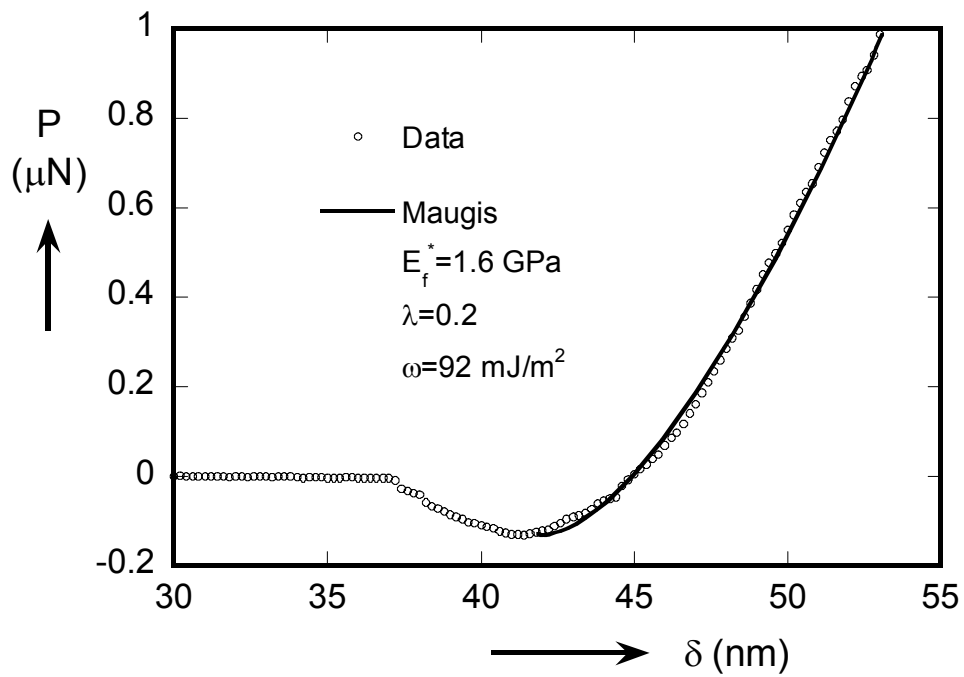


Figure 5.13 Maugis theory fit of a force profile from a 4 μm thick γ -APS film on silicon.

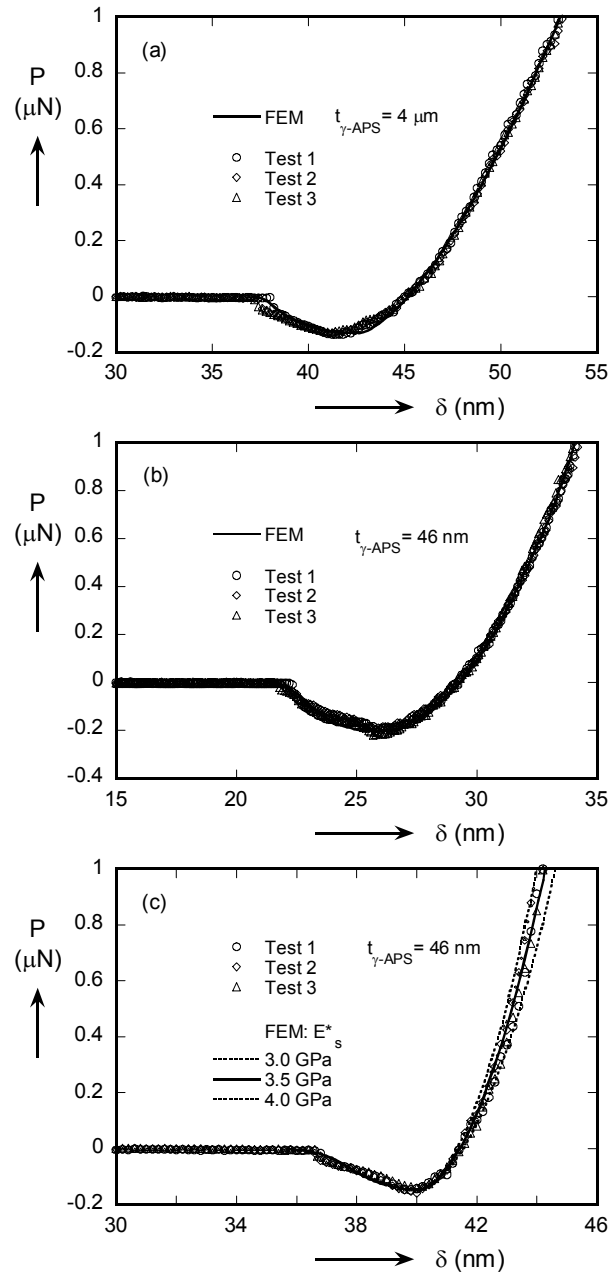


Figure 5.14 Finite element simulation of force profiles from: (a) a 4 μm thick γ -APS film on silicon, (b) an ambient cured, 46 nm thick γ -APS film on silicon and (c) a 100 $^{\circ}\text{C}$ cured, 46 nm thick γ -APS film on silicon.

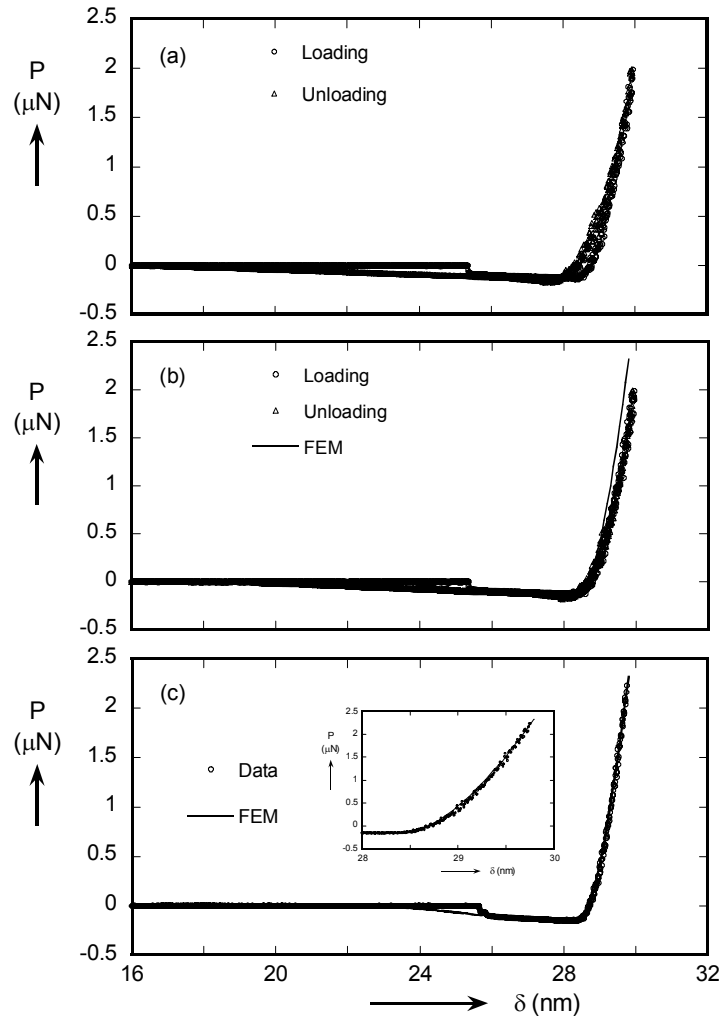


Figure 5.15 A typical IFM force profile of bare silicon at the loading speed of 0.26 nm/sec: (a) original profile showing hysteresis of piezo elements at slow loading/unloading speed, (b) force profile after the adjusting the hysteresis, and (c) data is compared with finite element analysis using the known properties of silicon and silica.

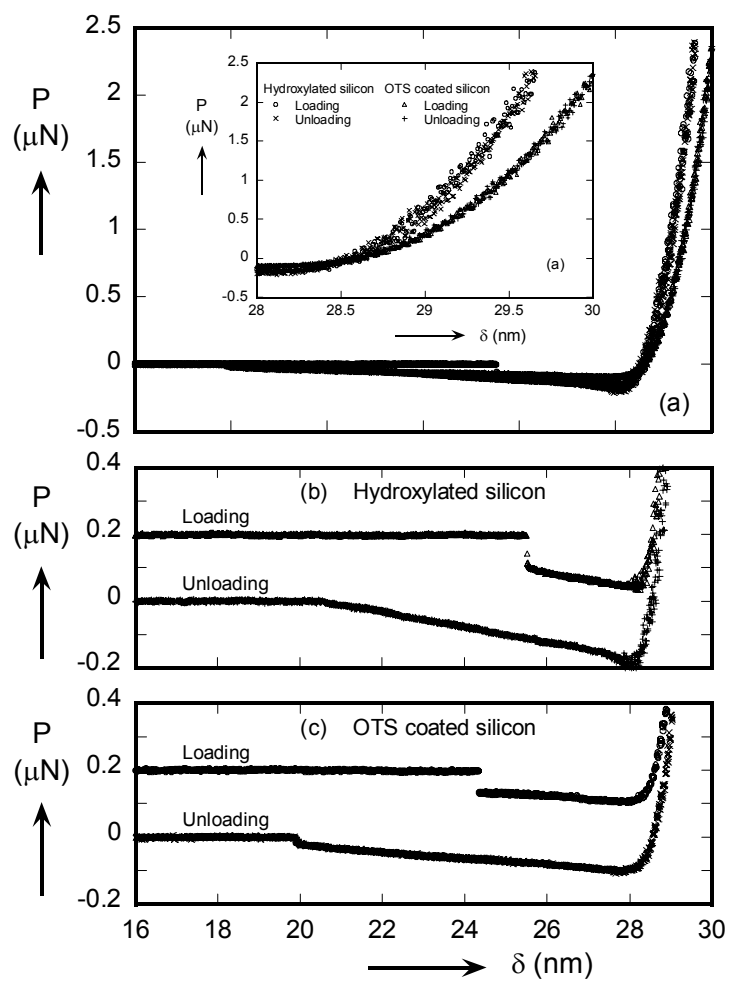


Figure 5.16 A comparison of force profiles of bare silicon and silicon coated with an OTS monolayer. The loading paths in (b) and (c) have been shifted upward for clarification.

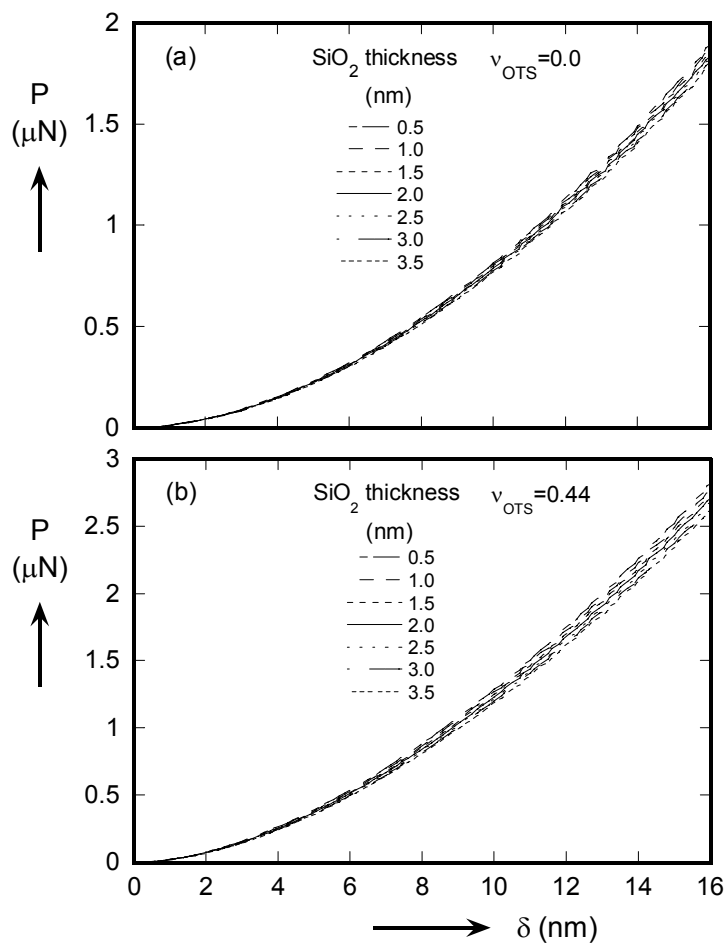


Figure 5.17 Parametric study of the effect of the thickness of the oxide layer on force profiles: (a) $v_{\text{OTS}} = 0.0$ and (b) $v_{\text{OTS}} = 0.44$.

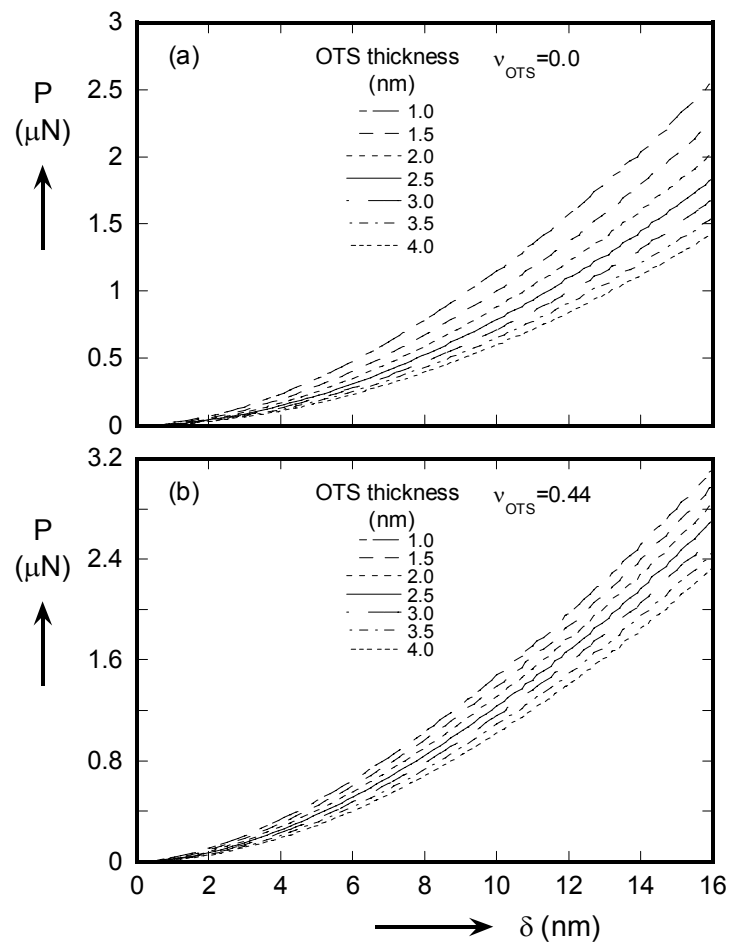


Figure 5.18 Parametric study of the effect of the thickness of the OTS monolayer on force profiles: (a) $\nu_{\text{OTS}}=0.0$ and (b) $\nu_{\text{OTS}}=0.44$.

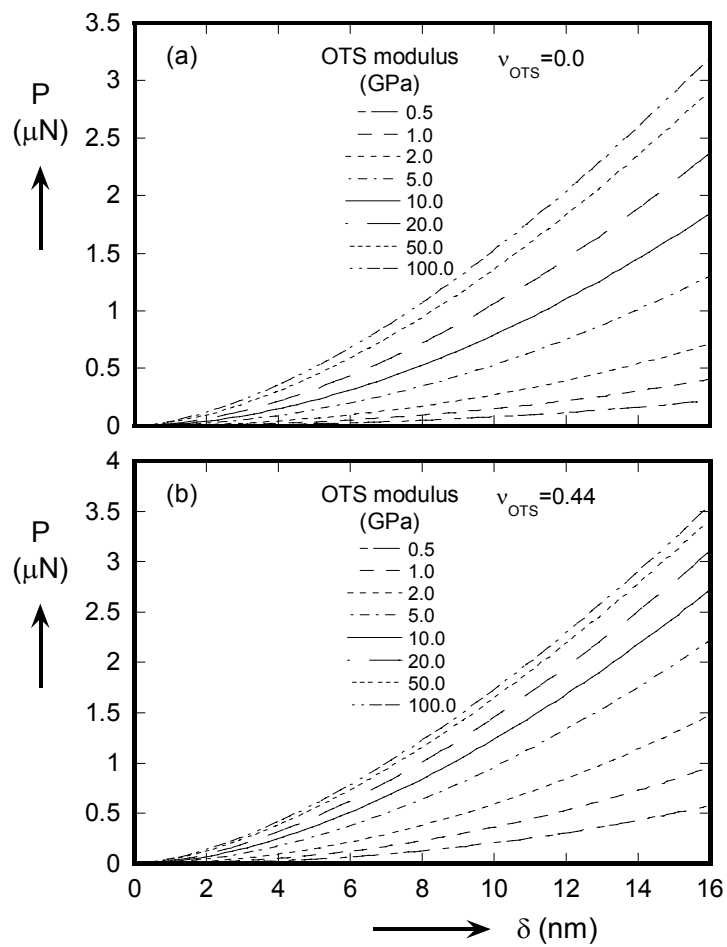


Figure 5.19 Parametric study of the effect of the OTS modulus on force profiles: (a) $\nu_{\text{OTS}} = 0.0$ and (b) $\nu_{\text{OTS}} = 0.44$.

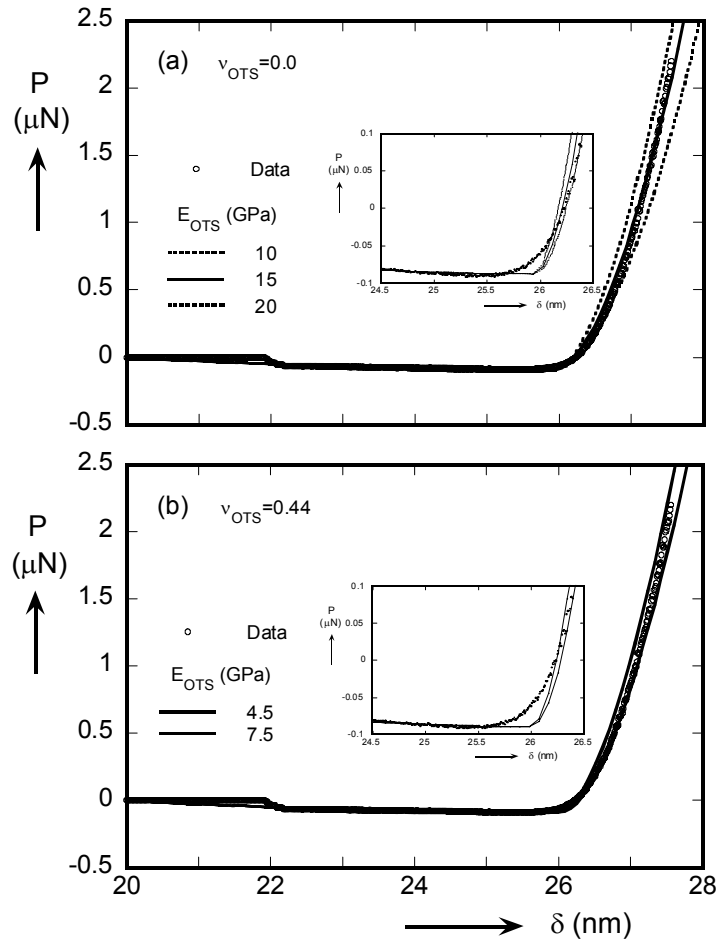


Figure 5.20 A comparison of measured and predicted IFM force profile on OTS: (a) $\nu_{\text{OTS}} = 0.0$ and (b) $\nu_{\text{OTS}} = 0.44$. The insets emphasize the disagreement at low force levels.

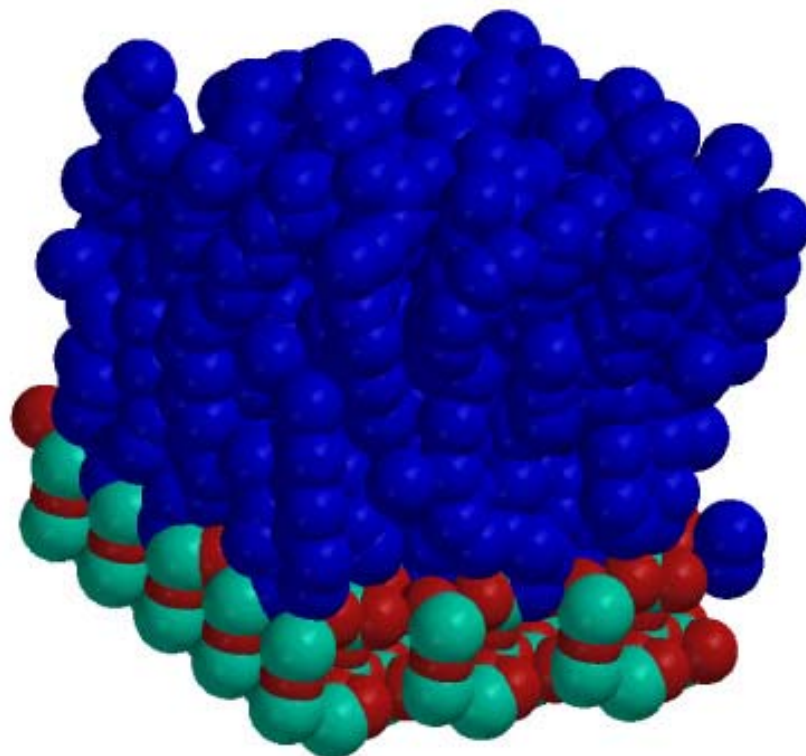


Figure 5.21 Self-assembly of OTS from the molecular dynamics simulation.
Blue=CH₂ and CH₃ united atoms, red=oxygen, turquoise=silicon.

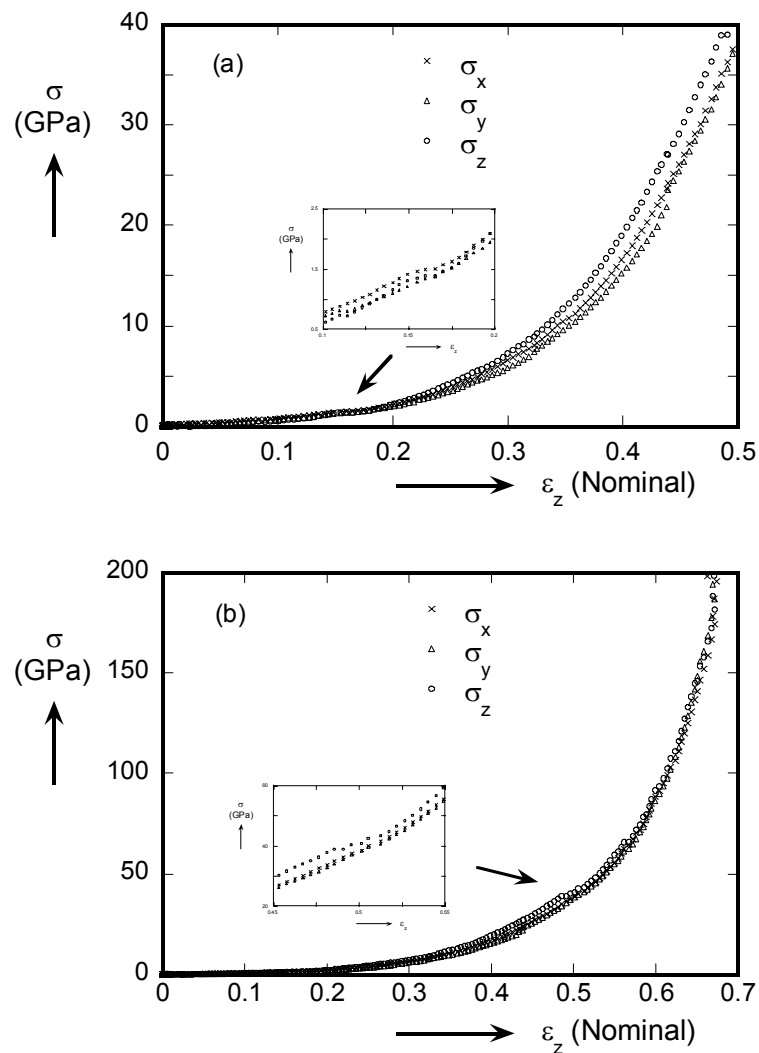


Figure 5.22 The stresses in an infinite OTS monolayer under uniform compression by molecular dynamics simulation. The insets emphasize kinks in the response that are probably due to conformational changes.

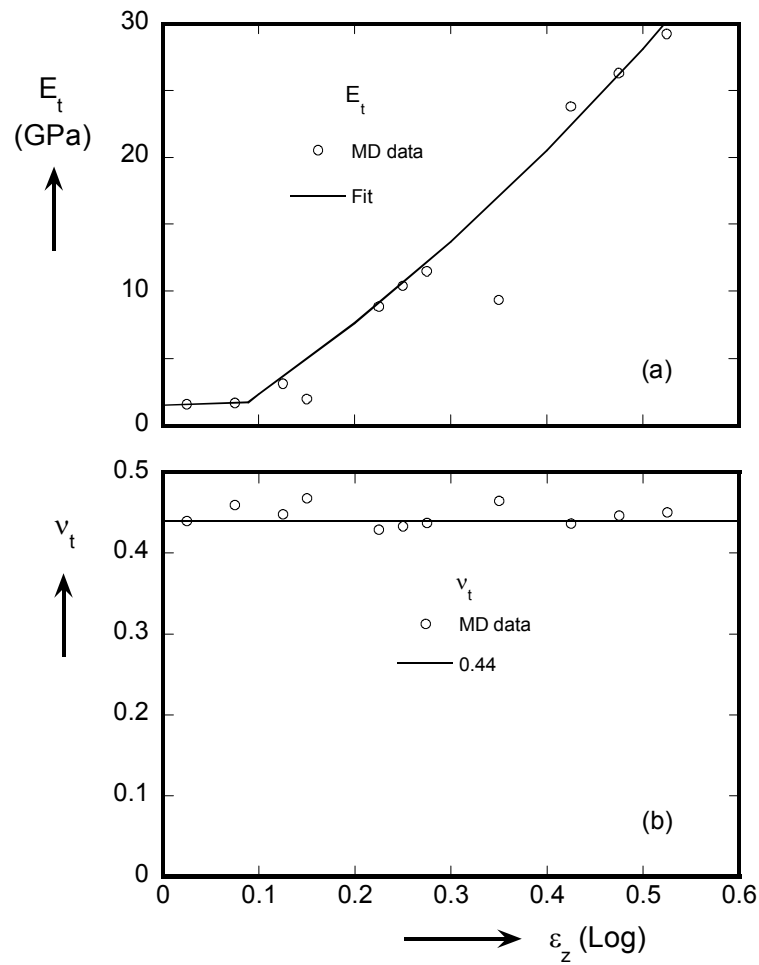


Figure 5.23 The extracted (a) tangent modulus and (b) Poisson's ratio for a hypoelastic material based on the response obtained from the molecular dynamics analysis.

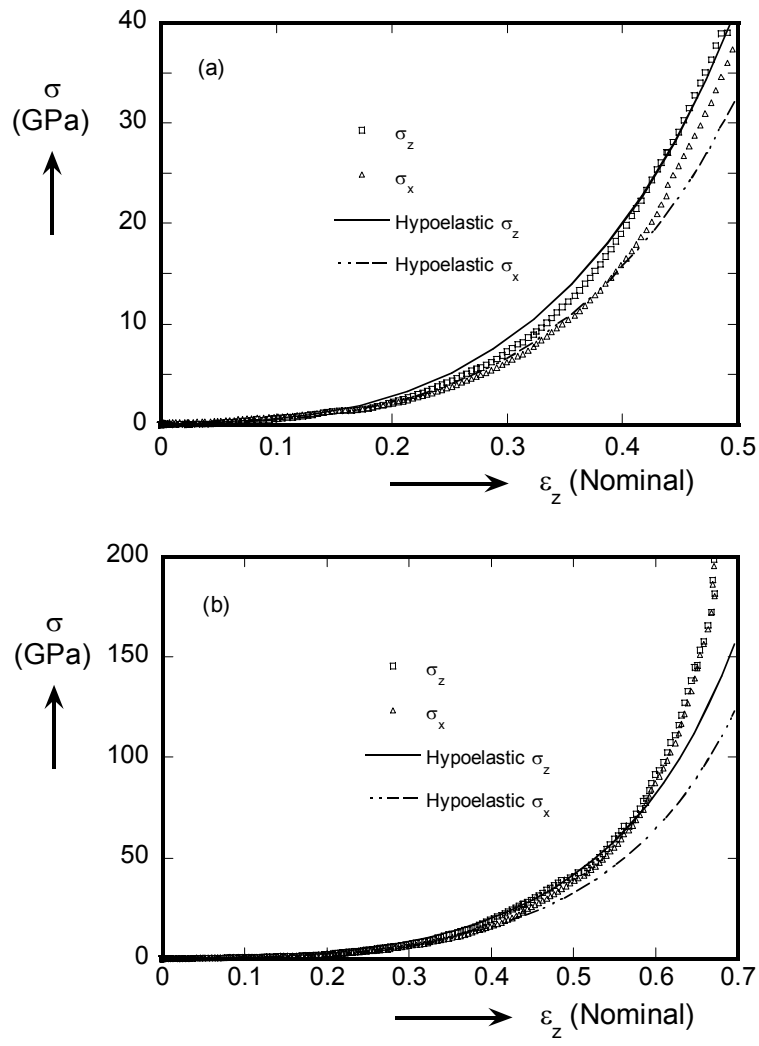


Figure 5.24. Comparison of the stress-strain behavior of OTS from the molecular dynamics simulation and hypo-elastic model: (a) the comparison at low strain levels and (b) complete range.

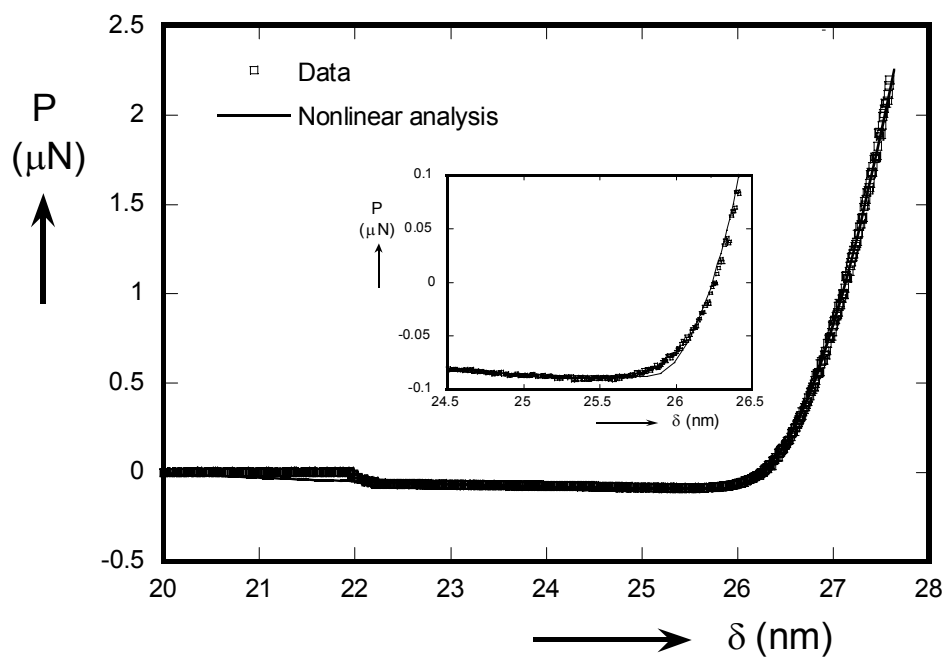


Figure 5.25 Non-linear finite element analysis of the IFM experiment on OTS. The inset emphasizes the improved agreement at low force levels.

Bibliography

- ABAQUS/*Standard User's Manual*. Habbit, Karlsson & Sorensen, Inc.
- Allen, M. P. and Tildesley, D. J., 2002. *Computer Simulations of Liquids*. Clarendon Press, Oxford.
- Angst, D. L., and Simmons, G. W., 1991. Moisture adsorption characteristics of organosiloxane self-assembled monolayers. *Langmuir* 7, 2236-2242.
- Azarian, M. H., and Bauer, C. L., 1993. Tribology of thin-film media in both flying and sliding modes. *Wear* 168, 59-76.
- Bain, C. D., Eval, J., and Whitesides, G. M., 1989. Formation of monolayers by coadsorption of thiol on gold: variation in head group, tail group, and solvent. *Journal of the American Chemical Society* 111, 7155-7164.
- Bhattacharya, A. K., and Nix, W. D., 1988. Analysis of elastic and plastic deformation associated with indentation testing of thin films on substrates. *International Journal of Solids and Structures* 24, 1287-1298.
- Bhushan, B., 1999 (a). *Handbook of Micro/Nano Tribology*. 2nd Ed., CRC Press.
- Bhushan, B., 1999 (b). *Principles and Applications of Tribology*, John Wiley and Sons, Inc, New York.
- Bining, G., Quate, C. F., and Gerber, Ch., 1986. Atomic Force Microscope. *Physical Review Letters* 56(9), 930-933.
- Britcher, L. G., Kehoe, D. C., Matisons, J. G., Smart, R. St. C., and Swincerpp A. G., 1993. Silicones on glass surfaces. 2. Coupling agent analogs. *Langmuir* 9, 1609 – 1613.
- Bunker, B. C., Carpick, R. W., Assink, R. A., Thomas, M. L., Hankins, M. G., Voigt, J. Sipola, A., D., de Boer, M. P., and Gulley, G. L., 2000. The Impact of solution agglomeration on the deposition of self-assembled monolayers. *Langmuir* 16, 7742-7751.
- Burns, A. R., Houston, J. E., Carpick, R. W., and Michalske, T. A., 1999 (a). Friction and molecular deformation in the tensile regime. *Physical Review Letters* 82(6), 1181-1184.

- Burns, A. R., Houston, J. E., Carpick, R. W., and Michalske, T. A., 1999 (b). Molecular level friction as revealed with a novel scanning probe. *Langmuir*, 15(8), 2922-2930.
- Bückle, H., 1971. in *Science of Hardness Testing and Its Research Applications*, edited by Westbrook, J. H., and Conrad, H., American Society for Metals, Metals Park, OH, pp453-494.
- Cabibil, H. L., Pham, V., Lozano, J., Celio, H., Winter, R. M., and White, J. M., 2000. Self-organized fibrous nanostructures on poly[(aminopropyl)siloxane] films studied by atomic force microscopy. *Langmuir* 16, 10471-10481.
- Cabibil, H., Celio, H., Lozano, J., White, J. M., and R. M., Winter, 2001. Nanomechanical properties of polysiloxane-oxide interphases measured by interfacial force microscopy. *Langmuir* 17, 2160-2166.
- Cappella, B., and Dietler, G., 1999. Force-distance curves by atomic force microscopy. *Surface Science Reports* 34, 1-104.
- Carpick, R. W., and Salmeron, M., 1997. Scratching the surface: fundamental investigations of tribology with atomic force microscopy. *Chemical Reviews* 97, 1163-1194.
- Celio, H., 2003. Private communication.
- Chaki, N. K., and Vijayamohanan, K., 2002. Self-assembled monolayers as a tunable platform for biosensor applications. *Biosensors & Bioelectronics* 17, 1-12.
- Chen, W. T., and Engel, P. A., 1972. Impact and contact stress analysis in multilayer media. *International Journal of Solids and Structures* 8, 1257-1281.
- Chouchaoui, C. S.; Benzeggagh, M. L., 1997. The effect of interphase on the elastic behavior of a glass/epoxy bundle. *Composites Science and Technology* 57, 617-622.
- Cossins, S., Connell, M., Cross, W., Winter, R., and Kellar, J., 1996. In-situ near-IR cure monitoring of a model epoxy matrix composite. *Applied Spectroscopy* 50, 900-905.

- Culler, S. R., Ishida, H., and Koenig, J. L., 1983. The use of infrared methods to study polymer interfaces. *Annual Review of Materials Science* 13, 363-86.
- Derjaguin, B. V., Muller, V. M., and Toporov, Y. P., 1975. Effect of contact on the adhesion of particles. *Journal of Colloid and Interface Science* 53, 314-326.
- Doerner, M. F., and Nix, W. D., 1986. A method for interpreting the data from depth-sensing indentation instruments. *Journal of Materials Research* 1 (4), 601-609.
- Drzal, L.T., 1990. The role of the fiber/matrix interphase on composite interfaces. *Vacuum* 41, 1615-1618.
- Dunders, J., 1969. Edge-bonded dissimilar media. *Journal of Applied Mechanics* 36, 650-652.
- Field, J. S., and Swain, M. V., 1993. A simple predictive model for spherical indentation. *Journal of Materials Research* 8, 297-305.
- Fischer-Cripps, A. C., 2000. A review of analysis methods for sub-micro indentation testing. *Vacuum*, 58, 569-585.
- Frenkel, D. and Smit, B., 2002. *Understanding Molecular Simulation: From Algorithms to Applications*. 2nd Ed., Academic Press, Inc., San Diego.
- Garnier, M. G., de los Arcos, T., Boudaden, J., and Oelhafen, P., 2003. Photoemission study of the iron-induced chemical reduction of silicon native oxide. *Surface Science* 536, 130-138.
- Gao, H., Chiu, C-H, and Lee, J., 1992. Elastic contact versus indentation modeling of multi-layered materials. *International Journal of Solids and Structures* 29, 2471-2492.
- Gao, S-L, and Mäder, E., 2002. Characterisation of interphase nanoscale property variations in glass fibre reinforced polypropylene and epoxy resin composites. *Composites: Part A*, 33, 559-576.
- Henda, R., Grunze, M., and Pertsin, A. J., 1998. Static energy calculations of stress-strain behavior of self-assembled monolayers. *Tribology Letters* 5, 191-195.

- Hodges, C. S., 2002. Measuring forces with AFM: polymeric surface in liquids. *Advance in Colloid and Interface Science* 99, 13-75.
- Houston, J. E., and Michalske, T. A., 1992. The interfacial-force microscopy. *Nature* 356, 266-267.
- Hues, S. M., Draper, C. F., and Colton, R. J., 1994. Measurement of nanomechanical properties of metals using the atomic force microscopy. *The Journal Vacuum Science and Technology B* 12(3), 2211-2214.
- Israelachvili, J. N., and Adams, G. E. 1978. Measurement of forces between 2 mica surfaces in aqueous electrolyte solutions in range 0-100nm. *Journal of the Chemical Society-Faraday Transactions I* 74, 975-1001.
- Israelachvili, J. N., and Pashley, R. M., 1984. Measurement of the Hydrophobic Interaction between Two Hydrophobic Surfaces in Aqueous Electrolyte Solutions. *Journal of Colloid and Interface Science* 98, 500-514.
- Israelachvili, J. N., 1992. Adhesion force between surfaces in liquids and condensable vapors. *Surface Science Reports* 14, 109-159.
- Jeon, N. L., Krista, F., Branshaw, K., and Nuzzo, R. G., 1997. Structure and stability of patterned self-assembled films of octadecyltrichlorosilane formed by contact printing. *Langmuir* 13, 3382-3391.
- Johnson, K. L., 1985. *Contact Mechanics*. Cambridge University Press.
- Johnson, K. L., and Greenwood, T. A., 1997. An adhesion map for contact of elastic spheres. *Journal of Colloid and Interface Science* 192, 326-333.
- Johnson, K. L., Kendall, K., and Roberts, A. D., 1971. Surface energy and the contact of elastic solids. *Proceedings of the Royal Society of London, Series A*, 324, 301-313.
- Joyce, S. A., and Houston, J. E., 1991. A new force sensor incorporating force-feedback control for interfacial force microscopy. *Review of Scientific Instruments* 62(3), 710-715.
- Jun, Y., and Zhu, X.-Y., 2003. Alkoxyl monolayer as anti-stiction coatings in MEMS. *Journal of Adhesion Science and Technology* 17, 593-601.
- Keily, J. D., and Houston, J. E., 1998. Nanomechanical properties of Au (111), (001), and (110) surfaces. *Physical Review B* 57(19), 588-594.

- Kent, M. S., Yim, H., Sorenson, J., Matheson, A., and Reedy, E. D., 2002. Using self-assembled monolayers to explore the relationships between interfacial interactions and fracture in structural adhesive joints. Proceedings of 26th Annual Meeting of the Adhesion Society, Inc., pp 323-325. Myrtle Beach, SC.
- Kessel, C. R., and Granick, S., 1991. Formation and characterization of a highly ordered and well- anchored alkylsilane monolayer on mica by self-Assembly. *Langmuir* 7, 532-538.
- Khurshudov, A. G., and Kato, K., 1996. Tribological properties of carbon nitride overcoat for thin-film magnetic rigid disks. *Surface and Coating Technology* 86-87, 664-671.
- Kim, J. K., and Mai, Y-W, 1998. Engineered Interfaces in Fiber Reinforced Composites. Elsevier Sciences, p257.
- Kim, J. K., Sham, M. L., and Wu, J., 2001. Nanoscale characterization of interphase in silane treated glass fiber. *Composites: Part A* 32, 607-618.
- Kim, M. T., 1996. Influence of substrates on the elastic reaction of films for microindentation tests. *Thin Solid Films* 283, 12-16.
- King, R. B., 1987. Elastic analysis of some punch problems for layered medium. *International Journal Solids and Structures* 23, 1657-1664.
- Kluth, G. J., Sung, M. M., and Maboudian, R., 1997. Thermal behavior of alkylsiloxane self-assembled monolayers on the oxidized Si(100) surface. *Langmuir* 13, 3775-3780.
- Kojio, K., Ge, S., Takahara, A., and Kajiyama, T., 1998. Molecular aggregation state of n-octadecyltrichlorosilane monolayer prepared at an air/water interface. *Langmuir* 14, 1998.
- Kumar, A., and Whitesides, G. M., 1993. Feature of gold having micrometer to centimeter dimensions can be formed through a combination of stamping with an elastomeric stamp and an alkanethiol "ink" followed by chemical etching. *Applied Physics Letters* 63(14), 2002-2004.
- Le Grange, J. D., Markham, J. L., and Kurkjian, C . R., 1993. Effects of surface hydration on the deposition of silane monolayers on silica. *Langmuir* 9, 1749-1763.

- Li, X., and Bhusha, B., 1999. Micro/nanomechanical and tribological characterization of ultrathin amorphous carbon coatings. *Journal of Materials Research* 14, 2328-2337.
- Lourie, O., Wagner, H. D., and Levin, N., 1997. Effective width of interface in a stressed model polymer composite measured by micro-FT I.R.. *Polymer* 38, 5699-5702.
- Lucas, B. N., Hay, J. C., and Oliver, W. C., 2004. Using multidimensional contact mechanics experiments to measure Poisson's ratio. *Journal of Materials Research* 19(1), 58-65.
- Maboudian, R., 1998. Surface processes in MEMS technology. *Surface Science Reports* 30, 207-269.
- Maboudian, R., Ashurst, W. R., and Carraro C., 2000. Self-assembled monolayers as anti-stiction coatings for MEMS: characteristics and recent developments. *Sensors and Actuators* 82, 219–223.
- Maboudian, R., Ashurst W. R., and Carraro, C., 2002. Tribological challenges in micromechanical systems. *Tribology Letters* 12, 95–100.
- Madhuka, M. S., and Drzal, L.T., 1991. Fiber-matrix adhesion and its effect on composite mechanical properties. *Journal of Composite Materials* 25, 932-957.
- Magnov, S. N., and Reneker, D. H., 1997. Characterization of polymer surfaces with atomic force microscopy. *Annual Review of Materials Science* 27, 175-222.
- Major R. C. and Zhu, X.-Y., 2001. Two-step approach to the formation of organic monolayers on the silicon oxide surface. *Langmuir* 17, 5576-5580.
- Maoz, R., and Sagiv, J., 1984. On the formation and structure of self-assembling monolayers. I. A comparative ATR-wettability study of Langmuir-Lodgett and adsorbed films on flat substrates and glass microbeads. *Journal of Colloid and Interface Science* 100(2), 465-496.
- Maugis, D., 1992. Adhesion of spheres: the JKR-DMT transition using a Dugdale model. *Journal of Colloid and Interface Science* 150, 243-269.
- Maugis, D., 2000. *Contact, Adhesion and Rupture of Elastic Solids*. Springer-Verlag, Berlin.

- Mello, A. W., and Liechti, K. M., 2004. Controlling mixed-mode interfacial fracture toughness with self-assembled monolayers. submitted to Journal of Applied Mechanics. Engineering Mechanics Research Laboratory Report EMRL #03-10.
- Menčík, J., Munz, D., Quandt, E., Weppelmann, E. R., and Swain, M. V., 1997. Determination of elastic modulus of thin layers using nanoindentation. Journal of Materials Research 12(9), 2475-2484.
- Meurs, P. F. M., Schreurs, P. J. G., Peijs, T., and Meijer, H. E. H., 1996. Characterization of interphase conditions in composite materials. Composites A 27A, 781-786.
- Nakagawa, T, Ogawa, K., and Kurumizawa, T., 1994. Atomic force microscope images of monolayers from alkyltrichlorosilane on mica surfaces and studies on an anchoring mechanism of alkyltrichlorosilane molecules to the surface. Langmuir 10, 525-529.
- Needleman, A., 1987. A continuum model for void nucleation by inclusion debonding. Journal of Applied Mechanics 54, 525-531.
- Needleman, A., 1990. An analysis of tensile decohesion along an interface. Journal of Mechanics and Physics of Solids 38, 289-324.
- Noy, A., Vezenov, D. V., and Lieber, C. M., 1997. Chemical force microscopy. Annual Review of Materials Science 27, 381-421.
- Oliver, W. C., and Pharr, G. M., 1992. An improved technique for determining hardness and elastic modulus using load and displacement sensing indentation experiments. Journal of Materials Research 7(6), 1564-1583.
- Parikh, A. N., Liedberg, B., Atre, S. V., Ho, M., and Allara, D. L., 1995. Correlation of molecular organization and substrate wettability in the self-assembly of n-alkylsiloxane monolayers. Journal of Physical Chemistry 99, 9996-10008.
- Pharr, G. M., Oliver, W. C., and Brotzen, F. R., 1992. On the generality of the relationship among conical stiffness, contact area, and elastic modulus during indentation. Journal of Materials Research 7(3), 613-617.
- Plueddemann, 1982. *Silane Coupling Agents*, Plenum Press, New York.

- Plueddemann, 1991. Chapter 9 in *Fundamentals of Adhesion*, edited by Lee, L-H, Plenum Press, New York, pp279-290.
- Rao, V., and Drzal, L.T., 1991. The dependence of interfacial shear strength on matrix and interphase properties. *Polymer Composites* 12, 48-56.
- Reedy, E. D. (Jr.), Kent, M. S., and Moody, N. R., 2002. On the relationship between the molecular work of separation and interfacial fracture toughness. Proceedings of 26th Annual Meeting of the Adhesion Society, Inc., pp502-504. Myrtle Beach, SC.
- Rybczynski, J., Ebels, U., and Giersig, M., 2003. *Colloids and Surfaces A: Physicochemical and Engineering Aspects* 219, 1-6.
- Sagiv, J., 1980. Organized monolayers by adsorption. 1. Formation and structure of oleophobic mixed monolayers on solid surfaces. *Journal of the American Chemical Society* 102(1), 92-98.
- Saha, R., and Nix, W. D., 2002. Effects of the substrate on the determination of thin film mechanical properties by nanoindentation. *Acta Materialia* 50, 23-38.
- Sawa, T., Akiyama, Y., Shimamoto, A., and Tanaka, K., 1999. Nanoindentation of a 10nm thick film. *Journal of Material Research* 14, 2228-2232.
- Shirafuji, T., and Tachibana, K., 1994. Photo-excited removal of native oxide on a silicon wafer in NF₃ gas using a VUV Xe lamp. *Applied Surface Science* 79/80, 117-121.
- Siepmann, J. L., and McDonald, I. R., 1993. Monte Carlo simulation of the mechanical relaxation of a self-assembled monolayer. *Physical Review Letters* 70(4), 453-456.
- Silberzan, P., Léger, L., Ausserré, D., and Benattar, J. J., 1991. Silanation of silica surfaces. A new method of constructing pure or mixed monolayers. *Langmuir* 7, 1647-1651.
- Simmons, G., and Wang, H., 1971. *Single Crystal Elastic Constants and Calculated Aggregate Properties: A HANDBOOK*, 2nd Ed., The M.I.T. Press, Cambridge.

- Skala, R. D., Low, I. M., and Li, D. Y., 1994. Origins, effects, and characterization of residual strains in composite materials. *Journal of the Australasian Ceramic Society* 30, 97-116.
- Smith, W., and Forester, T. R., 1996. DL_POLY_2.0: A general-purpose parallel molecular dynamics simulation package. *Journal of Molecular Graphics* 14(3), 136-141.
- Smith, W., and Forester, T. R., 2001. *The DL_PLOY_2 User Manual*. CCLRC, Daresbury Laboratory, Daresbury, England.
- Sneddon, I. N., 1965. The relation between load and penetration in the axisymmetric Boussinesq problem for a punch of arbitrary profile. *International Journal of Engineering Science* 3, 47-57.
- Srinivasan, U., Houston, M. R., Howe, R. T., and Maboudian, R., 1998. Alkyltrichlorosilane-based self-assembled monolayer films for stiction reduction in silicon micromachines. *Journal of Microelectromechanical Systems* 7(2), 252-260.
- Stevens, M. J., 1999. Thoughts on the structure of alkylsilane monolayers. *Langmuir* 15, 2773-2778.
- Swadener, J. G., George, E. P., and Pharr, G., M., 2002. The correlation of the indentation size effect measured with indenters of various shapes. *Journal of Mechanics and Physics of Solids* 50(4), 681-694.
- Swadener, J. G., Liechti, K. M., and de Lozanne, A. L., 1999. The intrinsic toughness and adhesion mechanism of a glass/epoxy interface. *Journal of Mechanics and Physics of Solids* 47, 223-258.
- Thomas, R. C., Houston, J. E., Crooks, R. M., Kim, T., and Michalske, T. A., 1995. Probing adhesion forces at the molecular scale. *Journal of the American Chemical Society* 117(13), 3830-3834.
- Thomas, R. C., Houston, J. E., Michalske, T. A., and Crooks, R. M., 1993. The mechanical response of gold substrates passivated by self-assembling monolayer films. *Science* 295(5130), 1883-1885.
- Thomas, R. C., Tangyonyong, P., Houston, J. E., Michalske, T. A., Crooks, R. M., 1994. Chemically-sensitive force microscopy: contact potential measurement of self-assembling monolayer films. *Journal Physical Chemistry* 98(17), 4493-4494.

- Tripp, C. P., and Hair, M. L., 1992. An infrared study of the reaction of octadecyltrichlorosilane with silica. *Langmuir* 8, 1120-1126.
- Tupper, K. J., Colton, R. J., and Brenner, D. W. 1994. Simulations of self-assembled monolayers under compression: effect of surface asperities. *Langmuir* 10, 2041-2043.
- Tupper, K. J., and Brenner, D. W., 1994. Compression-induced structural transition in a self-assembled monolayer. *Langmuir* 10, 2335-2338.
- Ulman, A., 1991. *An Introduction to Ultrathin Organic Films from Langmuir-Blodgett to Self-Assembly*. Academic Press, Inc.
- Ulman, A., 1996. Formation and structure of self-assembled monolayers. *Chemical Reviews* 96, 1533-1554.
- Vajapeyajula, K., 2002. An investigation into the mechanical properties of thin organic monolayers. Thesis for M.S., The University of Texas at Austin. Engineering Mechanics Research Laboratory Report EMRL #02-09.
- van Krevelen, D. W., 1990. *Properties of Polymers: Their Correlation with Chemical Structure, Their Numerical Estimation and Prediction from Additive Group Contributions*. 3rd ed., Elsevier Science Publisher.
- van Landingham, M. R., Dagastine, R. R., Eduljee, R. F., McCullough, R. L., and Gillespie, J. W., 1999. Characterization of nanoscale property variations in polymer composite systems: 1. experimental results. *Composites: Part A*, 30, 75-83.
- Wang, M., Liechti, K. M., Srinivasan, V., White, J. M., Rossky, P. J., and Stone, M. T., 2004. A hybrid continuum-molecular analysis of IFM experiments on a self-assembled monolayer. Submitted to *Journal of Applied Mechanics*.
- Wang, M., Liechti, K. M., White, J. M., and Winter, R. M., 2004. Nanoindentation of polymeric thin films with an interfacial force microscope. accepted, *Journal of the Mechanics and physics of Solids*.
- Wang, Q., Sun, Y.-M., Zhao, W., Campagna, J., and White J. M., 2002. In situ laser annealing system for real-time surface kinetic analysis. *Review of Scientific Instruments* 73(11), 3916-3919.

- Warren, O. L., Graham, J. F., and Notton, P. R., 1997. Tapping Mode Imaging with an Interfacial Force Microscope. *Review of Scientific Instruments* 68(11), 4124-4131.
- Wasserman, S. R., Tao, Y-T, and Whitesides, G. M., 1989. Structure and reactivity of alkylsiloxane monolayers formed by reaction of alkyltrichlorosilanes on silicon substrates. *Langmuir* 5, 1074-1087.
- Williams, J. G., Donnellan, M. E., James, M. R., and Morris W. L., 1990. Properties of the interphase in organic matrix composites. *Material Science and Engineering A* 126, 305-312.
- Winter, R. M., and Houston, J. E., 1998(a). Interphase mechanical properties in an epoxy-glass fiber composites as measured by interfacial microscopy. in *Proceedings of the SEM Spring Conference on Experimental and Applied Mechanics*, Houston, TX.
- Winter, R. M., and Houston, J. E., 1998(b). Nanomechanical properties of the interphase in polymer composites as measured by interfacial force microscopy. presented at the *Materials Research Society Spring Meeting*, San Francisco, CA.
- Winter, R. M., 2002. Private communication.
- Xia, Y., Mrksich, M., Kim, E., and Whitesides, G. M., 1995. Microcontact printing of octadecylsiloxane on the surface of silicon dioxide and its application in microfabrication. *Journal of the American Chemical Society* 117, 9576-9577.
- Xia, Y., and Whitesides, G. M., 1998. Soft Lithography. *Annual Reviews of Material Science* 28, 153-84.
- Yoffe, E. H., 1998. The elastic compliance of a surface film on substrate. *Philosophical Magazine Letters* 77, 69-77.
- Yu, H. Y., Sanday, S. C., and Rath, R. R., 1990. The effect of substrate on the elastic properties of films determined by the indentation test-axisymmetric Boussinesq problem. *Journal of Mechanics and Physics of Solids* 38, 745-764.
- Zhuk, A. V., Evans, A. G., Hutchinson, J. W., and Whitesides, G. M., 1998. The adhesion energy between polymer and self-assembled monolayers. *Journal of Materials Research* 13, 3555-3564.

Zhuravlev, L. T., 1987. Concentration of hydroxyl groups on the surface of amorphous silicas. *Langmuir* 3, 316-318.

Vita

Mingji Wang, the son of Xihua Wang and Yunhua Shi, was born in Zhenjiang, Jiangsu Province of P. R. China, on January 8, 1967. After completing high school at No. 3 High School at Zhenjiang in 1985, Mingji Wang entered Nanjing Aeronautics Institute at Nanjing (in 1993 it was renamed as Nanjing University of Aeronautics and Astronautics), China. From there, he received the degree of Bachelor in Helicopter Design in 1989 and the degree of Master in Solid Mechanics/Structural Dynamics in 1992, respectively. He then worked as a teacher at The East China Shipbuilding Institute (it has been renamed as Jiangsu University of Science and Technology) for six years. During that period, he had one year of industrial experience and he married Guirong Gu in 1994. Mingji Wang entered the Graduate School of The University of Texas at Austin in 1999.

Permanent address: He-jia-men 212, West Zhongshan Rd.
Zhenjiang, Jiangsu 212002
P. R. China

This dissertation was typed by the author.